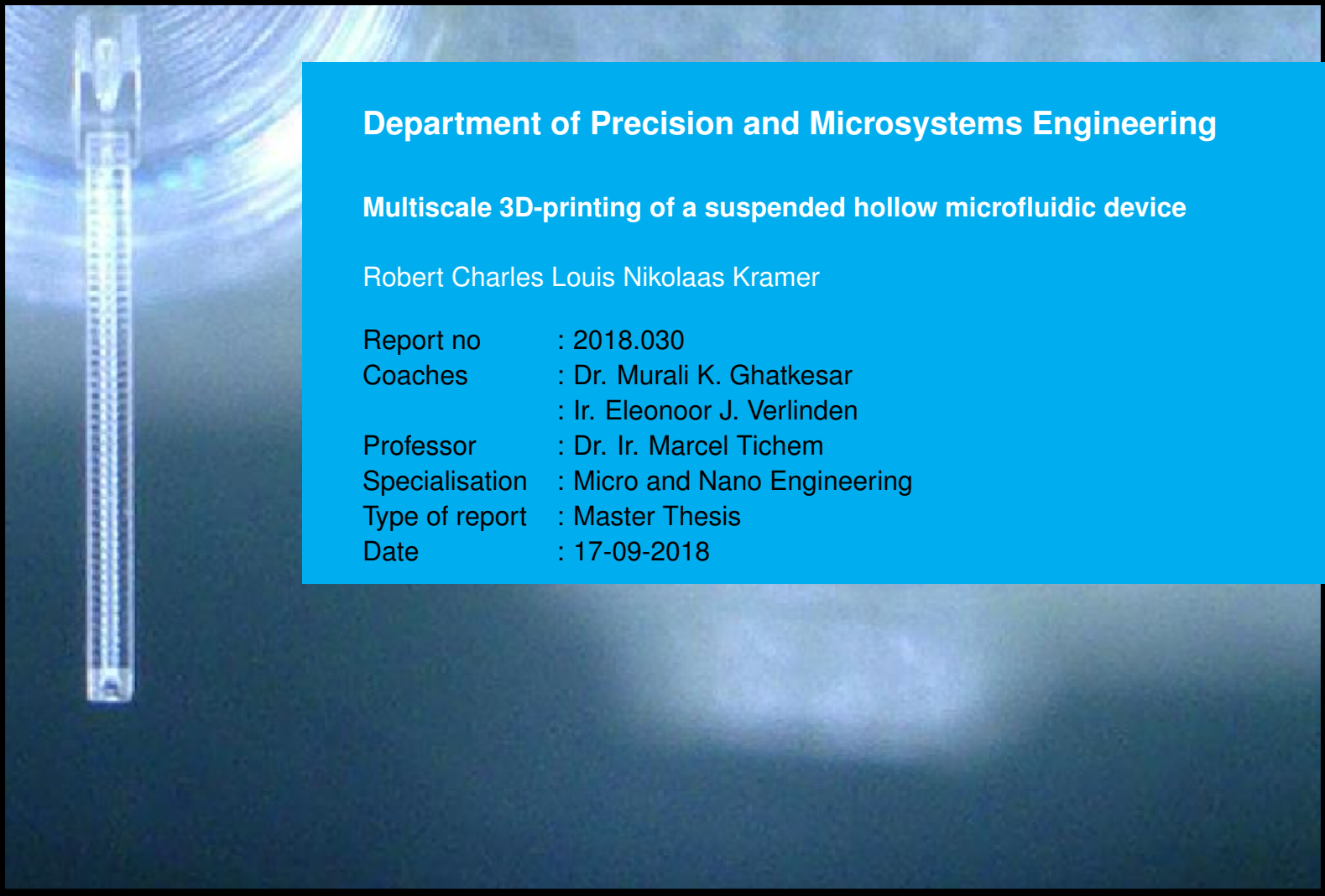
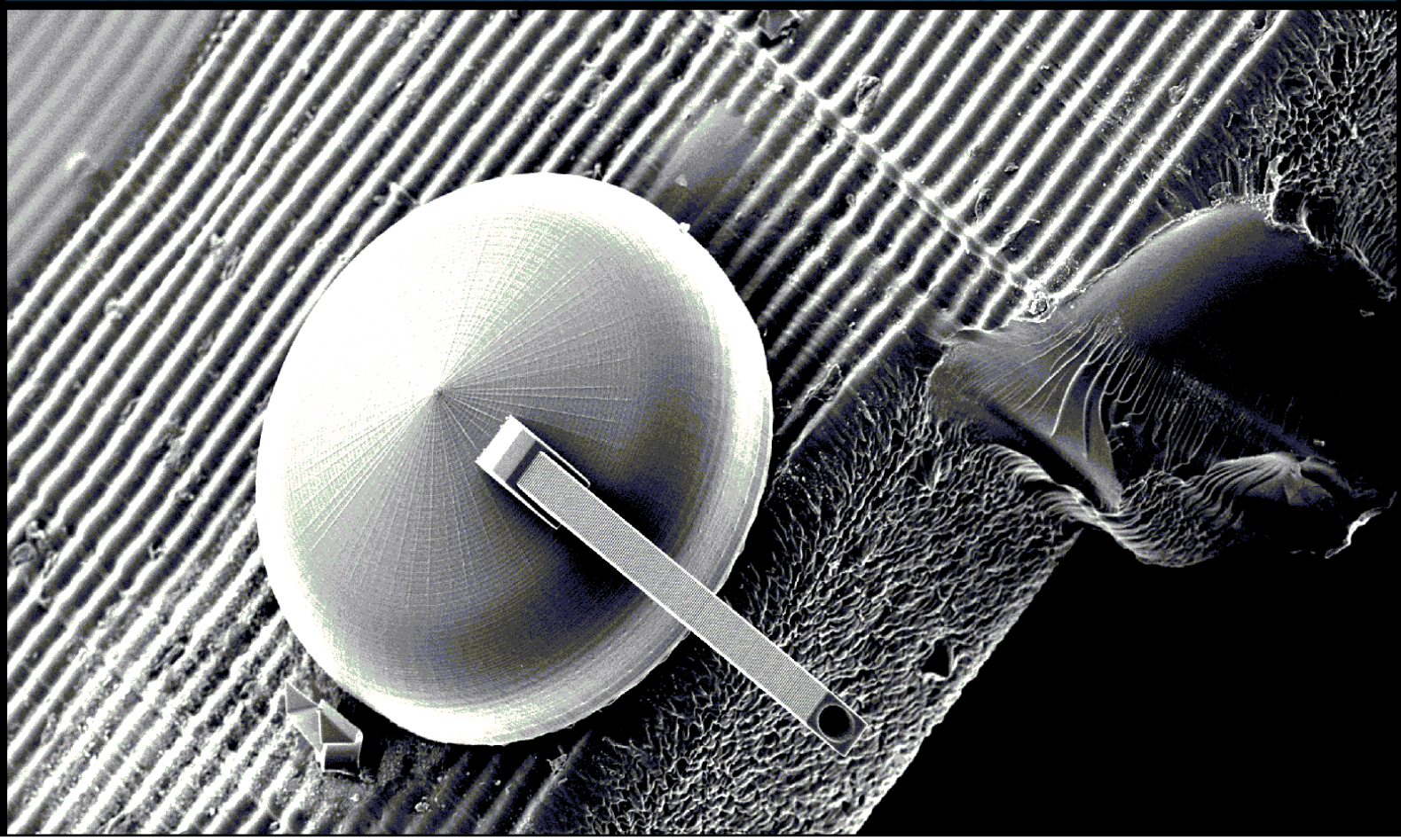


Department of Precision and Microsystems Engineering

Multiscale 3D-printing of a suspended hollow microfluidic device

Robert Charles Louis Nikolaas Kramer

Report no	: 2018.030
Coaches	: Dr. Murali K. Ghatkesar
	: Ir. Eleonoor J. Verlinden
Professor	: Dr. Ir. Marcel Tichem
Specialisation	: Micro and Nano Engineering
Type of report	: Master Thesis
Date	: 17-09-2018



TU Delft Delft University of Technology

Challenge the future

Preface

This past year I've experienced the taste of individual academic research. Prior to this I was only a consumer of knowledge, and through this project I had the pleasure of attempting the creation of it.
Working on this master's graduation project allowed me a glimpse in the scientific world, and made it possible for me to interact with some of the most creative and intelligent knowledge-creators I've ever met.
These interactions have not been possible without the nurturing scientific environment of the Technical University Delft, and the welcoming attitude of the Precision and Microsystems Engineering department and Micro and Nano Engineering group.

I would like to offer my gratitude to my graduation committee: Dr. Ir. Marcel Tichem as chair, Dr. Massimo Mastrangeli as external member, Dr. Murali K. Ghatkesar as supervisor, and Ir. Eleonoor J. Verlinden as daily supervisor.

My gratitude extends towards everyone with whom I've had the pleasure to share the office space with this past year, and the many enjoyable discussions over lunch and coffee breaks.
Special thanks to the other PME-staff members that provided training and guidance, such as Luigi Sasso, Paola Fanzio, Pierpaolo Belardinelli, Cristina Varone, and all others from which I've had the privilege of learning from, in my time at this university.
I would like to specifically thank my supervisors Murali K. Ghatkesar and Eleonoor J. Verlinden for their untiring guidance and unceasing enthousiasm during this project.
Part of this thesis wouldn't have been possible without Hongzhi Zhang from the Microlab of the Civil Engineering department with his help on the nano indentation experiments.
Thanks as well to the technical staff: Rob Luttjeboer, Spiridon van Veldhoven, Patrick van Holst, and Harry Jansen for their technical support.

Throughout my studies I've enjoyed the invaluable support from my family members, to whom I'll be indebted forever.

Robert Charles Louis Nikolaas Kramer
September 3, 2018

Contents

1 Introduction - literature review **1**
1.1 Introduction . . . 1
1.1.1 Force spectroscopy . . . 1
1.1.2 Manipulating matter . . . 2
1.1.3 Microfluidic probes . . . 2
1.1.4 Polymeric hollow AFM cantilevers . . . 2
1.2 Theory . . . 3
1.2.1 Atomic force spectroscopy / microscopy . . . 3
1.2.2 Mechanics . . . 3
1.2.3 Fluidics . . . 4
1.2.4 Fabrication . . . 6
1.3 State of the art . . . 7
1.3.1 Applications . . . 7
1.3.2 Fabrication methods . . . 10
1.3.3 Characterization methods . . . 13
1.4 Conclusion . . . 13
1.4.1 Research questions . . . 14

2 Paper **17**

3 Outlook **33**
3.1 Thesis conclusion . . . 33
3.2 Recommendations . . . 34
3.3 Future work . . . 34

A Fabrication **35**
A.1 Microfluidic interface . . . 35
A.2 Two-photon polymerization testing . . . 39
A.3 Connection of the SL-printed part with a 2PP-printed yurt . . . 42
A.4 Cantilevers . . . 49

B Characterization details **55**
B.1 Mechanical characterization . . . 55
B.2 Attachment experiment . . . 58
B.3 Code . . . 61

Bibliography **67**

1

Introduction - literature review

1.1. Introduction

1.1.1. Force spectroscopy

Imaging and manipulation of particles down to a single atom has become a reality thanks to several cornerstone inventions. The first images of a gold surface at atomic resolution were made by the scanning tunneling microscope (STM) in 1982 [1]. Although a wide range of materials can be mapped, it is limited to only conductive surfaces, as conductivity is a requirement for electron tunneling.
The need for topographical characterization of non-conductive surfaces led to the development of the atomic force microscope (AFM) [2], and the basic working principle is shown in figure 1.1. An AFM consists of a micrometer-sized cantilever with a sharp tip that ends in a radius of a few nanometers. When it is moved towards the surface, the tip interacts with the attractive van der Waals-, and repulsive electrostatic forces of the surface, among others. These forces deflect the cantilever, and this deflection can be transduced into an electrical signal by reflecting a laser beam from the top of the cantilever and monitoring its movement on a photodiode array [3].
The strength of the AFM lies in its ability to measure atomic interaction forces, not just in vacuum, but also

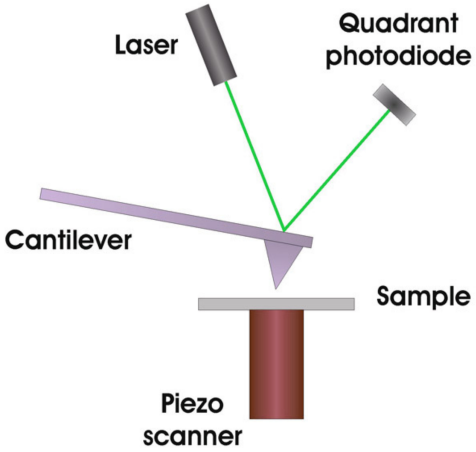


Figure 1.1: Schematic of the atomic force microscope principle with a piezo controlled stage. Image reproduced from [4].

in ambient and liquid conditions. In these conditions a dynamical imaging aspect is added, as the surfaces of solids constantly change due to adsorption and desorption of atoms and molecules. AFMs have been used in liquids [5], and have been used to monitor live cells, which have to be kept in liquid [6]. Chemical structures [7] and droplets of aqueous solution in ambient conditions [8] have also been imaged with an AFM.

1.1.2. Manipulating matter

The STM was used to position single atoms for the first time in 1990 by D. M. Eigler and E. K. Schweizer [9]. It wasn't until 2005 that the same feat was demonstrated with an AFM, due to an inability to achieve the needed gentle force control [10]. Although scientifically interesting, the process of manipulating single atoms is inherently slow. For manipulating larger volumes, microfluidic probes are better equipped for this purpose.

In 1999, 'dip-pen nanolithography' was developed [11]. This method consists of dipping an AFM-tip into a liquid and moving it close enough to a substrate so that the liquid makes contact. Upon removing the tip, some of the liquid remains onto the substrate by capillary action. This effect was used to selectively place a line of liquid with 30 nm linewidth resolution [11], and in 2007 with an even smaller resolution of 6 nm [12]. However, several drawbacks of the technique are that it is a non-continuous deposition process, since only a small amount of liquid can be held at the tip surface, and that the tip has to be loaded again after a few depositions.

1.1.3. Microfluidic probes

A hollow structure with an aperture at the end is required for continuous fluid deposition, in contrast with the non-continuous 'dip-pen' method. One approach for continuous deposition is to use glass micropipettes. these have been fabricated with tip radii of less than 50 nm by locally heating a thin-walled glass capillary and exerting a pulling force on both ends [13]. Similar glass micro-pipettes were used for near field microscopy, force sensing [14], and liquid dispensing [15].
In 2003, a nanoscale dispensing tool (NADIS) was used to dispense liquid droplets of femtoliter (10^{-15} L) volumes and below [16]. In this device an internal reservoir and aperture are present at the tip, different from the 'dip-pen' method, where the tip is solid. A droplet on top of the cantilever fills the tip and stops at the aperture due to capillarity, and, comparable to the 'dip-pen' method, the tip is brought into contact with the surface and liquid will be dispensed.
The deposited droplet volume depends mainly on the size of the liquid meniscus between tip and sample. In a subsequent paper the deposited volume had a maximum value of 40 aL (10^{-18}) using glycerol droplets with a tip aperture for the device of 200 nm [17]. In an alternative design the tip shape was altered from a simple circular aperture to a donut-shaped one with a solid core, and this design led to more control of the liquid-air meniscus position. This design reduced the deposition spacing further to an average of 100 nm, and a smallest size of 40 nm. This device was named the 'nanofountain pen' due to the similarity with a fountain pen tip [18].

Other probes emerged with an increased integration of microfluidics [19] [20], which included an internal channel and a fluid reservoir external to the cantilever. A similar design was implemented for cellular function analysis [21]. Meister et al. showed with their "FluidFM" the combination of an AFM with a fluidic system by connecting a hollow cantilever with an external pressure source through the use of an interfacing probe holder [22]. Liquid dispensing was mainly reported and pipetting was completed when aspiration was added to the probe functionality [23] [24]. Further control over flow rate, external pressure, temperature, and humidity has been added to an AFM set-up and combined with a hollow AFM cantilever [25]. The two functionalities of force sensing and fluidic manipulation are both needed in the same device to be able to call it a hollow AFM cantilever. The main fabrication material for the cantilevers described here is either silicon, silicon oxide, and silicon nitride. More of these fluid handling probes has been reviewed elsewhere [26].

1.1.4. Polymeric hollow AFM cantilevers

The photopolymers that are used in photolithography can also be used as a fabrication material, and this was demonstrated by Gaitas and Hower [27], when they fabricated hollow fluidic cantilevers out of the photopolymer SU-8.
Martinez et al. designed and fabricated hollow polymer cantilevers and used them to controllably deposit single-cells, thereby showing fluidic functionality [28]. Martinez et al. also measured sub-nano newton forces in cell adhesion studies, thereby demonstrating the possibility of doing force measurements [29].

All the hollow AFM cantilevers described so far were mainly fabricated with standard clean room micro/nano fabrication techniques. However, these techniques are inherently inflexible in design, because most patterning steps require a mask that has to be replaced for every set of alterations in the probe design.

1.2. Theory

1.2.1. Atomic force spectroscopy / microscopy

The interaction of a cantilever tip with surfaces is the basis for atomic force spectroscopy. When the tip is brought close enough, its atoms interact with the closest atoms, that of the surface. In vacuum, this interaction is governed by short-range chemical bonding forces, and long-range van der Waals, electrostatic, and magnetic dipole forces [30].
Additional forces play a role, when the measurements are not done in vacuum but in ambient conditions. This can lead to a thin film of water on both the cantilever tip and surface, and capillary forces can create a capillary bridge of water in close proximity. These force interactions can be used to perform imaging of surfaces. The images are formed by monitoring the deflection of the cantilever when moving across a surface by reflecting a laser beam from the cantilever surface to a photodetector. If a 'step' in the surface topography is encountered, then the deflection amplitude changes, resulting in a change in the signal captured by the photodetector. Combined with the known tip position a three dimensional image can be reconstructed.

AFMs are operated in a static or dynamic mode, of which the latter gives an improvement in resolution over the static mode [31]. In the static mode the tip-surface interaction force translates directly in a cantilever deflection, while in the dynamic mode the cantilever is vibrated at the resonance frequency of the beam. The dynamic mode can be subdivided in amplitude modulation (AM), and frequency modulation (FM), which both rely on feedback for control. In the AM-mode the frequency is held constant, and the cantilever is excited slightly off resonance. Force interactions lead to a change in resonance frequency, which result in a change in amplitude. In FM mode the amplitude is kept constant, and when force interactions occur, the resonance frequency changes [32].

1.2.2. Mechanics

Analysis of the dynamical behaviour of a hollow cantilever without considering internal flow leads to important relations between the resonance frequency, the beam stiffness, Young's modulus, and quality factor. The stiffness of the beam is calculated with equation 1.1,

$$k = 4\pi^2 m^* f_0^2 \tag{1.1}$$

where m^* is the effective mass for a single-clamped beam, in this case $\frac{33}{140} m_c$, with m_c being the cantilever rest mass, and f_0 the fundamental frequency. The effective mass is used because the total kinetic energy of a resonating cantilever is distributed over it, making it seem as if it has a higher mass, compared to cantilevers vibrating at low frequencies or at rest.

The Young's modulus can be derived from the deflection and stiffness as follows: beam deflection according to the Euler-Bernoulli beam theory is $y = \frac{Fl^3}{3EI}$, where F is the force, l the length, E the Young's modulus, and I the bending moment of inertia. The moment of inertia of a square with a circular hole is given in equation 1.2.

$$I = \frac{wt^3}{12} - \frac{\pi d^4}{64} \tag{1.2}$$

w is the cantilever width, t its thickness, and d the internal channel diameter.
It is assumed that deflections are small and occur in the elastic regime. Hooke's law states that $F = ky$, where k is the stiffness, then, substituting for k and rewriting the equation, an equation for the Young's modulus can be given 1.3.

$$E = \frac{4\pi^2 m^* f_0^2 l^3}{3I} \tag{1.3}$$

The quality factor is a measure of energy dissipation and is defined as the total stored energy divided by the dissipated energy per cycle. In mathematical terms, $Q = \frac{E_{\text{total}}}{E_{\text{diss,cycle}}}$. The height and width of the resonance peaks are indicative for the energy dissipation, and the Q-factor follows directly from them with equation 1.4,

$$Q = \frac{f_0}{BW} \tag{1.4}$$

where *BW* is the bandwidth from where the amplitude reduces by 3 dB.

The dynamics of a flow-containing pipe is governed by the linearised equation of motion described in equation 1.5, and its parameters are listed in table 1.1.

$$EI\left[1+\left(\alpha+\frac{\mu}{\Omega}\right)\frac{\partial}{\partial t}\right]\frac{\partial^4 w}{\partial x^4}+Mv^2\frac{\partial^2 w}{\partial x^2}+2Mv\frac{\partial^2 w}{\partial x\partial t}+c\frac{\partial w}{\partial t}+(M+m)\frac{\partial^2 w}{\partial t^2}=0 \tag{1.5}$$

This equation remains valid if the smallest structural dimension exceeds 1 µm, with $0.1 < D_i/D_O < 0.5$ and $L/D_O > 10$ [33]. D_i and D_O are the inner- and outer diameters of the tube respectively. The channel and wall dimensions of hollow cantilevers are in these orders of magnitude. From equation 1.5 a non-dimensional critical flow velocity, v_c, can be derived and the dimensional form is described in equation 1.6. ρ_f is the fluid density, λ_1 the ratio D_i/D_O, and λ_2 the ratio L/D_O. Flow speeds larger than this critical velocity will result in unstable cantilever behaviour.
Non-linear models have been proposed [34] [35], but those go beyond the scope of this literature review.

$$v_c = 5\sqrt{\frac{E}{\rho_f}\frac{\sqrt{1-\lambda_1^4}}{4\lambda_1\lambda_2}} \tag{1.6}$$

Table 1.1: Parameters of equation 1.5.

x	axial coordinate
t	time
$w(x,t)$	lateral deflection
E	Young's modulus
I	Second moment of area
α	viscoelastic damping coefficient
μ	hysteric damping coefficient
Ω	circular frequency
c	viscous damping coefficient (external fluid)
M	beam mass per unit length
m	fluid mass per unit length
v	fluid flow velocity

1.2.3. Fluidics

A further analysis of the flow speed inside a hollow cantilever reveals information about the fluidic functioning of the device. The flow can be either laminar or turbulent, depending on several factors including the channel dimensions, type of fluid, flow speed, and surface conditions. Macroscale flow is largely governed by volume forces such as inertia and gravity, but microscale flow is more affected by surface forces, for example capillarity.

Due to the micrometer-sized channels in the cantilevers, the flow is considered to be laminar, as viscous forces in the liquid dominate over inertial forces. Fluid flow is described mathematically by the Navier-Stokes equations, and equation 1.7 shows them for an incompressible fluid. The assumption of incompressibility holds if the fluid density remains constant, and if the fluidic speed is several orders of magnitude smaller than the speed of sound in the same material.

$$\rho\left(\frac{\partial \mathbf{v}}{\partial t}+(\mathbf{v}\cdot\nabla)\,\mathbf{v}\right)=-\nabla p+\mu\nabla^2\mathbf{v}+\rho\mathbf{g} \tag{1.7}$$

Where ρ is the fluid density, $\mathbf{v}$ the fluidic speed, p the pressure, μ the dynamic viscosity, and $\mathbf{g}$ the gravitational vector.
Solutions to this equation depend on the boundary conditions associated with the channel shape, and solving equation 1.7 for a cylindrical pipe leads to equation 1.8, otherwise known as Hagen-Poiseuille flow.

$$Q = \frac{\pi r^4}{8\mu L}\Delta p \tag{1.8}$$

Where Q is the flowrate, r the inner diameter, and L the length of a straight tube.
Flow in a rectangular channel results in equation 1.9, where b is the height of the channel, and a is the width.

$$Q = \frac{wh^3}{12\mu L}\left[1 - \left(\frac{192h}{\pi^5 w}\right)\sum_{i=1,3,5,\ldots}^{\infty}\frac{\tanh(\frac{i\pi w}{2h})}{i^5}\right]\Delta p \tag{1.9}$$

In electric circuits resistance is defined by Ohm's law as the voltage divided by the current. An equivalent approach can be taken for microfluidic circuits [36]. If the pressure is taken as an analogy to the voltage and the flow rate Q as current, then the hydraulic resistance for a circular channel, as seen in equation 1.10, follows from equation 1.8.

$$R_{\text{hyd,circ}} = \frac{8\mu L}{\pi r^4} \tag{1.10}$$

The analogy with the electrical circuit can be taken further to include capacitive elements. The physical reasoning behind this analogy is that the volume of the channel slightly increases due to elastic deformation of the material when a pressure is applied over it, leading to a temporal storage of fluid. This material dilatability is approximately the inverse of the Young's modulus, and the hydraulic capacitance can be approximated by equation 1.11, where V denotes the undeformed volume (V) in the channel and E the Young's modulus of the material [37].

$$C_{hyd} \approx \frac{V}{E} \tag{1.11}$$

These equations are valid for fully developed flow, however, during initial wetting of microchannels capillary effects have to be taken into account. Depending on surface tension properties of the channel walls, it can either effectively raise or lower the hydraulic resistance. Capillarity in a channel is described by the Young-Laplace equation 1.12.

$$\Delta P_c = \gamma\left(\frac{1}{R_1} + \frac{1}{R_2}\right) \tag{1.12}$$

ΔP_c is the pressure difference, γ the surface tension of the channel walls, and R_1 and R_2 the principal radii of curvature of the meniscus. For a circular shaped channel these radii are identical, and it can be described as a function of the channel radius and contact angle of the meniscus with the wall. Equation 1.13 describes the initial filling of a microfluidic channel.

$$Q = \frac{\pi r^4}{8\mu L}\left(\Delta P + \frac{2\gamma\cos\theta}{r}\right) \tag{1.13}$$

1.2.4. Fabrication

Micro/nanofabrication

A clean room micro/nanofabrication technique such as photolithography is capable of producing 22 nm feature sizes, with the next generation of patterning techniques capable of sub-10 nm line spacing [38]. Patterns are created by adding a layer of light-sensitive polymer and patterns are transferred to the polymer using a mask. Then irradiation takes place, which locally polymerizes the polymer. Polymerization is the absorption of a photon by a photoinitiating chemical, which releases a radical that enables cross-linking of oligomers to form a polymer. After removal of the non-irradiated polymer the layer below can be etched, or another layer of material can be deposited. Several etching techniques exist, such as isotropic- and anisotropic wet etching with chemicals, and plasma etching. Several material deposition/growth techniques exist, among those are oxidation, chemical-, and physical vapor deposition [39]. The layer-by-layer approach makes this a planar process, and so it becomes difficult to fabricate three-dimensional structures.

Stereolithography

The layer-by-layer approach is also commonly used in 3D-printing technology, and is particularly useful for microfluidics. The difference with the micro/nanofabrication methods described in paragraph 2.4.1 is the use of only one type of material to fabricate a structure, namely photopolymers. Researchers are able to adopt a "fail fast and often" approach due to the fast printing speed, and the manipulation of surfaces and fluids in three dimensions enlarges the design space [40].
An example of such a layer-by-layer technique is stereolithography. The structure is created in a bath of photoresist by using a laser to scan over the bath surface, thereby polymerizing the photoresist. When the layer is finished, the platform is raised, and the next layer can be fabricated. The laser can be positioned above the bath, as in figure 1.2, or at the bottom, which requires a transparent bath. Commercial systems can offer smallest structure details of 20 µm [41], with research set-ups attaining 0.43 µm [42]. Figure 1.3 shows the process from computer aided design (CAD) to print.

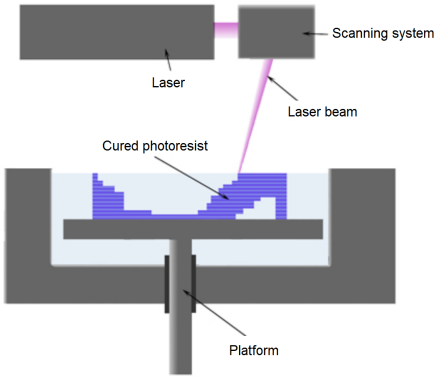


Figure 1.2: Stereolithography principle.

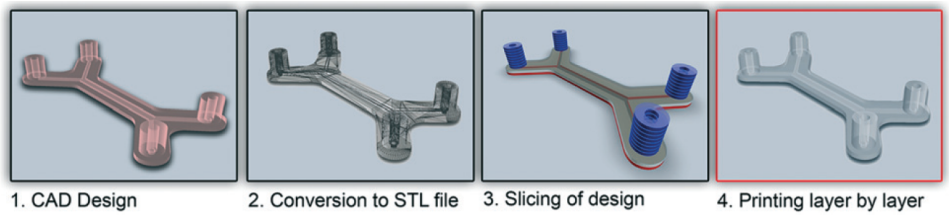


Figure 1.3: The additive manufacturing process. The CAD file is converted into a standard triangulation language (STL) file. The STL file is digitally sliced into individual layers that are sequentially realised to build an object in a layer-by-layer manner. Image reprinted from [40].

Two photon polymerization

The previous two techniques have a fundamental limit to their resolution; they are limited by diffraction, which is the bending of light around corners of an object or aperture. This determines the smallest focal spot, and thus the volume which is illuminated. However, unwanted polymerization also occurs in the light cone around the laser focus, and therefore the focal point is positioned near the bath surface in conventional stereolithography. This ensures that the next layer of photoresist isn't partially polymerized by the previous illumination step.
A way around this limitation is the use of a technique called two-photon polymerization (2PP). As the name suggests, instead of the single photon needed to initiate polymerization, two photons are needed to be absorbed. Figure 1.4 compares one photon absorption (1PP) with 2PP.

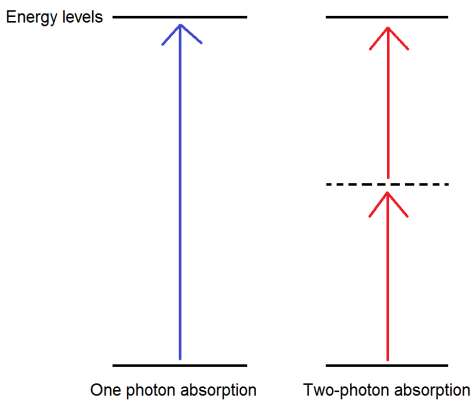


Figure 1.4: Two-photon absorption principle.
The dashed line indicates a virtual energy level.

When the photo-initiator molecule absorbs a photon, it raises the energy level of one of its atoms, and that breaks a carbon-carbon bond. In 2PP, photons of lower frequency are used that don't have sufficient energy to start this reaction separately, therefore it occurs only if two are absorbed by the same atom within roughly 1 femto second [43]. The chance of two photons absorbing reduces non-linearly away from the laser focus. This non-linearity reduces the polymerised volume (voxel) further to sub-micrometer accuracy [44]. Because polymerization occurs mainly in the small elliptical volume around the focus, no bath surface is needed. This polymerization reduction is shown in figure 1.5.

1.3. State of the art

In this chapter the an overview of hollow cantilever research is given. Relevant parameters following from the applications are ordered in tabels 1.2 and 1.3. Then, fabrication methods are given, and the chapter is closed with characterization methods to investigate these parameters.

1.3.1. Applications

Pipetting

One use of hollow cantilevers is the controlled pipetting of volumes down to femtolitres (10^{-15} L), which is of importance for extracting substances from, or injecting into cells, without disturbing cellular functions significantly [46]. A hollow cantilever has been used to pattern lines of DNA functionalized gold nanoparticles [47], as well as nanodiamond particles [48]. In the same paper functionalized nanodiamond particles were also injected into cells.
Pipetting can also be used for the local deposition of chemicals to enable the synthesis of nanoparticles, which has been demonstrated for gold particles with sizes down to 4 nm [49]. The parameters of importance for pipetting are flow rate control, and deposition resolution, which are listed in table 1.2 for various cantilevers.

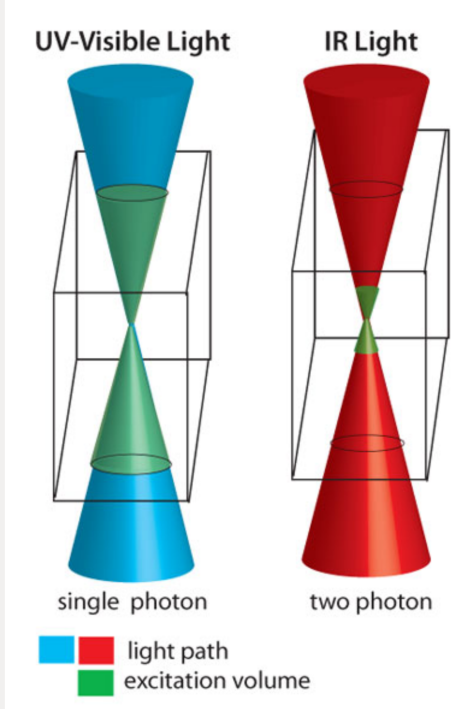


Figure 1.5: Comparison between 1PP and 2PP of the polymerized region around the laser beam focus. Reproduced from [45].

Force spectroscopy

Force spectroscopy is another application, and it has been used to investigate single molecules [50] [51], for example the elastic behaviour of single DNA molecules [52], or reaction-induced changes in the covalent bond structure of molecules [53]. Live cells has also been probed, and their stiffness can reveal information about the state of its cytoskeleton [54]. Cantilevers can be fabricated with low stiffness values that are suitable for force spectroscopy and imaging of biological materials [55].

Imaging

AFM imaging is performed on surfaces, however, ultrasound elastic waves through the sample could be picked up by an AFM and provide information on the inside of structures [56]. Of the discused applications, most regular AFM cantilevers are fabricated from silicon or silicon nitride. However, polymers have also been used as materials, and their imaging capabilities have been showcased for novolac [57], PMMA [58], and SU-8 cantilevers [59]. The use of polymers also opens up another way of detecting the cantilever deflection by making use of the transparency of SU-8 [60]. A beam of light is shone into the un-clamped front of the cantilever, and its intensity measured at the clamped side. The light intensity then changes in response to a cantilever deflection, making the cantilever into a waveguide.

One limiting factor for the imaging resolution is the tip radius, and silicon tips with radii below 10 nm are commercially available. Polymer AFM tips of arbitrary shape have been 3D-printed on silicon cantilevers with a minimum tip radius of 25 nm [61].

Imaging performed with hollow AFM cantilevers is not extensively reported, and only a few publications have been reported [19] [62]. Important parameters for imaging are the beam stiffness, that influences the available frequency bandwidth, as well as the tip radius and tip length, which have a direct influence on the resolution. A big tip radius won't be able to map structures that are smaller than it accurately, and tip length limit mapping of high aspect ratio features on surfaces.

Detection and mass sensing

Nanomechanical resonators are micrometer-sized beams capable of detecting single molecules and surface related physical quantities [63]. They function in two modes, the static mode and dynamic mode. In the static

mode the beam deflects whenever a particle attaches to the surface, due to the surface stress this attaching induces. In the dynamic mode the mass of the attached particle influences dynamical properties of the beam, such as a shift in the eigenfrequencies. The sensitivity thus depends on how accurate the frequency measurements can be performed, with the theoretical maximum limit of the thermomechanical noise.

The particles are adsorbed on the surface of a nanomechanical resonator and the dynamical properties of the resonator are influenced by high damping and viscous drag of the surrounding medium. Integration of a microchannel within such a beam circumvented these problems, and enabled detection of biomolecules adsorbed to the channel wall as low as femtograms [64]. With such a resonator a detection limit of a single bacteria (*L. monocytogenes*) per µL has been demonstrated [65]. Silicon nitride was used to fabricate the first suspended microchannel resonators (SMR), but more recently polymeric SMRs have been fabricated. They have been used to detect 10^5-10^7 oocysts per mL of the waterborne pathogen *Cryptosporidium* [66] and bovine growth hormones with a detection limit of 2 ng$\,$mL^{-1} [67].

A natural follow up from particle detection is the determination of the mass of small particles with these devices [64], approaching lower limits of attograms in vaccuum [68]. The viscosity of the medium in which the cantilever is used has an adverse effect on the quality factor and so on the sensitivity [69]. However, scaling the dimensions down has a positive effect on the viscous damping inside the cantilever [70]. Relevant parameters are the mass sensitivity and Q-factor, listed in table 1.3. Other quantities than mass are of interest, because some cells retain their mass but can change their density when there's something wrong with their internal functioning. An expansion on the mass measurement method enables the measurement of mass, volume, and density [71]. Setting several resonators in series enables the measurement of changes in mass [72], leading to determination of cell response to drugs [73].

Tables

Tables 1.2 and 1.3 list the parameters relevant for the applications pipetting and mass sensing respectively. Pipetting requires knowledge on the flow rate, deposition resolution, and aperture diameter, wile for mass sensing beam stiffness and quality factor have an effect on the mass sensing sensitivity.

Values that weren't provided were either estimated from the available information or omitted entirely. Estimated values are indicated with an asterix (*). Figures 1.6 and 1.7 show pictures of the devices mentioned in these tables.

Table 1.2: Pipetting parameters of reviewed devices.

Name	**Minimum flow rate**	**Deposition resolution** [nm]	**Aperture diameter** [µm]	**Beam stiffness** [N m^{-1}]	**Channel dimensions** (L; W; H; t) [µm]	**Material** (Beam, tip)
AFM cantilever pipette [24]	5 fL s^{-1}	-	2	4.3	153.5; 3.7; 2.2; 1.35	SiO_2, Si_3N_4
FluidFM [22]	-	-	0.1 - 1	0.1 - 10	150; 10; 2; 0.8	SiO_2, Si_3N_4
Nanofountain Probe [18][19]	-	40	2*	0.05 - 0.5	400; 5 - 7; 0.3 - 1; 1*	Si_3N_4, Si_3N_4
SU-8 microcantilever [27]	-	-	10	0.019 - 1.222	398 - 1598; 96; 8; 6	SU-8, SU-8
SU-8 hollow cantilever V1 [29]	1 nL s^{-1}*	-	4 - 20	0.5 - 80	93 - 493*; 16 - 36*; 3; 4	SU-8, no tip
SU-8 hollow cantilever V2 [28]	0.8 nL s^{-1}	5	20 - 35	150 - 500	236 - 386*; 36 - 66*; 22; 6	SU-8, no tip

Table 1.3: Detection and mass sensing parameters of reviewed devices.

Name	**Q-factor**	**Mass sensitivity** [mHz ag^{-1}]	**Beam stiffness** [N m^{-1}]	**Channel dimensions** (L; W; H; t) [µm]	**Material**
Suspended microchannel resonator (SMR) [64]	$1.5 * 10^4$ (vacuum)	3.33	-	200*; 8; 3; 2 - 3	Si_3N_4
Suspended nanochannel resonator [68]	$1.75 * 10^{4}$* (vacuum)	16.1	29.1	45; 1; 0.4; 1	Si_3N_4
SU-8 based SMR [74]	60 (air)	-	-	200; 14*; 14*; 3	SU-8

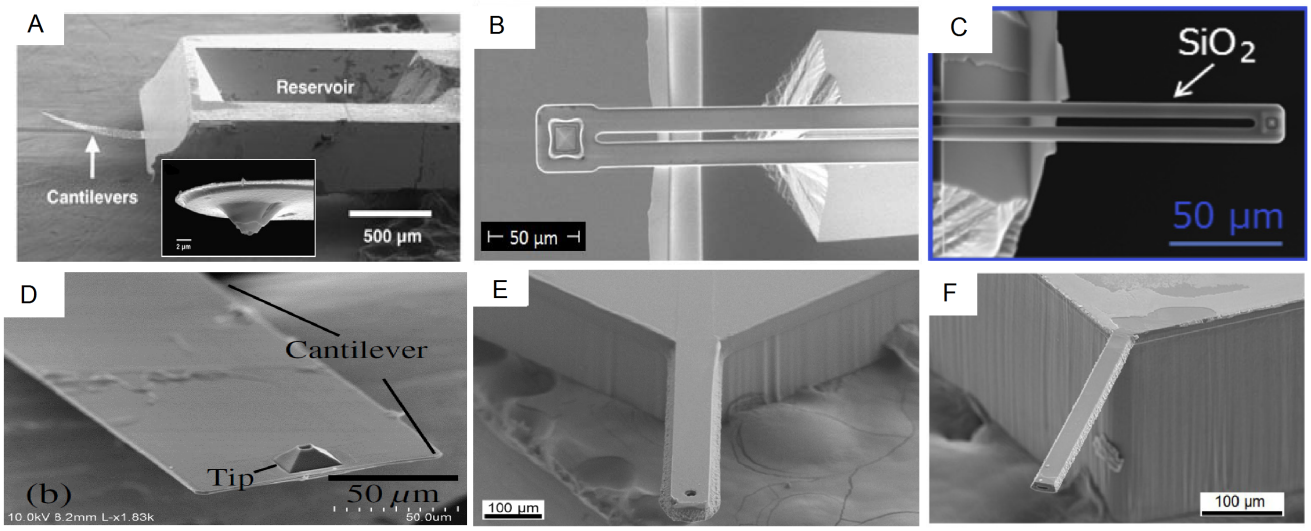


Figure 1.6: Pictures of several hollow cantilevers: **A**) Nanofountain probe [18][19]. **B**) FluidFM [22]. **C**) AFM cantilever pipette [24]. **D**) SU-8 microcantilever [27]. **E**) SU-8 hollow cantilever V2 [28]. **F**) SU-8 hollow cantilever V1 [29].

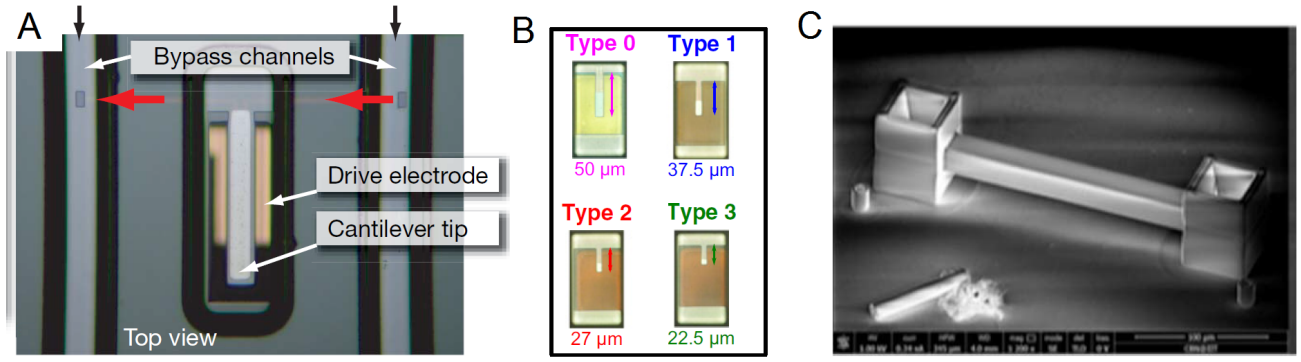


Figure 1.7: Pictures of suspended micro/nanochannel resonators: **A**) Suspended microchannel resonator [64]. **B**) Suspended nanochannel resonators [68], the types correspond to different cantilever lengths. **C**) SU-8 based suspended microchannel resonator [74], the scalebar reads 100 µm.

1.3.2. Fabrication methods

Micro/nanofabrication

The main fabrication method of hollow cantilevers is by micro/nanofabrication. Here, the fabrication of two hollow cantilevers are discussed, the nanofountain probe [19], made from silicon nitride, and the SU-8 microcantilever [27]. These examples are chosen for the reason that they're representative of the micro/nanofabrication method for polymeric and non-polymeric hollow cantilevers.
Figure 1.8 **A** shows the fabrication flow chart of the nanofountain probe. A tip shape is formed by isotropic etching of silicon (**a**, **b**). Silicon nitride is deposited by low-pressure chemical vapor deposition (LPCVD), then a layer of sacrificial silicon oxide (by LPCVD), and again a deposition of silicon nitride is performed to form the microchannel ceiling layer. The channel is closed of by a bird's beak oxidation step, which is a method to control the location of oxide-layer formation, while keeping the edges of the layer relatively smooth. A final layer of silicon nitride is then deposited by LPCVD (**d** - **f**). Potassium hydroxide is used to etch the reservoir in the backside of the wafer, and the tip on the frontside is etched **g**. Finally an oxide wet etch is performed to etch away the silicon oxide in the channel, and to release the cantilever.

The fabrication method for an SU-8 hollow cantilever is described in figure 1.8 **B**. A SOI wafer is oxidized and KOH-etched until the second silicon oxide layer is reached (**a**, **b**). A layer of SU-8 is spun on the wafer, and material for the deflection sensor (Cr/Au/Cr) is deposited, along with the gold electrode (**c** - **e**). A sacrificial layer of photoresist is deposited with a layer of aluminum on top, which serves to isolate the photoresist

from the solvents in the uncured SU-8, and again a layer of SU-8 is spun on top of that (**f** - **h**). The top is bonded unto another wafer, and the bottom silicon/silicon oxide layers are wet and dry etched (**i** - **j**). The channel through the tip is plasma etched, the rest of the silicon is removed, and the channel is cleared from the photoresist and aluminum (**l** - **n**).

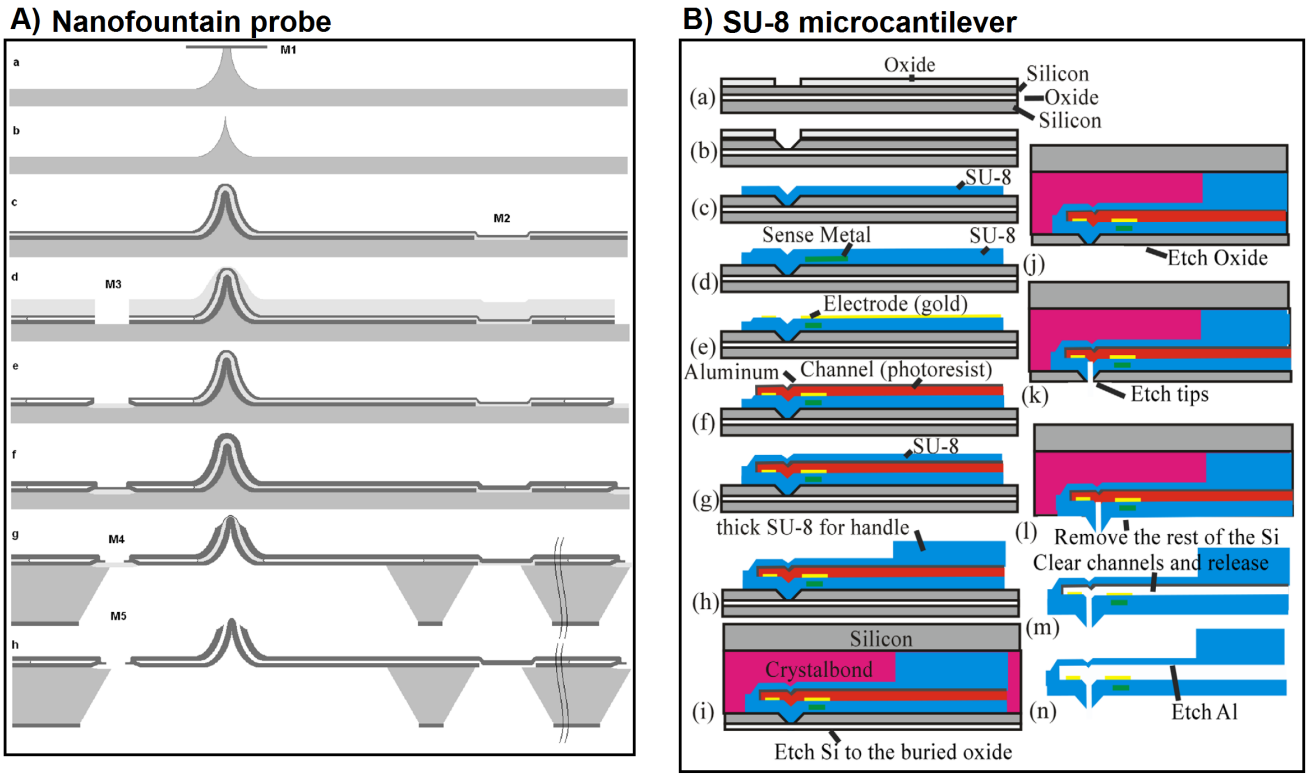


Figure 1.8: Fabrication proces flow of **A**) the nanofountain probe by N. Moldovan, K-H. Kim, and H. D. Espinosa [19], and **B**) the SU-8 microcantilever by A. Gaitas and R. W. Hower [27]. Both images are reproduced from their respective papers.

Two photon polymerization

Three-dimensional writing has been exploited for applications in microfluidics, for example spiral shaped internal channels [75], and 3D micromixers [76]. More microfluidic applications have been reviewed elsewhere [40] [77]. Other applications include tissue engineering [78] [79] [80] [81], photonics [82], light robotics [83], and micromechanical applications, for example light-weight reusable microlattice shock absorbers [84], and magnetically controllable micro/nanomachines [85].
Suspended micro cantilevers have also been fabricated by 2PP [86] [87] [88] [89].
Material properties like the Young's modulus, Poisson's ratio, and density of a photoresist are all dependent on the laser power that is used during the 2PP process [90], therefore this should be taken into account during design and modelling.

Pros and cons of the techniques

In research, using micro/nanofabrication techniques for prototyping comes with a high cost in time, taking up to several weeks, depending on the amount of fabrication steps involved. A benefit is that these techniques result in a large batch of nearly the same structures. Complex structures fabricated with stereolithography take far less time, usually a few hours to several days, and can often be done in-house. However, photolithography is able to fabricate the smallest features, down to tens of nanometers, with two photon polymerization techniques near the hundred nanometers, and stereolithography in the tens of micrometers. Another drawback for stereolithography and 2PP are the materials; they have to be photo polymerizable for 3D printing. Micro/nanofabrication is not limited to only polymers, and the technique is able to create metal structures. The choice of fabrication method depends on the desired goal, and if a well-established design with nanometer precise features is desired, then micro/nanofabrication is suitable. For rapid prototyping purposes and

three-dimensionally shaped features stereolithography fulfills that goal, and for sub-micrometer size features combined with meso-scale (100-1000 mm) features two-photon lithography is suitable.

1.3.3. Characterization methods

Fluid flow measurements

Characterization methods of the parameters listed in table 1.2 are subdivided here in two parts, flow- and dynamical methods. For the application of pipetting the relevant parameters are minimum flow rate, deposition resolution, and hollow beam aperture size.

Flow rate

Flow rates can be measured from the movement of the fluid meniscus and the frame rate, from which the velocity can be calculated. The volumetric flow rate can then be found by multiplying the velocity with the channel cross-sectional surface. A similar scheme is followed here [24]. The small channel sizes can result in very high flow speeds, resulting in the need for a high speed camera.
Another approach is to add a cantilever inside the channel which is positioned perpendicular to the flow. The deflection of that internal cantilever is directly proportional to the flow, and different cantilever designs have been proposed and tested [91] [92], with resolutions down to $3\,\mathrm{nL\,min^{-1}}$ and $1.3\,\mu\mathrm{L\,min^{-1}}$ respectively. Noeth measures the cantilever deflection similar to what is done in an AFM, a laser beam is reflected from the surface, while Sadegh Cheri optically measures the change in intensity, when a beam is reflected back through an optical cable. The fact that an extra structure must be incorporated into the design is a drawback due to the micro/nano-sized dimensions of the channels. A benefit would be the ability to continuously monitor the flow speed.

Deposition resolution

The smallest deposited feature width reported was 40 nm with the nanofountain probe [18], and these ink lines were imaged with the same tip that deposited them. Deposition resolution can depend on the residue after evaporation of the solvent, and solutions in liquids of low volatility can be used to reduce the evaporation rate of femtoliter droplets, which happens in a few seconds [93]. Another dependency of the resolution is the contact time of a tip with a hydrophobic substrate [94].

Pipetting can be performed when the cantilever is not vibrating, however, the internal flow speed can cause cantilever vibrations. This itself can interfere with liquid depositing, and care should be taken not to exceed a certain critical flow velocity, beyond which the cantilever vibrations become unstable. For slender elastomeric pipes with a length/outer diameter ratio of 100, these critical velocities are $\sim 10\,\mathrm{m\,s^{-1}}$ [33], which are speeds far exceeding the flow speeds in the range of $\mu\mathrm{m\,s^{-1}}$ - $\mathrm{mm\,s^{-1}}$ that are commonly used in hollow cantilevers.

Aperture size inspection

The often sub-micrometer dimensions of tip apertures require imaging techniques like the scanning electron microscope (SEM) and AFM to inspect it, however, both are slow compared to optical techniques. The SEM requires a conductive sample, therefore polymer structures must be sputtered with a conductive layer first, and imaging with an AFM is not time efficient for relatively large surfaces. Other techniques like white light interferometry have been suggested and compared [95], if a quick quantitative impression of the structure is desired.

Dynamical measurements

The frequency spectrum containing the structure's eigenfrequencies is used to determine beam stiffness, quality factor, and mass sensitivity. A way to obtain frequency information is to use laser Doppler vibrometry, which is a technique where the doppler shift between a reference- and reflected laser beam contains information on the frequency of an oscillating object. This technique has been used for the characterization of 2PP polymer suspended microresonators [74]. Mass measurements are performed by measuring the frequency shift in a resonance peak that occurs when mass is added to a cantilever.

1.4. Conclusion

In conclusion, hollow AFM cantilevers have been described in literature that are capable of continuously dispensing and aspirating fluid volumes down to several femtoliters per second. The fabrication materials are mainly silicon oxide and silicon nitride, but SU-8 cantilevers have also been successfully fabricated. All of the investigated AFM cantilevers have been fabricated using micro/nano fabrication techniques that are limited

to 2D-design, expensive, and slow, therefore unsuitable for rapid prototyping, compared to 3D fabrication techniques. The precision down to tens of nanometers that is offered by micro/nanofabrication makes it a suitable for planar designs with that structural precision. However, cost-effective rapid prototyping is better suited for stereolithography and two photon polymerization, with the former offering a structural resolution in the tens of micrometers, and the latter sub-micrometer resolution. These 3D printing techniques enable three dimension designs that are not possible with planar micro/nanofabrication techniques.
Applications have been discussed including pipetting, imaging, detection, and mass measuring, and the first three have been demonstrated for polymer cantilevers. From these applications, parameters have been distilled that are important for fabrication and functionality, including flow rate control, deposition resolution, aperture diameter, beam stiffness, channel dimensions, and the material.
Knowledge about the beam stiffness is important for force spectroscopy and the dynamics of the cantilever, and for surface imaging the tip radius is of importance. Sensitive mass sensing requires a high quality factor, and the medium in which the mass measurement is performed has a large influence on the quality factor.

Three dimensional laser writing has not yet been used to fabricate hollow AFM cantilever pipettes. Its versatility in design creates the possibility of combining functionalities, for example, suspended nanoparticles or cells could be weighed, deposited, and examined by force spectroscopy with a single device. However, to make this possible, a polymeric hollow AFM cantilever has to be designed and 3D-printed, and its fluidic- and mechanical functionality has to be characterized.

1.4.1. Research questions

The identification of knowledge gaps following from this literature review leads to the formulation of a main research question and several sub questions.

"How can a polymeric hollow cantilever be fabricated with 3D-printing that can manipulate sub-picoliter volume fluids with a one-step connection to the external world?"

The main research question can be divided into the following sub-questions:

1. How can two photon polymerization be integrated with stereolithography to construct functional fluidic structures?

2. What are the values of the physical characteristics of such hollow structures? (e.g. stiffness, quality factor, and flow rate)

Risks and mitigation

There are possible roadblocks that can prevent the answering of the research questions, and some of these risks are listed here with a mitigation strategy.

1. Detachment of the hollow two photon polymerized-structures from the stereolithographic fluidic interface.
   → 2PP 3D-printing of the interface and the cantilever as one whole, instead of only a cantilever.

2. Excessive bending of the cantilever by residual stresses.
   → Adjust the 3D-printing layer-slicing directions and/or voxel path.
   → Reduce the stresses by adding another layer to offset the asymmetry in stresses.

   Collapsing of cantilever channels.
   → Redesign by upscaling the dimensions of the rectangular channels, or thicker walls.
   → Redesign the shape of the cantilever and channel to circular or triangular.

3. No fluid flow due to blocked channels.
   → Test with a different fluid.
   → Redesign with larger channel dimensions.

Leakage.
→ Adjust printing speed of the entire cantilever, or only at 'vulnerable' parts.
→ Add an extra 2PP 3D-printed layer to the weaker parts of the structure.

4. Low/no amplitude signal from the laser Doppler vibrometer due to optical transparency of the polymer.
   → Sputter coat a reflective layer onto the cantilever.

5. Low/no amplitude signal from the laser Doppler vibrometer due to low energy transfer to the cantilever tip by the piezo-element.
   → Lower the speed at which the frequency spectrum is sweeped.
   → Redesign the cantilever such that it has an increased stiffness.

2

Paper

Multiscale 3D-printing of a suspended polymer microfluidic device

Robert C. L. N. Kramer

Department of Precision and Microsystems engineering, Faculty of Mechanical, Maritime, and Materials Engineering, Delft University of Technology, Delft, The Netherlands

Suspended hollow micro-cantilevers have been employed for zeptogram (10^{-21} g) mass measurements, pipetting of femtoliter (10^{-15}L) volumes, and studies on mechanical interaction with single cells. The main fabrication method of these devices is by standard clean room micro/nano fabrication techniques, however, they are inherently planar, thus limiting three dimensional design, and the required masks make prototyping time-consuming and expensive. In this work maskless 3D-printing by two-photon polymerization (2PP) was used to fabricate hollow microfluidic cantilevers. A novel fluidic interfacing approach was developed by directly 2PP-printing the cantilever on a stereolithographic microfluidic device for handling and connecting to the external world. Several 350 µm long cantilevers with an aperture of 25 µm were mechanically characterised by laser Doppler vibrometry and the fundamental frequency was measured at 99.6 kHz, with a quality factor of approximately 174 in air. A hydraulic model was constructed and fluidic functionality was demonstrated. The non-optimised printing time of the full device was approximately 2.5 hours, performed by only two automated maskless fabrication steps. This printing method enables rapid prototyping of ready-to-use suspended microfluidic devices.

1 Introduction

Hollow atomic force microscope (AFM) cantilevers have been employed for controlled continuous depositing and aspirating of volumes of liquid as small as several femtolitres (10^{-15} L) [1]. Combining these functionalities with atomic force microscopy (AFM) enables the precise positioning and sensitive force control of such devices, and enables direct imaging of the deposited substance. The fine control over the force and pipetted volumes make the device suitable for investigation of cellular functions by extracting or injecting fluids without any significant disturbance to the cell [2] [3]. Hollow cantilevers have also been able to deposit and pattern single cells [4]. Other applications include the local synthesis of gold nanoparticles [5], and submicrometer patterning of lines of functionalized gold-, and diamond nanoparticles [6] [7].
By measuring shifts in the eigenfrequencies of suspended resonating hollow cantilevers changes in its geometry or mass can be determined, and this effect has been used to perform zeptogram (10^{-21}) accurate mass measurements in near vacuum [8].
These, and the previously mentioned microcantilevers have all been fabricated by standard micro/nanofabrication techniques, in which repeated steps of deposition, photolithographic patterning, and etching result in micrometer-sized structures. The advantages are that nanometer precise patterns can be created over an entire substrate per step, and it offers precise control over the shape and size of the structure. Because of these techniques cantilevers are mainly fabricated from silicon, silicon oxide, and silicon nitride, but also from the photopolymer SU-8 using similar methods [9]. The fabrication steps can involve highly toxic and corrosive chemicals, and usually require high-maintenance infrastructure such as clean rooms. For each step a patterning mask is required, and for any change in design a new mask must be fabricated, which raises the cost of prototyping. The designs for the cantilevers are also limited in height, as material depositions are usually only several micrometers thick.

A fabrication technique that allows for more flexibility is 3D-printing. It offers rapid and cost-effective prototyping, lower equipment cost, and it is a single-step process. The added degree of freedom in the design space allows for out-of-plane designs not feasible with standard micro/nano-fabrication.

In this work two 3D-printing techniques have been used, namely stereolithography (SL) and two-photon polymerization (2PP), which are able to print with micrometer resolution. In both techniques a laser illuminates a liquid photoresist, thereby polymerizing it locally to form a solid structure. Commercial SL-systems can offer smallest structure details of 20 µm[10], and in research set-ups 0.43 µm was reported [11]. With this technique microfluidic devices have been fabricated with both passive and active components [12]. 2PP-systems can reach even lower resolutions, and line-widths of ∼23 nm has been reported[13]. Such low resolutions are possible through non-linear photon absorption of the resist, and this effect enables surface-free 3D-printing, which is a benefit it has over SL. Using 2PP, embedded microfluidic channels with internal pillar structures have been fabricated for trapping of biological entities [14], as well as a doubly-clamped suspended microchannel resonator [15]. Integration of

2PP-structures into microfluidic SL-devices has recently been reported, where a suspended microfilter was printed inside an SL-plate with an open channel and clamped between two sheets of polymethylmethacrylaat (PMMA) [16].

However, microfluidic functionality has not yet been shown for 2PP-written suspended hollow structures, nor have they been integrated onto a SL-printed microfluidic device. Employing 2PP as a fabrication method enables rapid prototyping of such structures, while the integration onto a SL-printed microfluidic device creates a ready-to-use product within these two automated fabrication steps.

In this work, a 2PP-written hollow microcantilever was directly printed onto an SL-printed microfluidic device, which provides the interfacing connection to external tubing, a concept of it is shown in figure 1. The materials used for both fabrication methods are different acrylic-based photopolymers, and therefore adhesion between the 2PP- and SL-prints was investigated. A hydraulic model of the complete device was constructed and evaluated. The 2PP-printed hollow cantilever was mechanically characterized, and its fluidic functionality was shown.

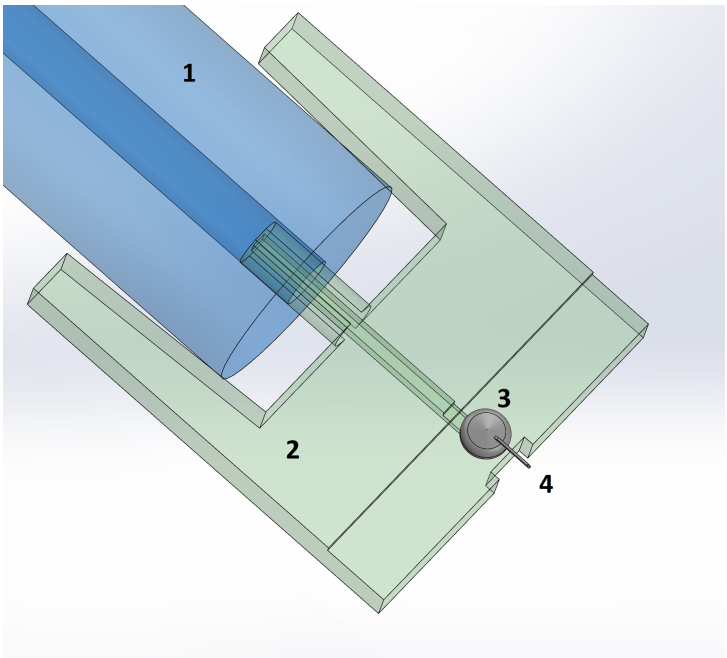


Figure 1: Schematic picture of the concept. The connected external tubing is labelled as **1**, the SL-interfacing device as **2**, a 2PP connection between the interfacing device and cantilever as **3**, and the cantilever itself as **4**.

2 Materials and methods

2.1 Stereolithography

Liquid photo resists contain a mixture of monomers, oligomers, and photoinitiators. When the photo-initiator molecule absorbs a photon, it raises the energy level of one of its atoms, and that breaks a carbon-carbon bond. These radicals can then form bonds with the monomers and oligomers and form a solid material. Stereolithography printing is based on this principle, and structures are formed through layer-by-layer laser illumination at the surface of a liquid photoresist. With this method a microfluidic interfacing device can be printed that serves as the connection between the hollow cantilever and fluidic tubing. The computer aided design (CAD) is shown in figure 2, together with an expanded view of the designed aperture. The dimensions of the device are chosen such that it can still be handled by tweezers and that the tubing can be connected by hand.

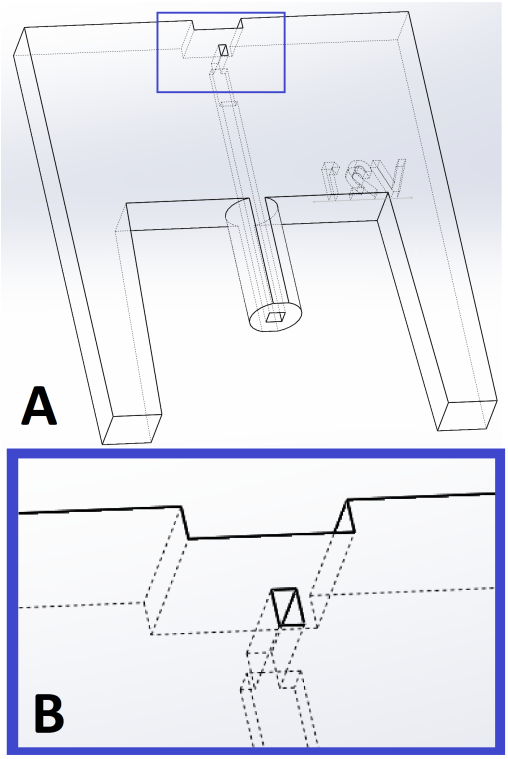


Figure 2: **A)** The CAD of the SL-printed interface is shown where the internal channel is visible in the middle of the device and ending in the aperture at the top. **B)** An expanded view of the rectangular aperture that is connected to the internal channel.

A commercial desktop stereolithography printer (EnvisionTEC GmbH. Micro® Plus Hi-Res) is used with a reported

minimum xy-resolution of 30 µm and z-resolution 25 µm. The fabrication material is a methacrylate/acrylate-based resin (HTM140V2M, EnvisionTec GmbH.) that was designed to attain these resolutions.

Compressed air is used to remove excess resin after printing, and after that it is immersed in isopropyl alcohol (IPA) and placed in an ultrasonic cleaner for two minutes. Scaffolding has to be designed that has to be able to withstand these cleaning steps, and such a scaffold is shown in the supplementary.

2.2 Two photon polymerization

Stereolithography has a fundamental limit to its resolution; it is limited by diffraction, which is the bending of light around corners of an object or aperture. This determines the smallest focal spot, and thus the volume which is illuminated. However, unwanted polymerization also occurs in the light cone around the laser focus, and therefore the focal point is positioned near the bath surface in conventional stereolithography. This ensures that the next layer of photoresist isn't partially polymerized by the previous illumination step.

A way around this limitation is the use of a technique called two-photon polymerization (2PP). Photons of lower frequency are used that don't have sufficient energy to start the polymerization reaction separately, therefore it occurs only if two are absorbed by the same initiator molecule within roughly 1 fs [17]. The chance of this occurring drops non-linearly further away from the laser focus, which reduces the resolution to below single micrometers.

A 2PP-printer (Nanoscribe GmbH. photonic professional GT) with sub-micron resolution is used for printing of the yurt/cantilever, shown in figure 3 **A**, and the base structure that connects to the aperture of the SL-interfacing device, shown in figure 3 **B**.
The yurt and base were designed to make use of the full 400 µm circular writing field of the microscope objective (25x magnification) to maximize the attached surface area. The rectangular slits in the base are implemented to mitigate the problem of bubble formation during printing. When this methacrylate/acrylate-based material is illuminated by the 100 to 200 femtosecond laser it will locally ablate and directly transform the material in a gaseous plasma [18] that reforms into gaseous carbon compounds. Large bubbles can block the laser from printing parts, but the slits can prevent the small, initially formed bubbles from coalescing. The photoresist that was used as material is a carbamate/methacrylate-based resist (IP-S, Nanoscribe GmbH.).

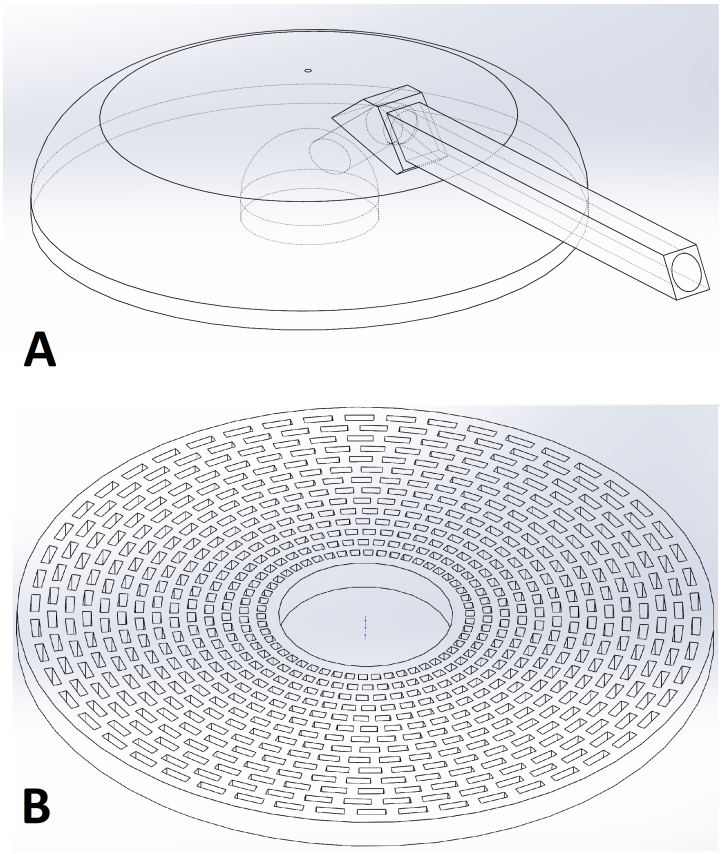


Figure 3: **A)** Dome and cantilever design. A 25 µm channel runs through the cantilever towards the base, shown in **B**, thereby fluidically connecting it with the SL-interfacing device.

To print the yurt/cantilever and the base on the SL-interfacing device a hanging structure configuration is used which is called "Dip-in laser lithography" (DiLL), and it is schematically shown in figure 4. The SL-interfacing device is taped to the bottom of an indium-tin-oxide (ITO) coated glass slide and immersed in the photoresist. The microscope objective is then directly dipped into the same resist droplet. Printing settings are shown in table 1 and a further explanation can be found in appendix **A**.

Table 1: 2PP-printing parameters

Parameter	**Value**
Laser power	20 mW
Scanning speed	60 mm s^{-1}
Objective	25x NA 0.8
Slicing distance	0.5 µm
Hatching distance	0.3 µm
Contour count	3
Contour distance	0.2 µm

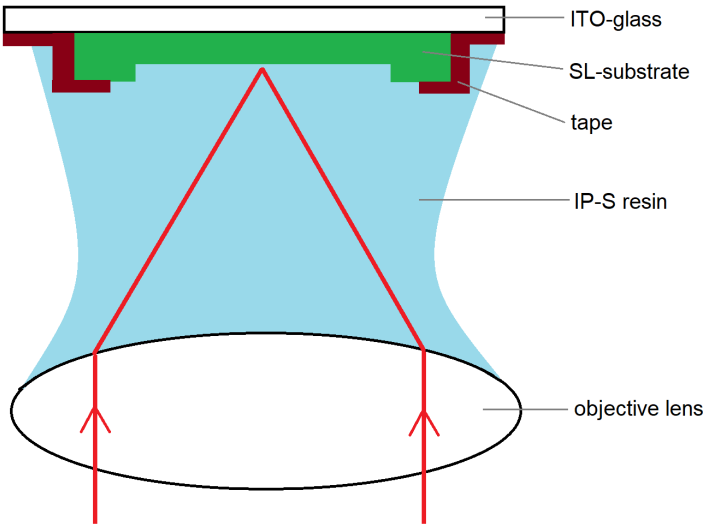


Figure 4: DiLL configuration. The SL-interfacing device is taped to the bottom of the ITO- coated slide, then immersed in the resin. This figure is not to scale.

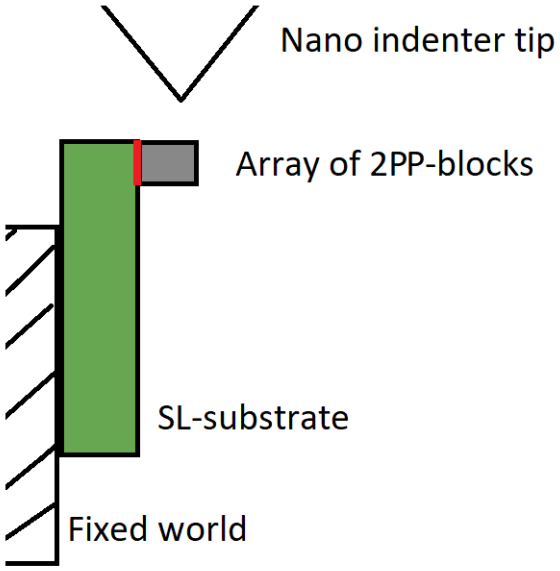


Figure 5: Schematic side-view of the adhesion experiment. The red strip indicates the attached area under test. Five cubes for each of the dimensions 10 µm^3, 50 µm^3, 100 µm^3, and 200 µm^3 have been printed accordingly. The SL-substrate was glued onto a fused deposition modelling (FDM) 3D-printed structure, as shown in the supplementary.

2.3 Adhesion strength

The strength of adhesion between the 2PP-written base and the SL-interfacing device was investigated by printing an array of 2PP-cubes onto a SL-printed slate, in the manner as shown in figure 5. This slate was quick-glued onto a fused deposition modelling (FDM) 3D-printed pentagon, shown in the supplementary.
The experiment was performed with a nano indenter (Nano Indenter MTS G200) using a Berkovich-tip that pushed against the side of a cube, and it recorded the force and distance until some time after the cube detached from the SL-substrate. A load-range from zero to 500 mN in steps of 1 mN was applied on every cube.

2.4 Mechanical characterisation

The hollow cantilever is mechanically characterised with a laser Doppler vibrometer (LDV) to obtain its frequency response. The LDV points a laser beam onto a vibrating surface and is scattered back with a slight frequency shift due to the Doppler effect. Recombination of the reflected beam and a reference beam causes an interference pattern which contains information on the velocity and frequency of the vibrating surface [19]. The LDV laser beam was focussed near the tip of the cantilever, at the middle of its width, where the amplitude of the fundamental mode is largest.
Three cantilevers were loaded onto a piezo-resistive element which was actuated by an A/C signal of 10 volt over a frequency range from 50 kHz to 150 kHz. To mitigate insufficient reflection due to the transparent cantilever material an 18 nm gold/palladium layer was sputter coated onto it.

2.5 Fluidic characterisation

A hydraulic model is proposed to characterise the fluidic capabilities of the device. Because of the physical similarities between flow rate, current, pressure drop, and voltage, an electrical circuit can be constructed [20]. Hydraulic resistance determines how much fluid flows through a channel when pressure is applied, while hydraulic capacitance relates to the temporal storage of liquid through expansion of the channel dimensions under pressure. Theory on these concepts can be found in the appendix. The electric circuit is shown in figure 6 **A**, and the subdivision of the channels in the device is shown in 6**B**.

In the experiment a syringe was filled with deionized water and loaded into a syringe pump. The syringe was connected by tubing to the SL-interfacing device as illustrated in figure 1. Flow rates of 0.5, 1, 2, 5, 10 µL min^{-1} were set and these were measured by making videos of the moving meniscus of the fluid in the cantilever.

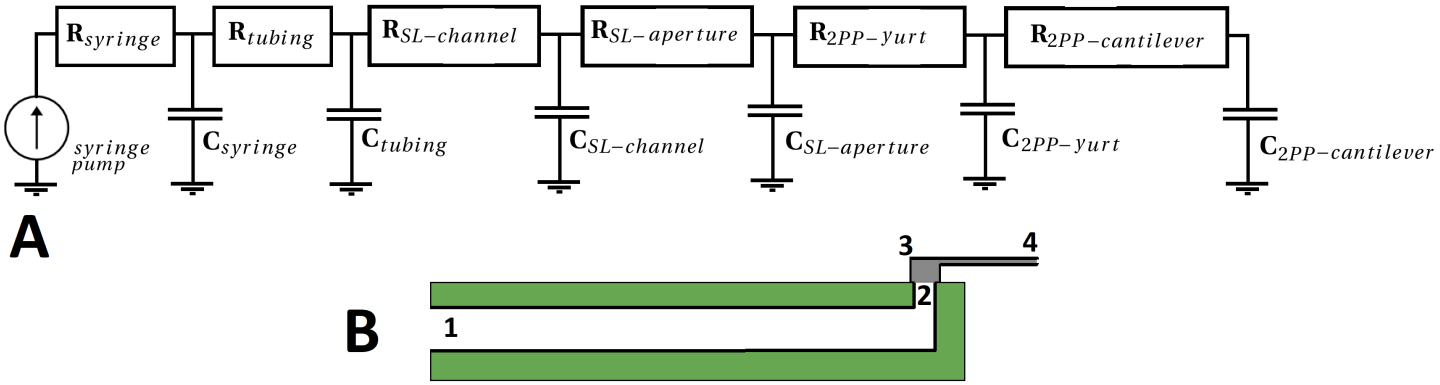


Figure 6: **A)** Electrical circuit model of the device, in which a syringe pump is modelled as a current source and where the components are separated based on the channel dimensions. This is illustrated in **B**, where **1** denotes the SL-channel, **2** the SL-aperture, **3** the 2PP-yurt channel, and **4** the cantilever channel. All channels are modelled as being cylindrical, with the exception of the rectangular SL-aperture.

3 Results

3.1 SL results

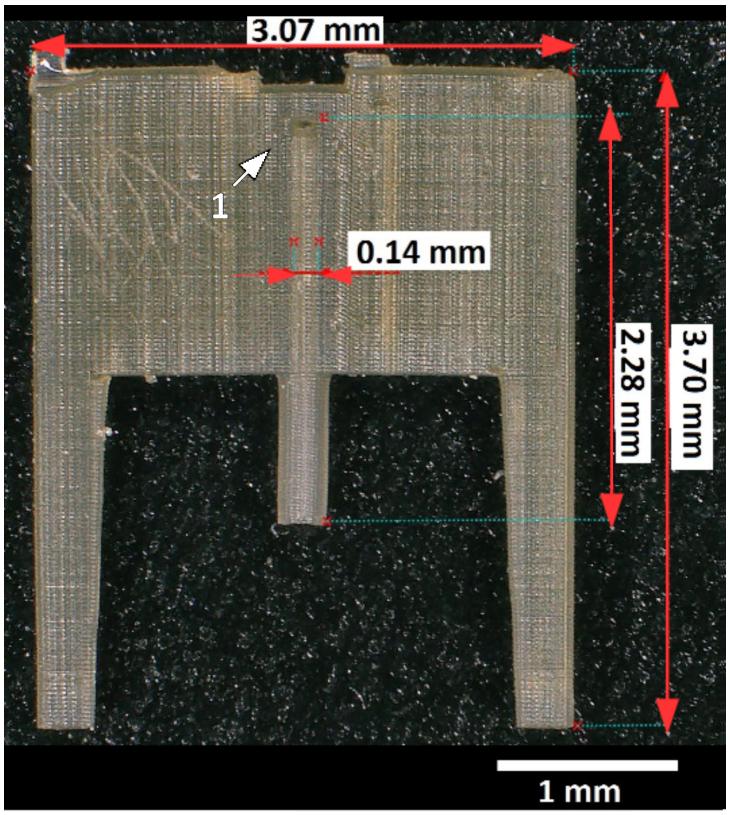


Figure 7: Picture of the underside of the SL-interfacing device; the location of the aperture is indicated at **1**. The internal channel has a diameter of approximately 0.14 mm and a length of 2.28 mm.

The SL-interfacing device is printed with the channel perpendicular to the build plate, and an image is shown in figure 7, including some of its dimensions. These were chosen such that the device can still be handled by tweezers and that the tubing can be connected by hand. Other dimensions are a thickness of 400 µm, and an aperture of approximately 150 µm wide and 90 µm high.

Each printing session resulted in 30 devices, and it will take approximately 2 hours and 10 minutes for a single job. The printing time per device is then close to 4.33 minutes.

3.2 2PP results

For the printing of the 2PP features a strategy was devised and is summarised as follows:

1. Prepare the ITO-glass sample by rinsing it with acetone and IPA.

2. Tape the SL-substrate on the glass at a location 5+ millimeter away from the center and deposit a drop of resist, as was illustrated in figure 4.

3. Approach the glass with the objective and focus the laser in the center of the glass surface.

4. Lower the microscope further than the combined height of the SL-substrate and the tape, then move the objective under a SL-substrate.

5. Print test rectangles at incremental heights until the surface of the substrate is reached, figure 8 clarifies this step.

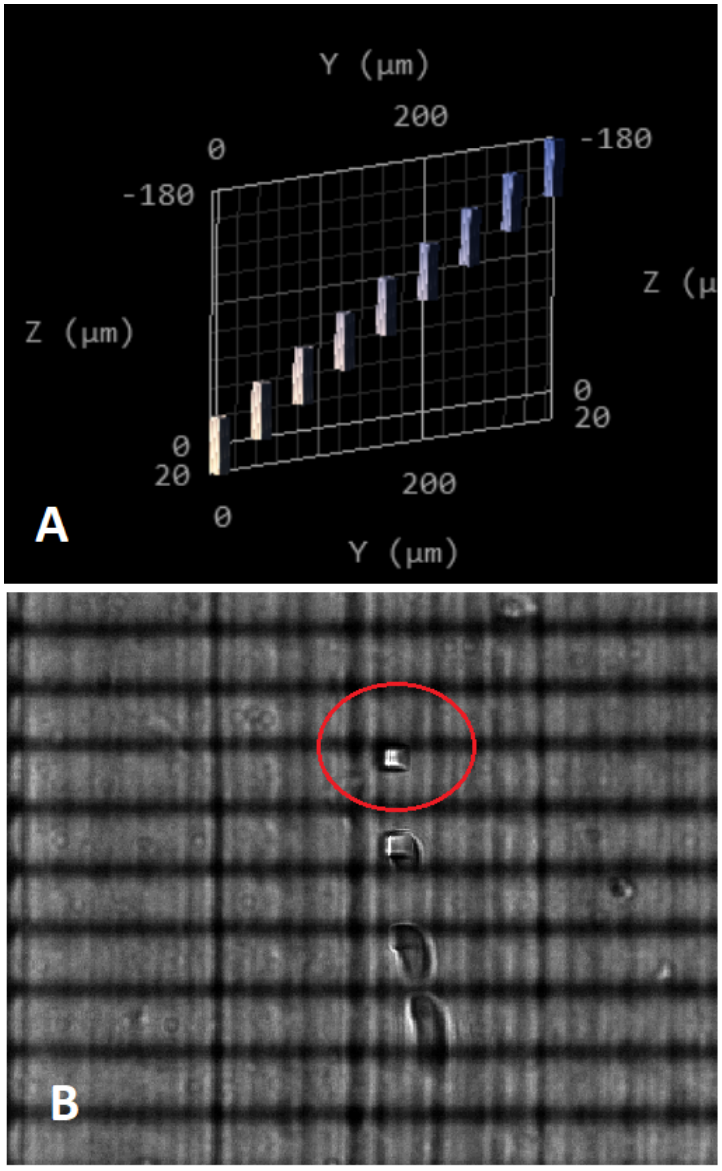


Figure 8: **A)** A view of how the height test is designed. the rectangles are printed at incremental heights of 20 µm until the first rectangle is shown to be attached, as illustrated in **B**. The microscope feed from the 2PP-printer is shown here, with the individual printing layers of the SL-substrate visible as horizontal bands. The first three rectangles were not printed on the substrate and remain suspended in the resin, but the fourth was attached. An indicator of this is the movement of the rectangle when the laser repositions, which moves the viscous resin and the unattached rectangles within it. An attached rectangle will not move or change shape.

After determining the correct height the base structure was printed around the aperture, and a picture is shown in figure 9.

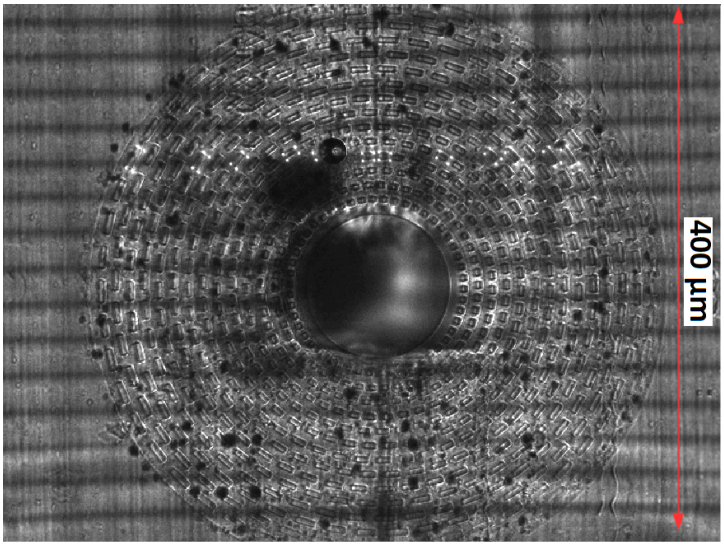


Figure 9: Picture of a base structure 2PP-printed around the SL-aperture. The damage to the SL-surface caused by the laser illumination is visible as small black circular spots with a burned appearance. At those locations gas-bubbles had formed and dissolved in the resist, leaving only the spots.

At a height where no more laser illumination occurs inside the SL-substrate the yurt and cantilever were printed. A SEM-picture of those is shown in 10 **B** and **C**, with the final device fully connected to fluidic tubing shown in 10 **A**. Dimensions for the yurt and cantilever are listed in table 2 respectively.

Printing time of the 2PP-base, yurt, and cantilever was approximately 2.5 hours, with a development time of 48 hours.

Table 2: Yurt and cantilever dimensions

Yurt	
outer diameter	400 µm
wall thickness	50 µm
height	140 µm
inner cylinder diameter, height	100, 50 µm
attachment surface area	79630 μm^2
Cantilever	
width, height, length	30 µm, 30 µm and 350 µm
inner diameter	25 µm
channel length	436 µm
volume	$1.43 \times 10^{-13}\,m^3$
density	$1.2\,g\,cm^{-3}$
mass	172 ng

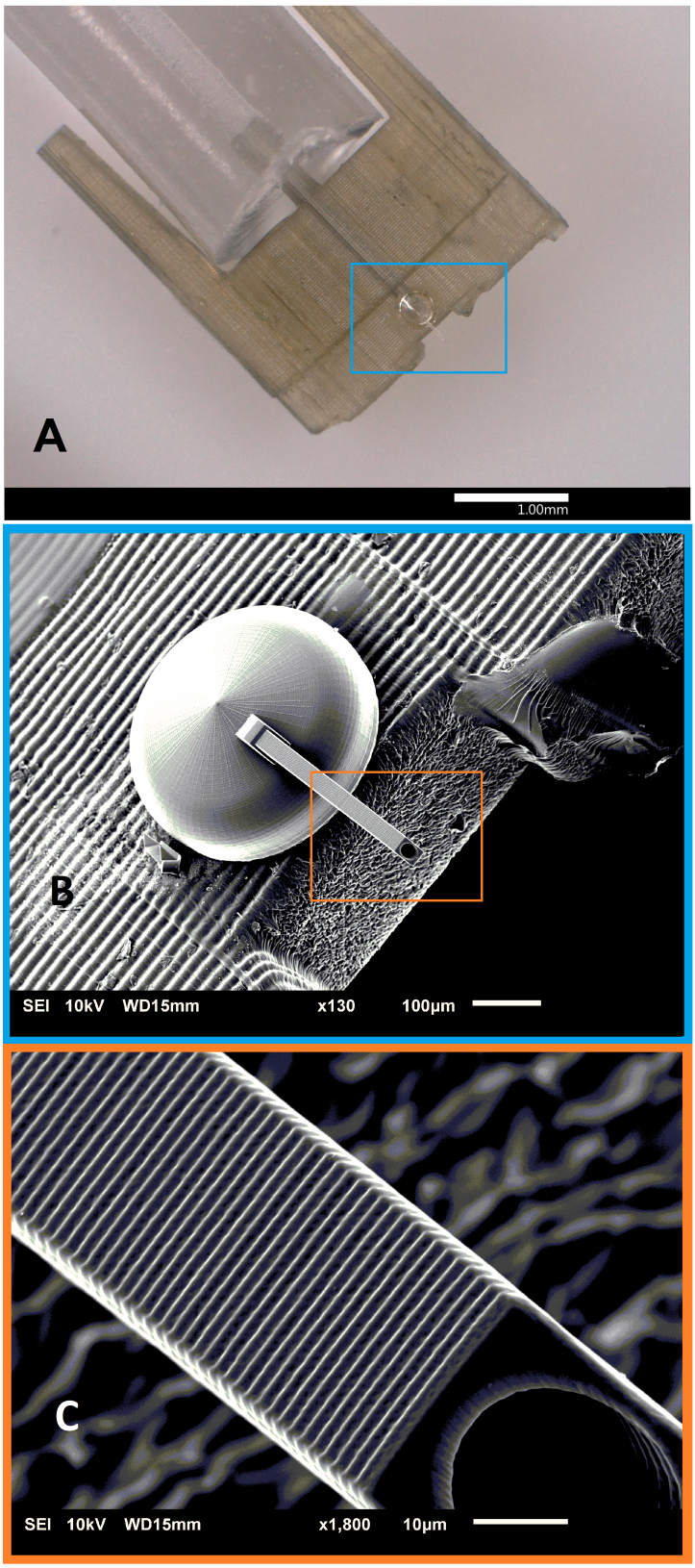


Figure 10: **A)** Picture of a cantilever printed onto a SL-interface that is connected to an external pressure source. **B)** SEM-image of the 2PP-yurt and cantilever. **C)** SEM-image near the tip of the cantilever.

3.3 Adhesion results

The printing of the 2PP blocks of 10 µm^3, 50 µm^3, 100 µm^3 and 200 µm^3 resulted in samples as shown in figure 11, and nano indentation measurements yielded the following graph in figure 12. Four 100 µm^3 blocks were detached, as well as two 200 µm^3 ones.

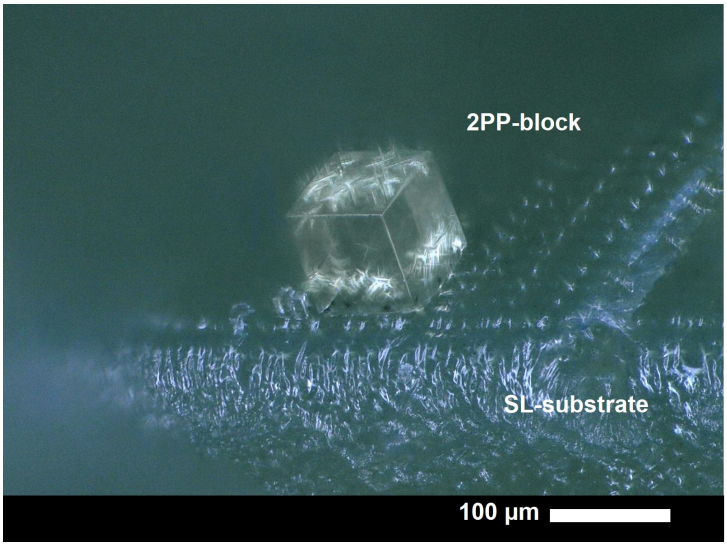


Figure 11: 3D composite picture of a 100 µm^3 2PP block that was printed on a SL-substrate. The blocks with other dimensions were printed in a similar manner.

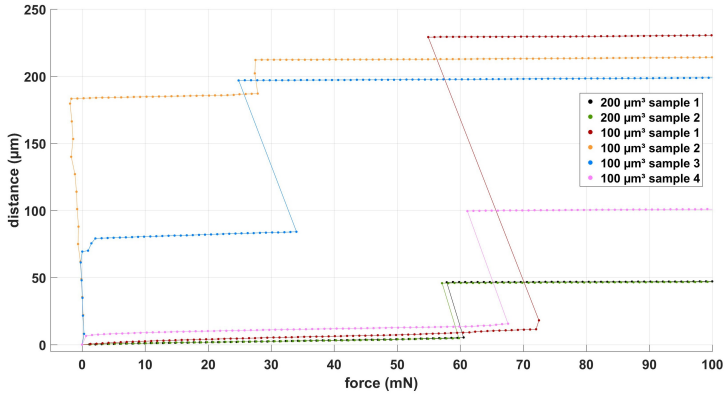


Figure 12: Results from the adhesion experiment for two 200 µm^3 blocks and four 100 µm^3. Distance is plotted against the force and the detachment of the blocks is indicated by the sudden jump in distance.

3.4 Mechanical results

The laser Doppler vibrometry experiment resulted in the frequency response of the cantilever shown in figure 13. Two

other cantilevers have been tested, and those results can be found in appendix **B**, together with magnitude (dB) - frequency graphs around the fundamental frequency.

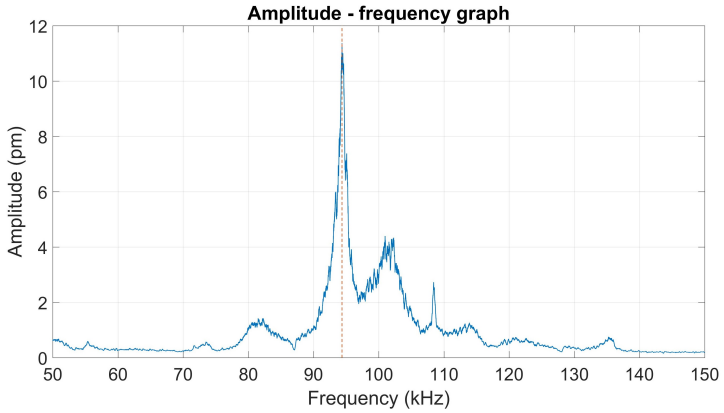


Figure 13: This figure shows the frequency response of the cantilever, with the frequency of the first mode at 94.3 kHz indicated with at the vertical red dashed line. A frequency sweep was performed over the band 50 kHz to 150 kHz.

3.5 Fluidic results

Fluidic functionality of the cantilever is shown by filling it, as seen in figure 14.

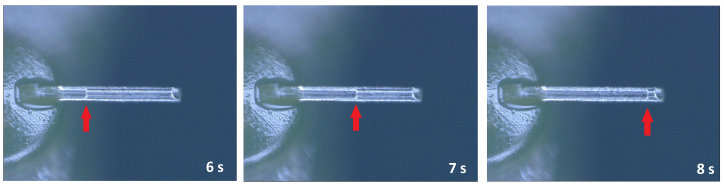


Figure 14: Photo series of the filling of the cantilever. The yurt is seen on the left, with the transparent cantilever and aperture on the right. The meniscus is moving to the right inside the channel, as indicated by the red arrows.

The total circuit resistance is $6.09 \times 10^{13}\,\mathrm{Pa\,s\,m^{-3}}$ and the RC time constant of the circuit was calculated as 0.0319 s. Separate values for the fluidical circuit elements are listed in table 3.

Table 3: Fluid volumes, fluidic resistances, and capacitive values of the circuit.

	Volume	Resistance $\left[\frac{\mathrm{Pa\,s}}{\mathrm{m^3}}\right]$	Capacitance $\left[\frac{\mathrm{m^3}}{\mathrm{Pa}}\right]$
Syringe	1000 µL	$4.88 * 10^{6}$	$6.45 * 10^{-16}$
Tubing	13.7 µL	$1.49 * 10^{13}$	$2.14 * 10^{-15}$
SL-channel	32.5 nL	$3.50 * 10^{11}$	$9.71 * 10^{-21}$
SL-aperture	1.82 nL	$2.37 * 10^{10}$	$5.44 * 10^{-22}$
2PP-yurt	0.38 nL	$1.97 * 10^{10}$	$8.25 * 10^{-23}$
2PP-cantilever	0.214 nL	$4.56 * 10^{13}$	$4.66 * 10^{-23}$

Figure 15 graphs the flow rate against the pressure. Five measurements were performed for five set flow rates of $0.5\,\mu\mathrm{L\,min^{-1}}$, $1\,\mu\mathrm{L\,min^{-1}}$, $2\,\mu\mathrm{L\,min^{-1}}$, $5\,\mu\mathrm{L\,min^{-1}}$ and $10\,\mu\mathrm{L\,min^{-1}}$. The pressure was calculated with these flow rates and the total hydraulic resistance of the device.

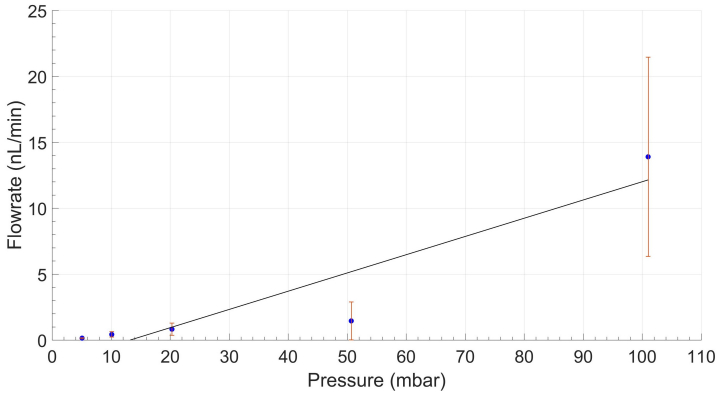


Figure 15: Graph of flow rates plotted against pressure. Five sets of five flow rates were measured and this graphs shows the average per flow rate with each standard deviation as error bars. The black line indicates a least squares curve fit through the data points.

4 Discussion

4.1 SL-device

The specifications of the SL-printer list the minimum in-plane (x and y) resolution as 30 µm, and 25 µm out of plane, however, it was found that this does not hold for internal channels. The minimum channel dimensions differed depending on its orientation, and if a channel is printed parallel to the build plate (in-plane), then the dimensions were 150 µm and 90 µm in the x and y direction respectively. The minimum dimensions for a channel perpendicular to the build plate (in z direction) was a circle with a diameter of 130 µm, shown in figure 16.
It was also found that a minimum square channel of 130 $\mu\mathrm{m}^2$ in the z-direction was printed as circular. This can be ex-

plained by the fact that some non-polymerised resist still remains in the corners of the channel, after developing with isopropyl alcohol (IPA). That resist remains after blow drying and it will be polymerised in the subsequent UV irradiation step.

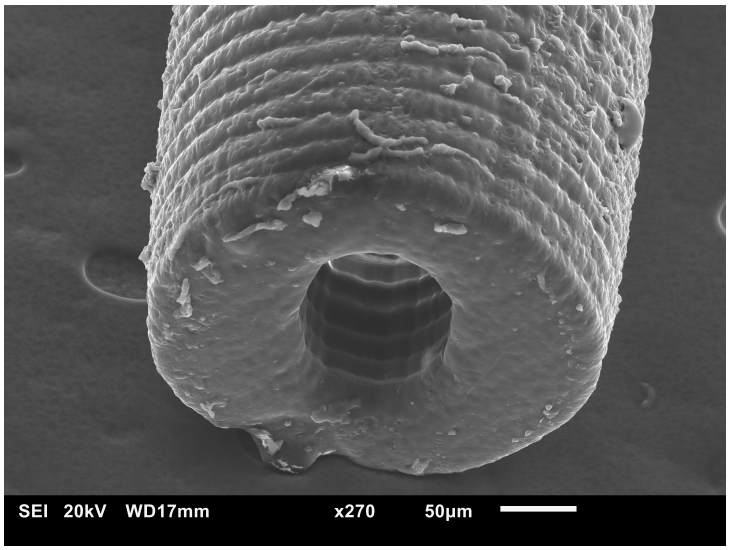


Figure 16: SEM-picture of the fluidic connection between the SL-interface and the external tubing. A square channel design of 130 µm result in a circular channel due to residual resist after the IPA development step.

The printing time per job of approximately 2 hours and 10 minutes depends mostly on the height of the structure, as the build plate is slowly raised out- and in the liquid resist per vertical slice. A reduction of the height of the structure directly reduces printing time, as each 25 µm slice takes approximately 24 s. Per job approximately 30 SL-substrates could be printed, from which follows that fabrication time per device is 4.33 min.

4.2 2PP- base, yurt, and cantilever

After fabrication of the SL-device 2PP-printing of the base, yurt, and cantilever can commence in the manner as described in the printing strategy. This was devised because in the DiLL-printing configuration there exists a chance of scratching the objective lens during initial approach, and if printing occurs close to high-aspect ratio structures that are larger than the working distance of the objective.

The most crucial printing step is that of the 2PP-base. If that is not fully connected to the substrate liquid will leak at this interface. Two problems were faced that can hamper with the fluidic connection, first is the formation of the gas bubbles during laser illumination of the SL-substrate. These bubbles effectively block laser irradiation by physically displacing liquid resist and scattering of the laser beam. The gas inside the bubbles will dissolve in the resist if they're smaller than approximately 3 µm, but can coalesce into larger bubbles that will persist. If the bubbles are larger than the structure wall it will remain as a hole after developing. This problem is solved by maximising the thickness of the wall and an addition of the rectangular slits in the base design. Small bubbles that form will remain in these slits and are prevented from coalescing. The printed base structure is shown in figure 9

The second problem were the irregularities in surface height of the SL-substrate. Larger bubbles form when laser illumination starts deeper in the substrate, for the reason that more substrate material gets ablated. It was therefore desired to start printing at a depth of 1 to 2 µm close to the substrate surface without losing fluidic function. figure 17 shows the surface roughness and height irregularities of the SL-substrate. These height differences can lead to unconnected structure walls, as seen in figure 18. It can also be seen that small circular ablation spots due to the laser illumination are present (figure 18), and these can be used as indicators of a connected structure. The height problem was solved by aborting the print when the structure is not fully connected, and restarting the print one or several micrometers deeper until the ablation spots are visibly uniformly present.

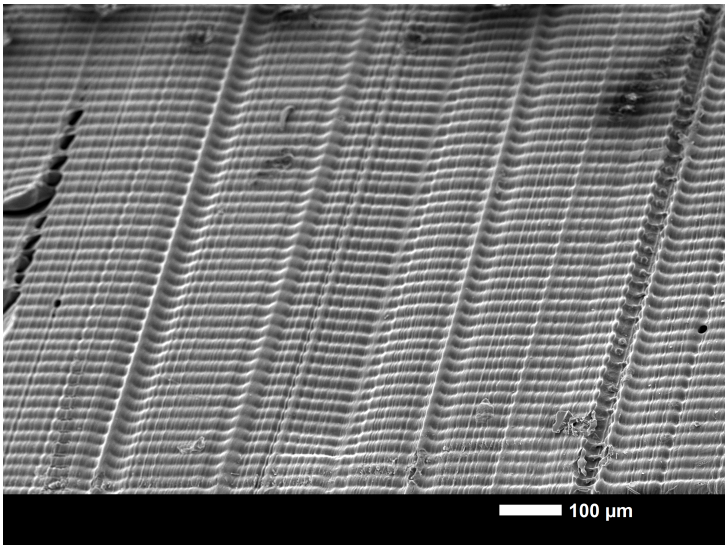


Figure 17: SEM-picture of the surface of a SL-substrate, showing the roughness and height irregularities due to printing defects.

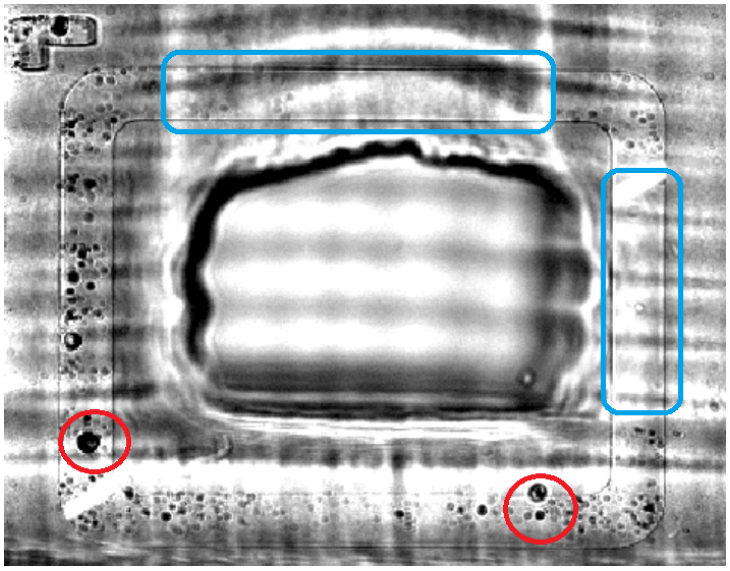


Figure 18: Microscope feed picture of the top view of a rectangular 2PP-structure printed around an SL-aperture. Through the transparent material the surface defects due to ablation are visible as small black spots, two of those are indicated with red circles. The blue rectangles indicate the locations where these spots were not visible, thus these parts were not connected to the substrate.

On top of this base the yurt was printed whose main function is connecting the cantilever and the base. These 2PP-structures are printed layer-by-layer, with the layers parallel to the SL-surface. Printing time was kept at a minimum by designing and printing the yurt to have a low height, while still retaining a spherical shape to avoid stress concentrations.

A horizontal cantilever was printed around an aperture at the side of these yurt-structures,. However, high aspect ratio structures cannot be printed horizontally with the layer-by-layer method, as the very first printed layer will be a single voxel thick and thus very compliant. This layer can tear, displace, or outright detach due to brownian motion in the liquid resin, and subsequent layers will be affected by this first layer. This problem was solved by printing the cantilever in vertical, overlapping slices. However, vertical printing is hindered by an effect called shading. This occurs when structures are printed close together and one structure casts a shadow which will reduces the amount of laser illumination in the shaded areas, effectively blocking parts of the other structures being printed. This is resolved by printing the slices under an angle, and three slice thicknesses were printed as a test, 5 µm, 3 µm and 1 µm, as shown in figure 19.

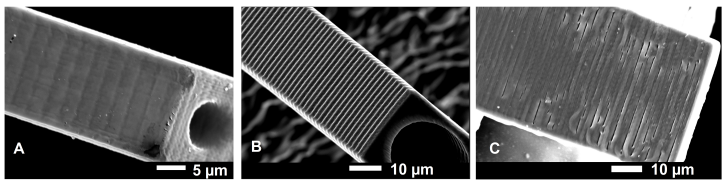


Figure 19: **A)** SEM picture of a cantilever surface with 5 µm imported slices with a 2 µm overlap. **B)** A cantilever with 3 µm imported slices with a 1 µm overlap. **C)** SEM picture of a cantilever printed with a self written code, where the designed distance between the single voxel 1 µm thick slices was 0.3 µm. The resulting overlap was insufficient for a full connection between slices, leading to the visible slits between them.

These slicing sizes will lead to different structural properties of the cantilever, as this slicing determines how much of the cantilever will be doubly exposed, thereby changing the materials Young's modulus slightly [21]. Overlap between slices should also be sufficient, as that would ensure that slices stay connected during and after illumination, which causes the photopolymer to shrink slightly. The SEM-picture in figure 19 **C** shows this clearly, where slices of a single voxel (approximately 1 µm wide) were written with a designed distance between the slices of 0.3 µm. The resulting overlap was not sufficient, causing slits of tens of nanometers to form between the slices, effectively adding numerous parallel high hydraulic resistance channels.
The other effect of slicing is the difference in surface roughness. For non-contact measurements such as laser Doppler vibrometry (LDV), a smooth surface is desired for sufficient reflection of the laser. An increase in surface roughness would scatter a higher proportion of the incoming laser light, and this scattering can be reduced by increasing thickness of the slices. These have reduced surface roughness compared to thinner slices, as seen in figure 19.
The internal channel is affected by the slicing as well, as scallops form inside which have sizes comparable to the slice thickness. The scallops that were formed for the 5 µm slices resulted in a closed channel and it was found that slices of 3 µm with a 1 µm overlap would result in a surface roughness that still yielded sufficient signal strength for LDV measurements, while retaining full fluidic functionality.

The printing process of base, yurt and cantilever can be automated and performed in a single, maskless step, which reduces the active time spent on fabrication. This is in contrast with standard clean room micro fabrication, where multiple active steps and masks are needed. Total printing time for the combined 2PP-structure is approximately 2.5 hours, with a developing time of 48 hours, for sufficient removal of the resin from the channel. If it is assumed that

standard microfabrication yields one hundred cantilevers in two weeks, (ten working days, 240 hours) then the fabrication per cantilever will be 2.4 hours. Additional steps such as glueing will still be required to be able to use these chips, which is not the case for the 3D-printed ones, as those can be directly connected to external tubing after developing.
The printing method developed here is not optimised, and other implementable strategies to decrease the printing time has been developed by others [15]. Also non-horizontal cantilevers could be printed that do not involve vertical slicing, decreasing the printing time.

Another benefit of 3D-printing is that after every job a design could be altered with little to no extra cost, and it could be printed immediately, compared to the clean room microfabrication, where a new mask has to be designed and all fabrication steps have to be performed again, making prototyping costly and slow.

4.3 Adhesion

Adhesion strength between the SL-device and 2PP-base puts additional limits on the cantilever design dimensions, as this determines how much pressure can be set on the device before the base detaches. This maximum adhesion strength is determined from the nano indentation graph in figure 12. In this graph the vertical jumps indicate sudden displacements of the nano indenter tip, which can only occur if the 2PP-blocks detach. When a cube is loaded it can either detach fully, or tear, since the force is applied in the middle of the cube and not at its base. Optical inspection showed that cubes were detached in full, with no tearing observed. The lowest detachment forces were recorded for the $200\,\mu m^3$ blocks, and although no standard deviation can be determined, this data can be used as a limit for adhesion strength. It follows that these blocks can withstand a maximum sheer stress of 1.5 MPa, and this is indicative of the maximum pressure the device can handle before detachment of the 2PP-base. The fact that such bonding occurs between the acrylic-based photopolymers of the SL-device and 2PP-structures can possibly be explained by diffusion of some liquid 2PP resist inside the solid SL-substrate. Subsequent laser illumination will then be able to polymerise the internal 2PP resist, thereby creating some interlocking between the two materials.

This maximum allowable pressure can be viewed as an additional design criterium for cantilever channel dimensions. For a hollow cantilever dispensing requires that the capillary pressure must be overcome. For a cylindrical aperture this is described as: $P_{cap} = \frac{2\gamma\cos\theta}{r}$, where γ is the surface tension of the liquid, θ the wetting angle of the liquid at the channel wall, and R the effective radius of the sphere that can be superimposed on the meniscus. This pressure is largest when this radius coincides with that of the channel, or in other words, if the wetting angle is π, which occurs just before a droplet is dispensed at the cantilever tip. The Hagen-Poiseuille law can be modified to include the capillary pressure, and is shown in equation 1.

$$Q = \frac{\pi r^4 \left(\Delta P + \frac{2\gamma\cos\theta}{r}\right)}{8\mu L} \tag{1}$$

If the maximum applied pressure is taken to be 1.5 MPa, a maximum wetting angle of π, and with the surface tension between water and air as $72.86\,mN\,m^{-1}$, a graph can be plotted for different values of the flow rate Q, as seen in appendix **B**, which can serve as a design guide for minimum cantilever aperture diameters and lengths.

The functional cantilevers that were printed were 350 µm long and had internal channel diameters of 25 µm. After substituting these dimensions into equation 1 it was found that these diameters could be reduced further to approximately 3.5 µm for a flow rate of $5\,\mu L\,min^{-1}$. The choice for this large channel diameter was taken to speed up the development process in which residual resist is removed, as this becomes more difficult with narrower channels.

4.4 Fluidic experiments

Fluidic functionality is shown in figure 14 where the filling of a cantilever is shown. The resistance through the cantilever that the fluid experiences was modelled as in figure 6. It was found that the highest resistance resulted from the cantilever channel, $4.56 \times 10^{13}\,Pa\,s\,m^{-3}$, due to the 25 µm channel diameter and 436 µm internal length. The second highest is for the tubing, which is mostly due to its length of 48 cm. The calculations for these resistances assume a smooth surface inside the SL-interface and cantilever, which is not the case due the internal scalloping. However, because the internal flow is laminar this will only increase the resistance slightly.
When flow rate experiments are performed care should be taken to wait for steady flow to form, and this time is determined by the capacitive elements in the circuit. The interpretation of this capacitance is that when a pressure is applied to an internal channel it slightly expands, thereby increasing its volume and affecting the flow. The amount of expansion depends on the initial volume and Young's modulus of the material, and in this hydraulic circuit the highest capacitive influence was from the flexible tubing. It's relatively high channel volume and low Young's modulus make it expand noticeably when pressure is applied. The tubing contributes almost solely to the time constant, with its product of the resistance and capacitance being 0.0319 s, and with the contribution of the next highest capacitance from the syringe being only 3.3985×10^{-9} s.

The performed flow rate experiment resulted in the graph shown in figure 15, in which nanoliter flow rates were measured with large standard deviations for the highest measured flow rate. The expected flow rates were a factor of three higher, $10\,\mu L\,min^{-1}$. Inspection of the yurt base revealed that another fluidic channel was formed from which some liquid was leaking, effectively being a parallel fluidic resistance.

4.5 Mechanical characterisation

The eigenfrequency is obtained through the experiment, and from that the stiffness and Young's modulus can be derived. The experimental values correspond well with the analytical- and finite element model, as seen in tables 4 and 5 and a possible explanation for the discrepancies between them is that the Young's modulus depends on the degree of crosslinking between monomers, which, in acrylate-based photoresists, depends on the writing speed and laser power [22].
The elastic modulus of 4.6 GPa is comparable to that of SU-8 (4.5 GPa), from which hollow cantilevers have already been fabricated with clean room microfabrication and their mechanical and fluidic functionality have been demonstrated [9].

Table 4: Comparison of the values of the eigenfrequency, stiffness, and the Young's modulus, obtained through an analytical and finite element model, and the experiment. *The Young's modulus of the analytical model is adopted from literature [23].

	Analytical model	**FEM**	**Experiment**
Eigenfrequency (kHz)	99	96	99.6 ± 6.2
Stiffness ($N\,m^{-1}$)	15.55	14.76	15.8 ± 1.9
E-modulus (GPa)	4.6*	4.37	4.6 ± 0.5

Table 5: Relative errors of the eigenfrequency, stiffness, and Young's modulus between the experiment, and the analytical and finite element model.

	Analytical error	**FEM error**
Eigenfrequency	5.5-6.8%	2.6-10.2%
Stiffness	10.5-14.7%	5.7-20.8%
Young's modulus	10.5-14.6%	5.8-20.7%

The quality factor was determined to be approximately 174, which is in the expected range for resonating cantilevers in air. This quality factor is approximately three times larger than one reported in literature for 2PP-written doubly clamped, suspended hollow SU-8 structure [15]. The fact that the 2PP-printed cantilever is only singly clamped has a positive effect on the quality factor, as energy dissipation through the supports only occurs on one side.
The quality factor can be significantly increased by removing additional factors that increases vibrational energy dissipation, such as modifying the viscous drag of the medium by changing the cantilever shape or removing the medium itself. This energy loss broadens the magnitude peak around the resonance frequency, and, in combination with noise, will have an adverse effect on the resolution with which changes in the eigenfrequency can be detected.

5 Conclusions

In this work a fabrication method has been developed for the direct printing of a polymer microfluidic hollow cantilevers by two-photon polymerization onto a stereolithographically 3D-printed microfluidic interface, together with a connecting base design that can mitigate fluidic disconnection by large bubble formation. The thickness of the cantilever slices determined the external- and internal surface roughness, which could affect the laser Doppler vibrometer measurements by scattering the incident laser light, and so weakening the receiving signal.
A 350 µm long cantilever with a width and height of 30 µm and internal diameter of 25 µm has been fabricated and its eigenfrequency, stiffness, and Young's modulus has been determined experimentally and compared to an analytical-, and finite element model. The values for these are 99.6 kHz, $15.8\,N\,m^{-1}$, and 4.6 GPa respectively.
The adhesion strength between the 2PP-written base and the SL-substrate was investigated and it was found that the base can withstand a maximum pressure of 1.5 MPa before delamination occurs, resulting in lower limits on possible channel diameters.
A fluidic circuit model has been constructed from which the fluidic resistances and capacitances were calculated. The total resistance was $6.09 \times 10^{13}\,Pa\,s\,m^{-3}$, with the highest resistance being the cantilever channel. The capacitive elements in the circuit determine the time it takes to reach steady state flow, and the biggest contributor to the RC time constant of 0.0319 s is the tubing due to its relatively high volume and low Young's modulus. The fluidic experiment resulted in flow rates that were three orders of magnitude smaller than expected, and the forming of a parallel fluidic path was identified as the reason.
A quality factor of approximately 174 has been obtained in air, which is three times larger than another 2PP written hollow beam structure reported in literature, and this difference is explained by the fact the structure printed in this

work was clamped only on a single side, in contrast with the doubly clamped beam from literature.

A comparison between the 2PP-printing of a microcantilever and standard clean room micro fabrication showed that the total fabrication time per device are similar, with 3D-printing only needing a single fabrication step that requires little involvement. This fabrication method is suitable for rapid prototyping, being able to print several different designs without any additional mask changes and repetition of time costly fabrication steps. The non-optimised printing time of a single device was approximately 2.5 h.

References

[1] Murali Krishna Ghatkesar, Hector Hugo Perez Garza, and Urs Staufer. Hollow AFM cantilever pipette. *Microelectronic Engineering*, 124:22–25, 2014.

[2] Orane Guillaume-Gentil, Eva Potthoff, Dario Ossola, Clemens M. Franz, Tomaso Zambelli, and Julia A. Vorholt. Force-controlled manipulation of single cells: From AFM to FluidFM. *Trends in Biotechnology*, 32(7):381–388, 2014.

[3] André Meister, Michael Gabi, Pascal Behr, Philipp Studer, János Vörös, Philippe Niedermann, Joanna Bitterli, Jérôme Polesel-Maris, Martha Liley, Harry Heinzelmann, and Tomaso Zambelli. FluidFM: Combining Atomic Force Microscopy and Nano uidics in a Universal Liquid Delivery System for Single Cell Applications and Beyond. *Nano Letters*, 9(6):2501–7, 2009.

[4] Vincent Martinez, Csaba Forró, Serge Weydert, Mathias J. Aebersold, Harald Dermutz, Orane Guillaume-Gentil, Tomaso Zambelli, Janos Voros, and László Demkó. Controlled single-cell deposition and patterning by highly flexible hollow cantilevers. *Lab Chip*, 2(2):303, 2016.

[5] Hector Hugo Perez Garza, Murali Krishna Ghatkesar, Per Lothman, Andreas Manz, and Urs Staufer. Enabling local deposition and controlled synthesis of Au-nanoparticles using a femtopipette. *9th IEEE International Conference on Nano/Micro Engineered and Molecular Systems, IEEE-NEMS 2014*, pages 323–328, 2014.

[6] Keun Ho Kim, Raymond G. Sanedrin, Andrea M. Ho, Seung W. Lee, Nicolaie Moldovan, Chad A. Mirkin, and Horacio D. Espinosa. Direct delivery and submicrometer patterning of DNA by a nanofountain probe. *Advanced Materials*, 20(2):330–334, 2008.

[7] Owen Loh, Robert Lam, Mark Chen, Nicolaie Moldovan, Houjin Huang, Dean Ho, and Horacio D. Espinosa. Nanofountain-probe-based high-resolution patterning and single-cell injection of functionalized nanodiamonds. *Small*, 5(14):1667–1674, 2009.

[8] Y T Yang, C Callegari, X L Feng, K L Ekinci, and M L Roukes. Zeptogram-Scale Nanomechanical Mass Sensing. pages 10–13, 2006.

[9] Vincent Martinez, Pascal Behr, Ute Drechsler, Jérôme Polesel-Maris, Eva Potthoff, Janos Vörös, and Tomaso Zambelli. SU-8 hollow cantilevers for AFM cell adhesion studies. *Journal of Micromechanics and Microengineering*, 26(5):055006, 2016.

[10] Ferry P.W. Melchels, Jan Feijen, and Dirk W. Grijpma. A review on stereolithography and its applications in biomedical engineering. *Biomaterials*, 31(24):6121–6130, 2010.

[11] Shoji Maruo and Koji Ikuta. Submicron stereolithography for the production of freely movable mechanisms by using single-photon polymerization. *Sensors and Actuators, A: Physical*, 100(1):70–76, 2002.

[12] Reza Amin, Stephanie Knowlton, Alexander Hart, Bekir Yenilmez, and Fariba Ghaderinezhad. 3D-printed microfluidic devices. 2016.

[13] Dengfeng Tan, Yan Li, Fengjie Qi, Hong Yang, Qihuang Gong, Xianzi Dong, Xuanming Duan, Dengfeng Tan, Yan Li, Fengjie Qi, Hong Yang, and Qihuang Gong. Reduction in feature size of two-photon polymerization using SCR500 Reduction in feature size of two-photon polymerization using SCR500. 071106(2007):1–4, 2015.

[14] M A M Gijs, R Guidetti, J Michler, E Montinaro, M Grisi, M C Letizia, L Petho, J Brugger, and G Boero. 3D printed microchannels for sub-nL NMR spectroscopy. pages 1–17, 2018.

[15] Celso Accoto, Antonio Qualtieri, Ferruccio Pisanello, Carlo Ricciardi, Candido Fabrizio Pirri, Massimo De Vittorio, and Francesco Rizzi. Two-Photon Polymerization Lithography and Laser Doppler Vibrometry of a SU-8-Based Suspended Microchannel Resonator. 24(4):1038–1042, 2015.

[16] F Perrucci, V Bertana, S L Marasso, G Scordo, S Ferrero, C F Pirri, and M Cocuzza. Microelectronic Engineering Optimization of a suspended two photon polymerized micro fluidic filtration system. *Microelectronic Engineering*, 195(February):95–100, 2018.

[17] John T Fourkas. *Chapter 1.3 - Fundamentals of Two-Photon Fabrication*. Elsevier Inc., 2016.

[18] Yang Liao, Ya Cheng, Changning Liu, Jiangxin Song, Fei He, Yinglong Shen, Danping Chen, Zhizhan Xu, Zhichao Fan, Xunbin Wei, Koji Sugioka, and Katsumi Midorikawa. Direct laser writing of sub-50 nm nanofluidic channels buried in glass for three-dimensional micro-nanofluidic integration. *Lab on a Chip*, 13(8):1626, 2013.

[19] Polytec gmbh, waldbronn, germany. *MSA-400 manual*.

[20] Kwang W Oh, Kangsun Lee, and Edward P Furlani. Lab on a Chip Design of pressure-driven microfluidic networks using electric circuit analogy. pages 515–545, 2012.

[21] Enrico Domenico Lemma, Francesco Rizzi, Tommaso Dattoma, Barbara Spagnolo, Leonardo Sileo, Antonio Qualtieri, Massimo De Vittorio, and Ferruccio Pisanello. Mechanical properties tunability of three-dimensional polymeric structures in two-photon lithography. *IEEE Transactions on Nanotechnology*, 16(1):1–1, 2016.

[22] Li Jia Jiang, Yun Shen Zhou, Wei Xiong, Yang Gao, Xi Huang, Lan Jiang, Tommaso Baldacchini, Jean-Francois Silvain, and Yong Feng Lu. Two-photon polymerization: investigation of chemical and mechanical properties of resins using Raman microspectroscopy. *Optics letters*, 39(10):3034–7, 2014.

[23] John H. Campbell, Nicole Nicole, Ori Stein, Ying Liu, Yongfeng Lu, and Lijia Jiang. Three-dimensional printing and deformation behavior of low-density target structures by two-photon polymerization. *Nanoengineering: Fabrication, Properties, Optics, and Devices XIV*, (August):66, 2017.

3

Outlook

3.1. Thesis conclusion

A literature review was performed that focussed on the fabrication of (polymeric) hollow AFM cantilevers. Some of their applications are discussed briefly, including force spectroscopy, mass measurement, and liquid dispensing. It has been found that mostly standard micro/nanofabrication techniques are employed for the fabrication of these hollow structures. A photopolymerization technique called two-photon polymerization has been able to 3D-print polymer structures with resolutions lower than 1 µm.
In this thesis a suspended hollow microcantilever was 3D-printed by 2PP. The 2PP-cantilever was directly printed onto a stereolithographically printed microfluidic device, that serves as a ready-to-use connection to the external world.

One main research question was posed, which could be subdivided in two: "How can a polymeric hollow cantilever be fabricated with 3D-printing, which can manipulate sub-picoliter volume fluids with a one-step connection to the external world?"

1. *How can a two-photon polymerized printed part be integrated with a stereolithographically printed part?*
   Direct printing of the 2PP-structure onto a stereographically printed substrate resulted in sufficient bonding between the two acrylic-based photopolymers. A 2PP-base design had been printed around the aperture of the SL-microfluidic interface that made use of the full writing field of the 25x objective. The second irradiation of the SL-interface by the femtosecond laser of the 2PP-printer can lead to local ablation and bubble forming. Small (<3 µm)bubbles will dissipate, but bubbles larger than that tend to persist. Slots in the base will trap small bubbles, thereby preventing them to coalesce into a bigger bubble. Laser writing settings have been optimized and it was found that printing of the material IP-S on HTM140M is succesfull with a laser power of 20 mW and scanning speed of 60 mm s^{-1}.
   A printing strategy has been developed, where the microfluidic substrate is taped to the bottom of a glass slide and liquid resist is deposited on it. The dip-in-laser-lithography printing mode is employed in which the objective is directly in contact with the liquid resin, and the structure is printed on the bottom of the slide. The laser is first focussed on the glass surface, and then the objective is lowered such that the distance between the SL-substrate and objective lens is larger than the working distance of the objective. Small test structures are printed at incremental heights and the correct printing height is reached when a test structure is printed on the substrate. Hollow cantilevers have been printed with a width and height of 30 µm, and a length of 350 µm and an inner diameter of 25 µm.

2. *What are the values of the physical characteristics of such hollow structures?*
   The cantilever has been mechanically characterized with laser Doppler vibrometry. An 18 nm gold/palladium layer was sputtered on it to increase reflection. A fundamental frequency of ~94 kHz was obtained, and through it a stiffness of 14.13 N m^{-1} and Young's modulus of 4.18 GPa, which is in agreement with an analytical- and finite element model. A quality factor in air of ~174 was obtained.
   A fluidical circuit model was constructed and the total resistance was calculated to be 6.09×10^{13} Pa s m^{-3}.
   The time constant due to the capacitive elements was determined to be 0.0319 s.
   Adhesion between 2PP-blocks and a SL-substrate was investigated with nano indentation. A maximum

pressure on the device of 1.5 MPa was deduced, and minimum channel radii as a function of cantilever length were modelled for several flow rates.

3.2. Recommendations

It was found that some devices were not watertight, and most of the time this was due to only partially connected 2PP-bases. The surface of the SL-substrate around the aperture was uneven and at times had distortions. These were the results of the environment in which the printer was operating. Dust particles on either the build plate or on the projector glass led to regular distortions of the surface of the final device. A recommendation would be to egalize the surface by precise cutting, or alter the SL-design in such a way that the flat surface would be parallel to the printing plane. Other materials with better defined surfaces could be used, such as glass, but additional steps such as glueing would become necessary again.
There are significant time improvements to be made, firstly for printing the SL-substrate. The printing time per device was determined by the height of the structure, so if the design could be altered to print it horizontally, it would not only result in a flat surface, but also in faster printing times. A printing job with a structure height of 3.69 mm took 135 min, and the printing time is linearly dependent on the structure height.
The printing time of the dome and cantilever could also be reduced. A time-reducing printing strategy could be explored where only several outer contours of the structure are irradiated by the laser, leaving the internal resin trapped and unpolymerized. A subsequent full UV-irradiation step would polymerize the internal resin. This method was utilized by Accoto et al. [74] and helpful suggestions are made there.
Printing horizontal cantilevers takes more time then printing an angled cantilever, as each slice is printed from bottom to top, whereas an angled cantilever can be printed fully.

3.3. Future work

As this work shows, the design freedom offered by 3D-printed can be further explored in future work. For example, the stiffness and mass of the cantilever can be specifically tuned by changing the cantilever shape and dimensions.

Mass can be distributed unevenly over the cantilever to amplify and modify desired mode shapes.

The quality factor could be increased by designing the cantilever surface such that fluid can be more easily displaced by it, i.e. shaping it in such a way that it reduces the viscous drag.

Multiple internal channels of different dimensions could be printed in parallel, thereby enabling multiple kinds of fluids to be dispensed/measured at flow rates in set ratios of the channel resistances, i.e. multiple flow rates with a lower number of pressure sources.

A sharp tip could be printed on the cantilever in such a way that atomic force microscopy would be possible in combination with pipetting, without losing visibility of the probe tip.

Very low stiffness (<0.01 $\mathrm{N\,m^{-1}}$) cantilevers could be printed for non-invasive, non-destructive cellular studies [58].
The transparent cantilever could possibly be used together with an optical tweezer to trap particles at the tip for mass measurements.
Active elements can be printed inside the cantilever, or inside the microfluidic substrate. For example a peristaltic pump could be printed, or a microfluidic diode [96].

Different materials could be added to the resins to change its properties, for example the addition of ferrofluidic particles to form a photosensitive ferrofluid to print micro/nanomachines that can be actuated magnetically [85]. Regular resin can be used to print the skeleton or device, then it could be developed regularly. A second printing step could be performed afterwards with the altered resin to add functionality to the earlier printed device.
In the same manner an electrically conducting resin could be used to actuate the cantilever directly, or add capacitive sensing of the deflection, or trapping of particles at specific locations inside the cantilever.

A

Fabrication

These appendices describe with more depth what is discussed in the paper. Fabrication and experimental processes will be discussed, what problems were encountered and how they were overcome or turned into an advantage. These appendices are divided into two parts, fabrication and characterization details.
In this section the fabrication process of a 3D-printed hollow microcantilever is discussed, beginning with the stereolithograpically 3D-printed microfluidic interface. Then testing has been performed to find optimal parameters for the use of two-photon polymerization. After that the method of connecting the interface with the 2PP-printed yurt is expanded upon. The section finishes with a functional device and a focus on the printed cantilevers.

A.1. Microfluidic interface

By definition, microcantilevers have at least one dimension smaller than 1 mm, with outer diameters typically in the tens of micrometers, inner diameters in single micrometers, and lengths in the hundreds. The device needs to interact with the external world; it needs connections to an external pressure source if fluid dispensing is desired. These dimensions make assembly by hand impractical, which poses the first problem, and one of the research questions is derived from it: how can two photon polymerization be integrated with stereolithography to construct functional fluidic structures?
In literature, cantilevers that are fabricated by standard microfabrication processes are designed with handling in mind. The cantilever and fluid reservoir are fabricated in a single chip, where chip dimensions are several millimeters, which can still be handled with tweezers. However, with this fabrication method a connection from the microfluidic chip to an external pressure source requires a glueing step, where either the chip is directly glued to the tubing, or glued to an interface that connects to the tubing. This extra step introduces the danger of clogging the internal channels by improper glueing and thus rendering the cantilever useless.

One solution to this problem is to 2PP 3D-print the entire device as a single structure, just as with standard micro/nano fabrication, with the benefit of not having to glue the device. However this amplifies one major drawback of 2PP 3D-printing: the time it takes to print a structure. A single block of 200 μm^3 can take half an hour, and that is without needing to stitch parts together. Stitching is needed if structures are printed that exceed the writing field of the galvo-mirrors that are used for laser positioning. Bigger structures are then separated in sections and printed sequentially, and printing a millimeter sized structure can take hours to days for a single device.

Another solution is 3D-printing a microfluidic interfacing device with stereolithography. This device must function as an interface between tubing and the cantilever, it should also be big enough that it can be handled with a tweezer, and have an internal channel that can be connected to external tubing. The smallest feature size that can be printed with this method is 25 µm as reported by the manufacturer, which is a loss in resolution compared with two-photon polymerization, for which the manufacturer claims sub-micrometer resolution. The benefit of stereolithography over 2PP-printing is that it reduces the printing time per device, as multiple devices can be fabricated in one print job. A single print job takes approximately two hours and

ten minutes, where the height of the device is the time-bottleneck. In this work the approach of fabricating an interfacing device has been implemented.

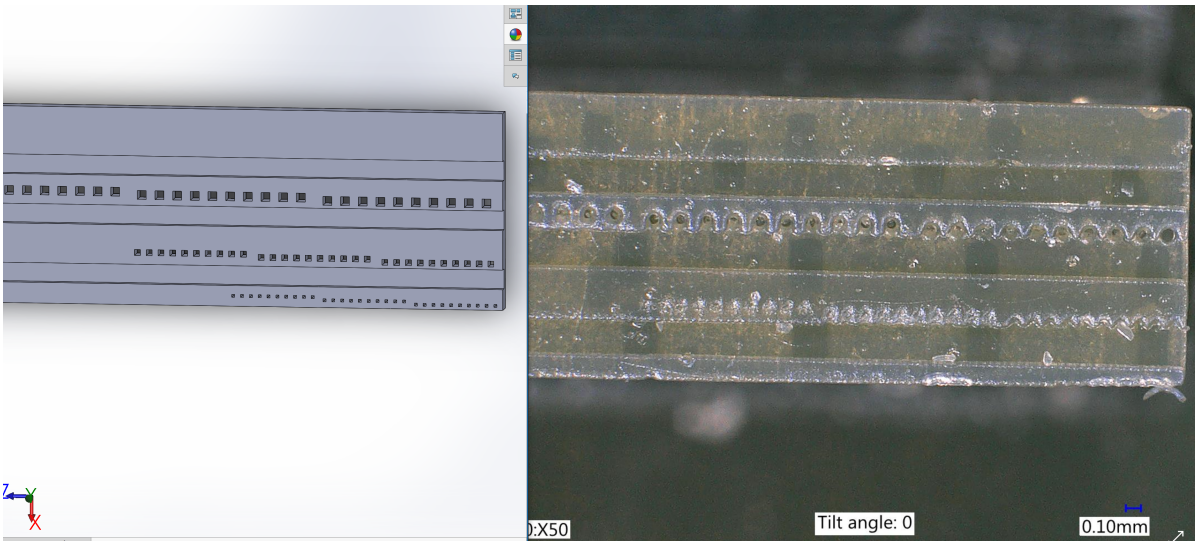


Figure A.1: Comparison between the CAD-design and a picture of the stereolithographically printed structure. Thirty holes each with sizes of 30, 60, and 90 μm^2, which have been placed 30, 60, and 90 µm from an edge.

The first test that was performed was on finding the minimum aperture size that could be reproducibly fabricated with the available stereolithography 3D-printer (EnvisionTec Micro-Plus HD). Figure A.1 shows a comparison between the CAD-design and printed structure, where apertures have been printed that are 30, 60, and 90 μm^2. They have been positioned at a distance of 30, 60, and 90 µm from an edge. The reason for this additional positioning test was to find out at what distance an aperture could be printed without changing the same aperture. From figure A.1 several things can be concluded.

1. square hole design lead to circular holes
2. apertures with dimensions smaller than 90 µm will not be printed
3. the minimum distance from an edge is 90 µm

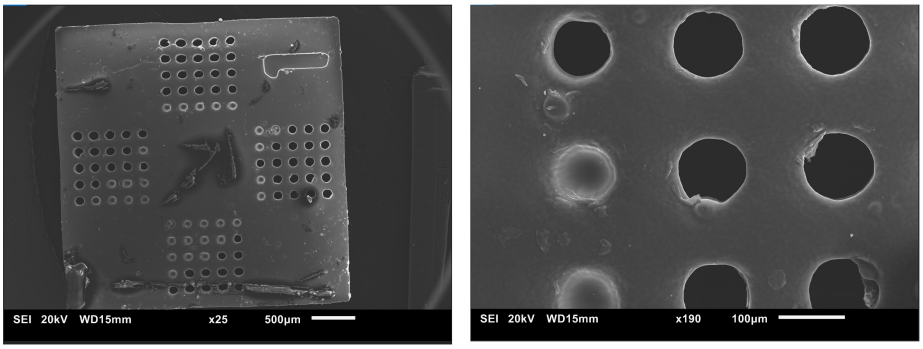


Figure A.2: SEM images of SL-printed structures with 100 µm apertures. Some apertures were not developed for a sufficient amount of time, leading to clogged apertures.

From the picture it can be seen that the reproducibility of open holes is not high, with hole diameters inconsistently below 90 µm. A second print was performed with an aperture size of 100 µm as shown in figure A.2. Although the size of the aperture is now consistently 100 µm, it can be seen that several apertures are not fully developed. An explanation of this is that during a developing step, where residual resin is removed by

2-propanol, was not performed for a sufficiently long time. Larger apertures proved to be reliably printed and 130 µm sized apertures were set as internal channel dimension.

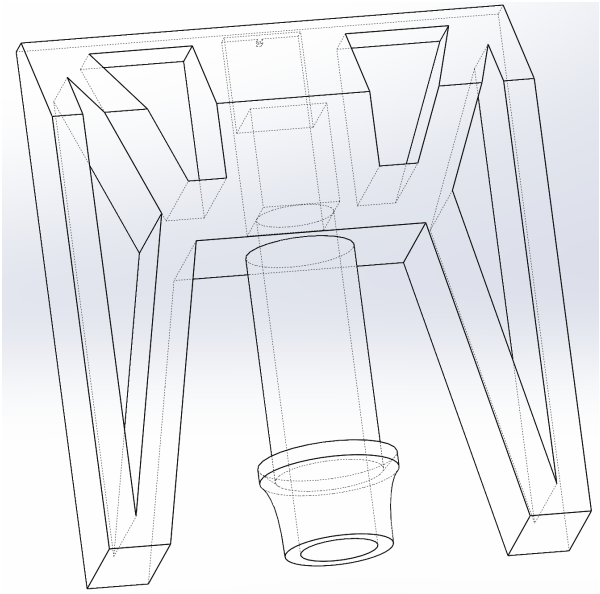


Figure A.3: CAD-design of an initial fluidic interface. The tubing can connect to the structure, and an internal channel runs through it, ending in an aperture on the top of the device at the back. This device, and subsequent versions were 3.6 mm in length, and 3.15 mm in width. These dimensions were chosen such that the device could still be handled by tweezer.

Based on these channel dimensions an initial interface design was made, shown in figure A.3. This structure was printed with the inner channel parallel with the print build plate. However, these dimensions were determined for a printing orientation of the channel that was perpendicular to the build plate. This resulted in channels and apertures that were deformed and the device was unsuitable for a connection to tubing. The reason for this was that the resolution of printing apertures is different in all three directions, x, y, and z, although according to the manufacturer the resolution of x and y should be the same, 30 µm. The decision was made to print the device with the internal channel perpendicular to the print build-plate, resulting in reproducible internal channels as seen in picture A.4.

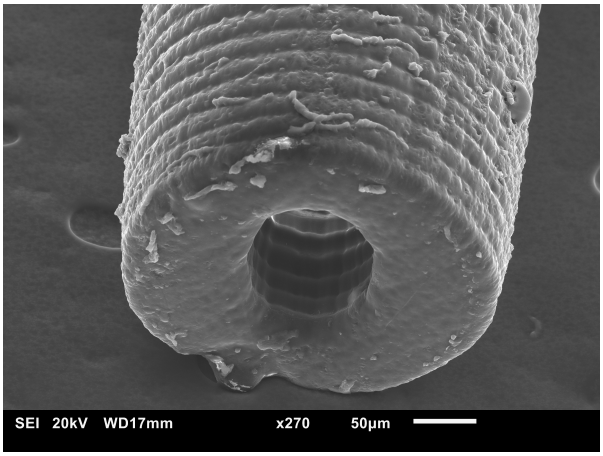


Figure A.4: SEM picture of the connection between external tubing and the fluidic interface. The device is printed perpendicular to the build plate, resulting in the open channel. In the picture individual printing layers are visible as scallops on the exterior.

This perpendicular printing orientation meant that the minimum reproducible dimensions for the small aperture, where eventually the cantilever would be printed, needed to be determined. Several simple squares

with equally spaced apertures were printed, with dimensions of increasing size, until the apertures were consistently open. The structure in figure A.5) **A** shows such a square test structure for which the designed apertures resulted in consistent apertures. These minimum dimensions were approximately 150 µm.
The distance between the apertures were designed to be 200 µm, but turned out to be approximately 105 µm. This is attributed to the earlier mentioned resolution difference in all three writing directions.

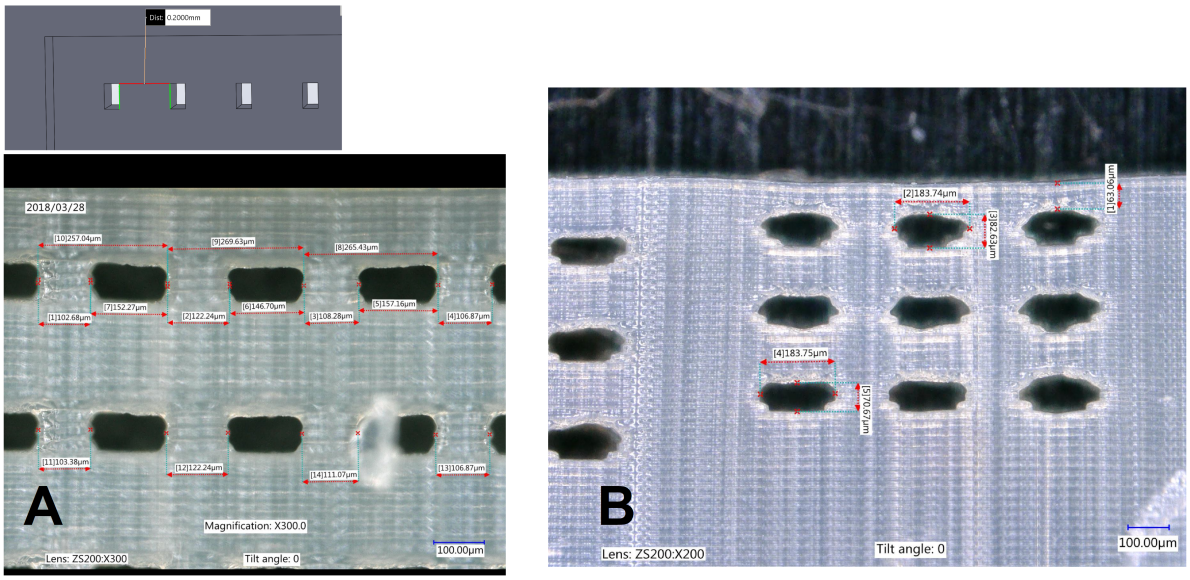


Figure A.5: **A)** comparison of the spacing of the apertures between the CAD-design and the printed part. **B)** diamond-shaped apertures.

60 µm designed diamond-shaped apertures have been printed to investigate if that would result in smaller apertures, which was not the case. The apertures retained their diamond shape only slightly and the dimensions were bigger than in figure A.5) **A**. All of the described tests resulted in the design choice for the aperture dimensions to be 100 µm long and 60 µm wide.

Since the goal is to 2PP-print onto this fluidic interface, it should be able to fit into the 2PP-printer without interfering with its function. The height was chosen to be 400 µm, as this would be able to house a 130 µm internal channel, be sturdy enough to be handled, and thin enough such that it fits into the 2PP-printer. The final version of the fluidic interface design can be seen in picture A.7, alongside a picture of a printed device.

An important aspect of the SL-printing is the scaffolding that supports the device during the printing process and subsequent cleaning steps. Extra ridges have been added to the approximately 4 mm high scaffold, as shown in figure A.6.

short summary
A microfluidic device was 3D-printed with stereolithography with its main function being the connection between a 2PP-printed cantilever and the external world. The printing resolution was found to be different for in-plane and out-of-plane printing. Minimum aperture and channel size for reliable out-of-plane (z-direction) printing of apertures was 130 µm and for in-plane ~150 x ~90 µm. The final device has dimensions ~3.1 x ~3.7 x ~0.4 mm.

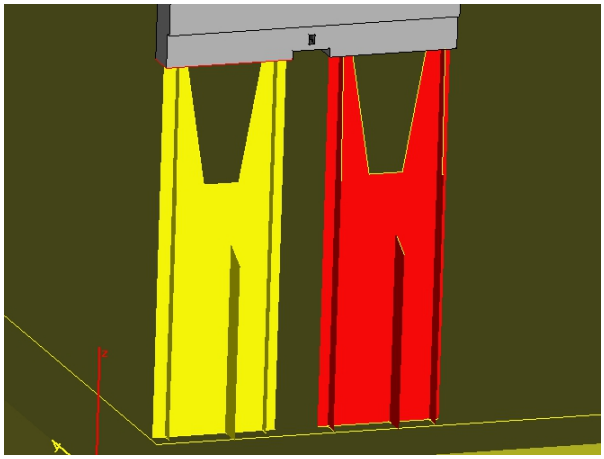


Figure A.6: Scaffolding design for printing of the SL-printed interface. This scaffold keeps the device stable during removal of excess photo resist in the ultrasonic bath.

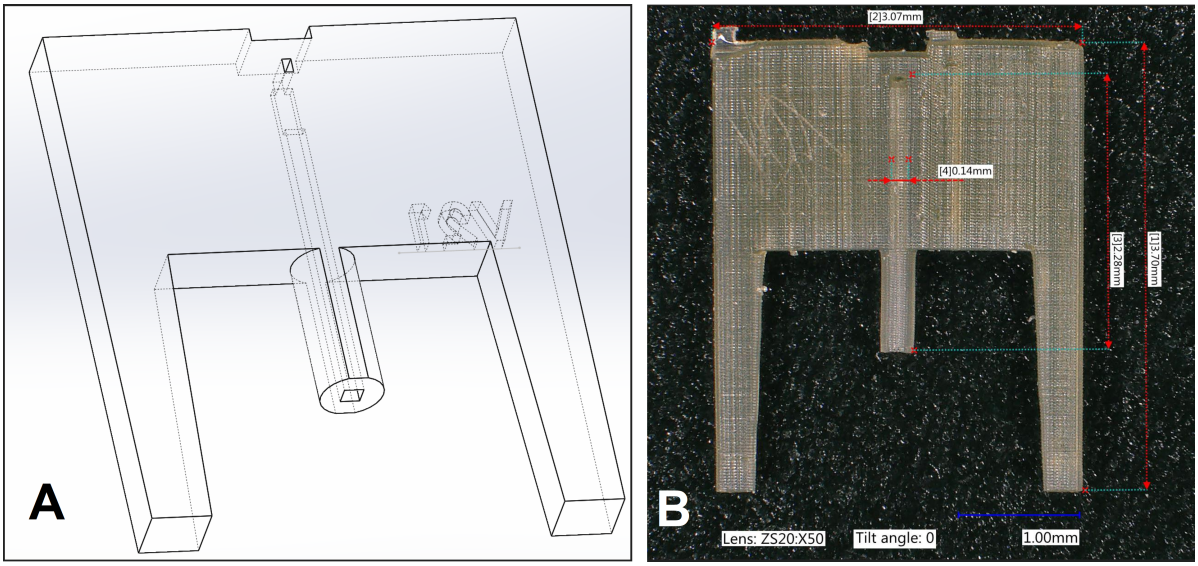


Figure A.7: CAD-design **A** and picture **B** of the final version of the fluidic interface.

A.2. Two-photon polymerization testing

A Nanoscribe photonic professional GT was used for two-photon polymerization. The machine uses galvo mirrors to direct the focus of a pulsed femto second fiber laser beam with pulse lengths between 100 fs - 200 fs. The position of the focus can be changed by the galvo mirrors and a motorised stage in x and y, by a piezo-resistive element for fine positioning in x, y, and z, and the z-position of the microscope itself. Two-photon polymerization allows for freeform 3D-printing, however, the shadowing effects must be taken into account. Earlier written structures effectively block the laser from polymerizing structures in their shadow. A layer-by-layer printing method will by-pass this type of shadowing. In the 2PP-printer high-speed 2D galvo mirrors were used for in-plane writing, and a piezoresisitive element for out-of-plane.

There are several parameters than can be tuned, which can be divided into design parameters and writing parameters. The design parameters are set when the designer loads an .stl-file into the Nanoscribe-specific software called DeScribe, where the stl-file is converted into a format that describes what path the voxel will take to write the structure. The design parameters are listed and described in table A.1. A data file will be created after the .stl-importation, and this can be used as input for the print job.

A code must be written in Describe-syntax for the actual print job. Printing parameters can be set here, as well as importing the data files containing the CAD-designed structures. For-loops can be used to change parameters during printing, or importing multiple copies of the same data file for repeated printing. The code

Table A.1: Design parameters for a CAD-imported design.

Parameter	Explanation
Slicing distance	The structure will be printed from top to bottom. The voxel lines are written layer-by-layer, whereby the distance between layers is the slicing distance.
Hatching distance	This is the distance between voxel lines that are in the writing plane.
Hatching angle	This value sets the angle between hatching lines of two slices.
Contour count	The edges of structures are written as single, separate lines. Contour count sets the number of these lines.
Contour distance	The distance between two contour voxel lines.
Splitting	If the structure is bigger than the writing field of the objective it must be split into separate blocks. The size of these blocks as well as the angle between them can be set.

that was used for printing of a cantilever can be found in the supplementary.
Laser power and scan speed are two important parameters. The former can be set as a percentage of the maximum laser output, which is 50 mW. The laser power is adjusted by an acousto-optic modulator. Scan speed is the speed at which the voxel travels, which is set in $\mu m\,s^{-1}$. This speed has a noticeable effect on the surface roughness, especially at sharp corners. Higher scan speeds decrease writing time, but some printing accuracy is lost. The parameter settings also depend on the printing configuration, the chosen objective, photopolymerizable resin, and type of substrate.

There were three microscope objective types available, magnifications of 20x, 25x, and 63x. Naturally with higher magnifications comes higher resolution, and 63x magnification was chosen. The type of objective puts limits on the writing field of the galvo, and for 20x the writing field diameter is 600 µm, for 25x 400 µm, and for 63x 200 µm. The aperture size of the fluidic interface was around 150 µm long, and 110 µm wide, which is within the writing field of the 63x. The 63x was initially chosen for this reason and its sub-micrometer resolution.
The machine can operate in two configurations, the oil/immersion (conventional) mode, or dip-in-laser lithography (DiLL) mode. For the conventional mode the resist is deposited on top of the glass slide, with oil between the glass and the lens. The structures are written on the top side of the glass. In the DiLL mode the objective lens is directly immersed in the resist and structures are written on the bottom of the slide. Figure A.8 shows a schematic of both modes.

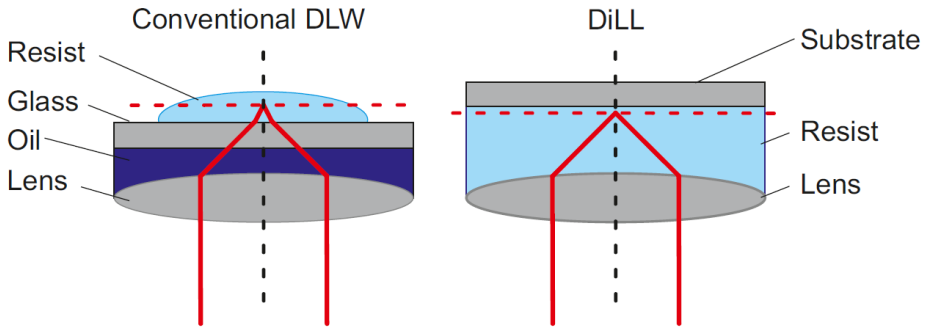


Figure A.8: Conventional oil/immersion printing mode and the dip-in-laser lithography mode. Figure adopted from the Nanoscribe user manual.

The two parameters laser power and scanning speed were tested in the conventional mode. $16\,\mu m^2$ hollow cubes with a wall thickness of 3 µm were printed in an array. Laser power and scan speed were varied, as shown in figure A.9.
In figure A.9 it can be seen that laser power affects the degree of polymerization, with good reproduction of the design from laser power at 32% onward. The influence of scanning speed can be seen in figure A.10. A slower speed will result in smoother structures and no edge defects. From these tests the laser power was set at 32% and the scanning speed at $60\,000\,\mu m\,s^{-1}$. The scanning speed is chosen this high because for large (150 µm+) structures this will decrease the printing time significantly, with a small loss in structure quality.

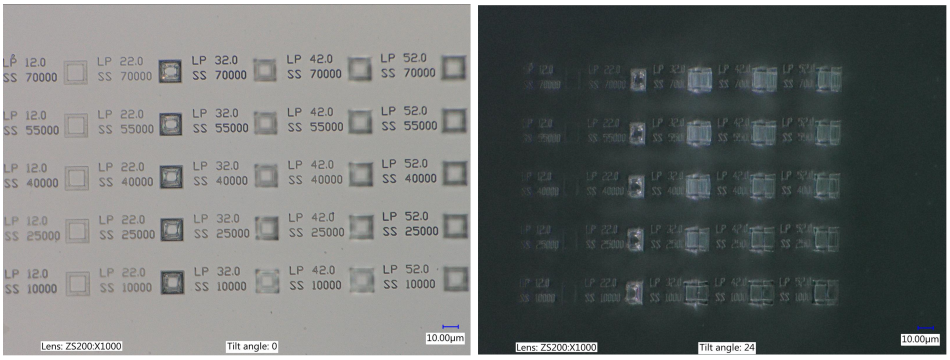


Figure A.9: Conventional mode printed 16 µm^2 hollow cubes. Laser power was varied from 12% to 52% in the x-direction and scan speed from 10 000 µm s^{-1} to 70 000 µm s^{-1} in the y-direction. The left picture is a top view and the right a 3D-composite picture under an angle.

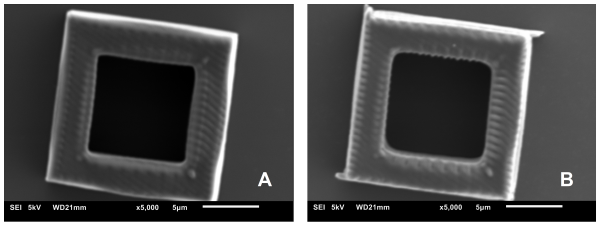


Figure A.10: SEM image of hollow squares with laser power at 52% and scanning speed 10 000 µm s^{-1} in **A**, and 70 000 µm s^{-1} in **B**.

These quality losses are less pronounced in the internal part of the cube.

short summary
The parameters for 2PP-printing in the conventional mode with the 63x objective were chosen to be 32% for the laser power, and a scanning speed of 60 000 µm s^{-1} for sufficient structure polymerization and reduced printing time.

A.3. Connection of the SL-printed part with a 2PP-printed yurt

The previous tests were structures written directly on glass. The next step is to write structures onto a stereolithographically 3D-printed substrate. The goal was to 2PP-print in the conventional mode, on an SL-printed substrate. A schematic of how it would look like is seen in figure A.11, with a picture of an SL-substrate in figure A.12.

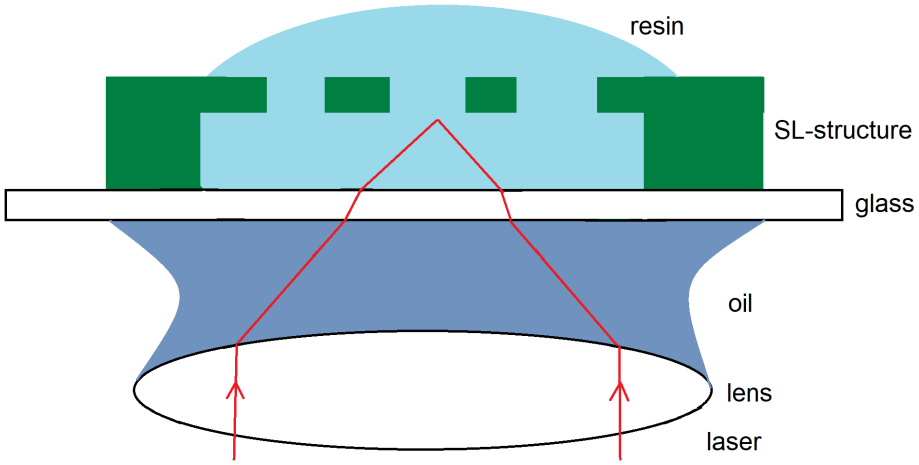


Figure A.11: Cross-section of the printing configuration on a SL-printed substrate in the conventional mode.

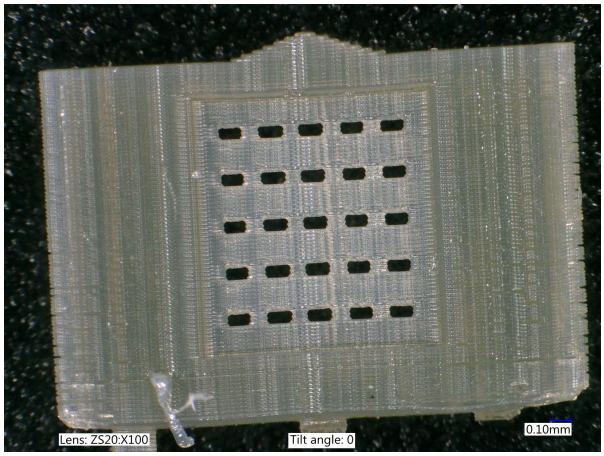


Figure A.12: Bottom view of a SL-printed substrate for 2PP-printing in the conventional mode. This and other pictures are made with the Keyence® Digital Microscope VHX-6000.

A thin-walled rectangular structure was to be printed onto the SL-substrate around the apertures. The printing process could begin after the standard sample preparation steps of cleaning the glass and SL-substrate. The process is shown in figure A.13. Firstly, the aperture is located with the microscope. A button in the Nanowrite GUI then focusses the laser at the interface between the resin and glass structure. Then a reference structure is printed to confirm the printing location of the entire structure. The structure is printed in layers until it is finished, and A.13) **5** shows a finished print after it being developed. Several things are noticeable in the last picture. The structure is not fully containing the aperture, which is a result of the limited writing field of the 63x objective that was used. The walls also have a non-desirable shape, in pictures A.13) **4** & **5** it is seen that this is due to bad connection to the SL-substrate. A single printed layer will not stay in position if it is not connected to either another layer or the substrate.

To ensure the covering of the hole, the structure has to be printed in parts. These parts are printed such that they overlap by ~2 µm. A thicker rectangle was printed next in parts, as seen in picture A.14. Taking a closer

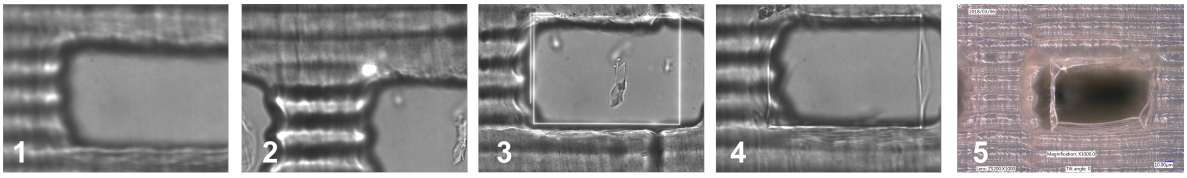


Figure A.13: Microscope images from during the printing process of a thin-walled rectangular structure. **1)** locating of an aperture with the microscope. **2)** printing of a small reference structure. **3)** printing of the rectangular structure. **4)** Finished structure. **5)** Picture of the structure after developing.

look from the sides however, reveals a stitching problem. In picture A.15) **A** it can be seen that at the places where the separate parts are stitched together, the bottom part is not connected. This problem persisted when the walls were also stitched horizontally at half the height of the rectangle A.15) **B**.

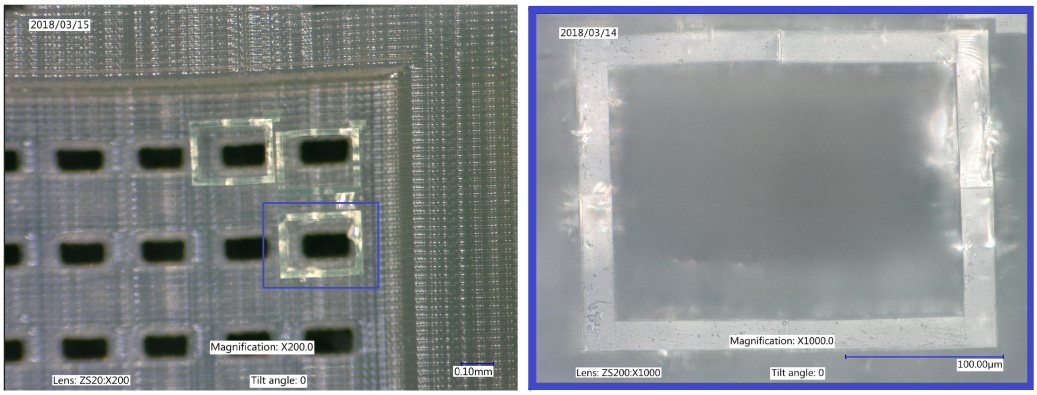


Figure A.14: A bottom view of an SL-substrate with a stitched rectangle printed on it.

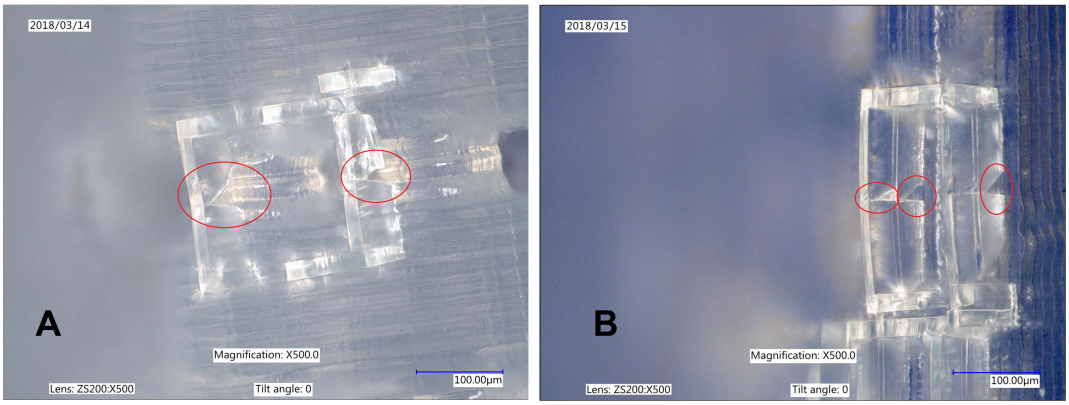


Figure A.15: Side view of the stitched rectangle. Triangular holes can be seen where the parts are stitched together.

The cause of this is a shadowing effect. The SL-substrate is always under some small angle with the glass, and precise 90° angles between the laser beam and glass substrate are also unrealistic. The very first written part won't be affected by shadowing, but adjacent parts will. The laser will not be focussed enough when it shines through the first structure, and the resin of the adjacent part will not be polymerized close to the first part. A solution to this problem is redefining the printing angle. The parts can be printed under an angle, and that must be chosen sufficiently large that the shadowing effect won't occur, as seen in picture A.16.
The height of the designed rectangle was 80 µm, and the height of the structure was measured to be ~70 µm, meaning that ~10 µm of the structure is written inside the SL-substrate.

Successful printing of a 2PP-structure onto a SL-printing structure has been shown so far. The structures

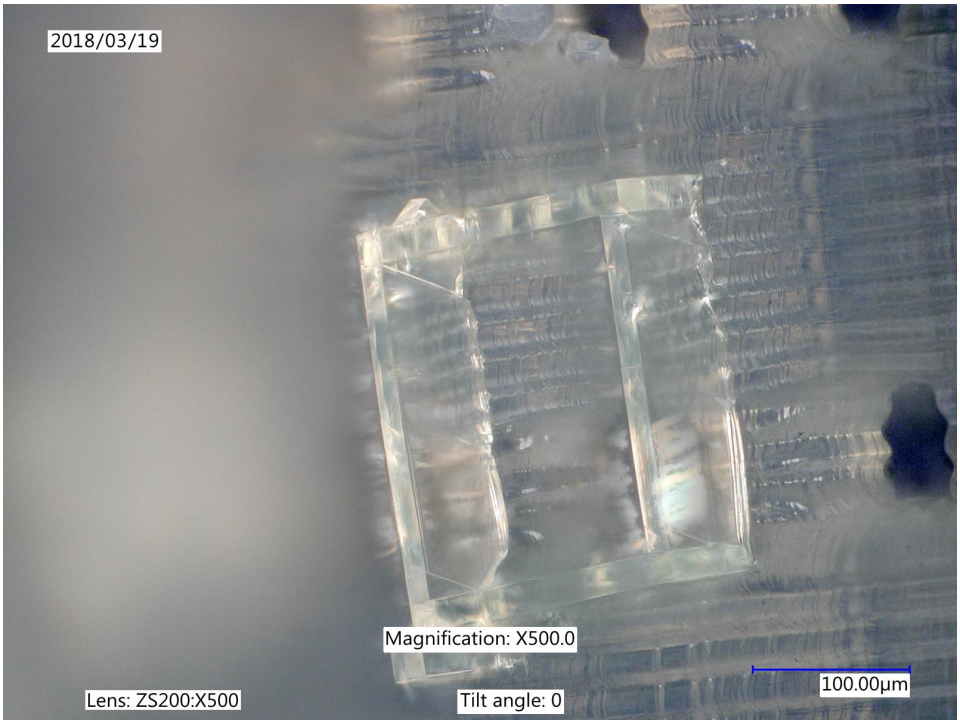


Figure A.16: Side view of the angled stitched rectangle. The triangular-shaped holes due to shadowing are not present. A stitching angle of 2° was sufficient for a 90 µm high structure.

were attached firmly enough to withstand the developing steps, and with this result the first milestone of this project has been reached.

Although printing was successful, there were practical limitations when using the conventional printing method. The first is a limitation on how high a structure can be printed. This is due to the fact that in order to print in height, the objective has to move closer to the slide. The working distance of the 63x objective is 360 µm, subtract from this a slide thickness of 170 µm and that leaves 190 µm for printing. This can be enough for an in-plane printed cantilever structure, but not for out-of-plane, as the connecting yurt between cantilever and SL-substrate can be as high as 150 µm.
The second limitation is time. As discussed earlier any structure bigger than 200 µm in diameter must be printed in several parts by stitching. The printing time increases with every part that has to be printed separately, and this could increase the time from ~half an hour to ~4 hours.
The choice was made to change the objective to the one with a magnification of 25 times which enables a writing field of 400 µm in diameter. The printing configuration was changed to the DiLL-mode, in which the structure will be printed on the bottom of the slide, thereby avoiding the height limitation of the conventional mode. Instead of a 170 µm glass slide an indium tin oxide (ITO) coated 700 µm thick glass slide is used, in combination with another acrylate based resin (IP-S - Nanoscribe GmbH). The refractive indices of the two resins IP-L-780 and IP-S are both 1.48, and they differ in viscosity. DiLL-mode requires a hanging droplet, therefore a resin with high viscosity is needed.

The same hollow square test as in picture A.9 was performed, which resulted in the choices for laser power (32%) and scan speed (60 000 µm s^{-1}). The printing configuration is shown in figure A.17, where the SL-substrate is taped to the bottom of the ITO-slide. The height of the tape needed to be determined, and the Keyence microscope enabled height measurements on the 3D-composite picture in figure A.18.
With these settings a relatively large (200 µm width and length, 100 µm high) block was printed to test the printing time with the 25x objective for large structures and printing took 18 minutes.

Because the SL-printed substrate is made from another acrylate-based photo polymer (HTM140M - EnvisionTec), it will be affected by the illumination of the femtosecond laser. The polymer will locally ablate [97] and a bubble forms. These bubbles can interfere with printing as they displace the liquid resin or block the

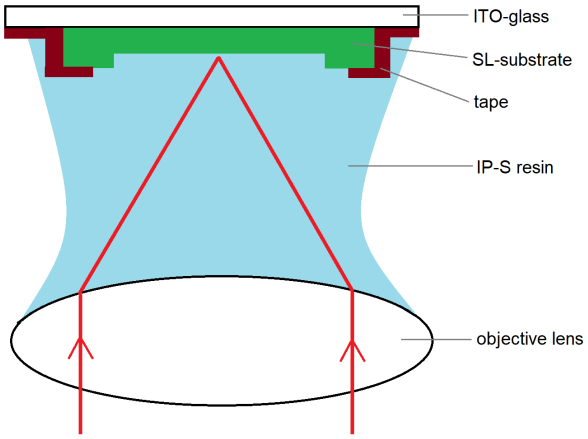


Figure A.17: DiLL configuration. The SL-substrate is taped to the bottom of the slide, then immersed in the resin. Dimensions in this figure are not to scale.

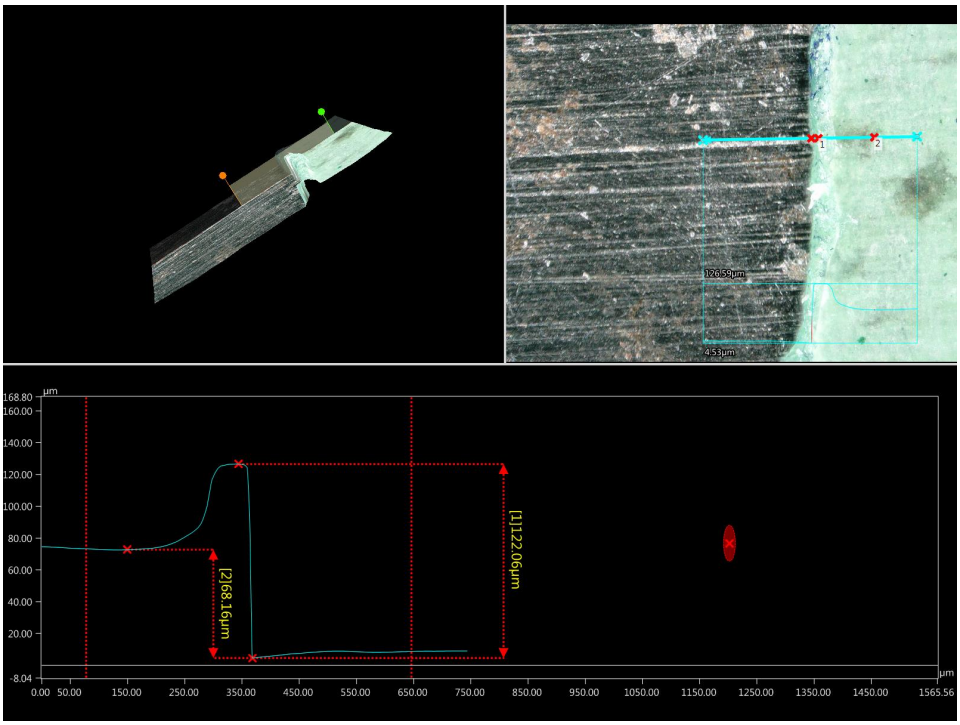


Figure A.18: 3D composite picture made with the Keyence microscope of the tape to measure its thickness. It can be seen that the tape protrudes at the edge, and to add safety to the printing procedure the tape height is taken to be 150 µm.

laser focus from reaching a location. A test was performed to evaluate the bubble formation. 10x10x40µm rectangles were printed in a five by five grid, where on the horizontal axis the laser power was varied from 12% to 52%, and on the vertical axis the scan speed from 30 000 µm s^{-1} to 70 000 µm s^{-1}. The result of this test is seen in picture A.19. Ablation occurred in some degree at all laser powers above 12%, but if the bubbles remain approximately smaller than ~3 µm they dissipate rather quickly. The size of the bubbles is seen to be increasing with laser power, most notably at 42% and 52%. As the depth of printing inside the structure increases so too does the amount of ablated material, and that directly increases the bubble size.

In DiLL-mode there exists the risk of scratching the objective lens if there's an additional structure taped to the bottom of the slide. The working distance of the objective is 380 µm, which means that the substrate should not have any parts that protrude any higher than that. The tape thickness should be taken into account when calculating the distance from objective to SL-substrate.

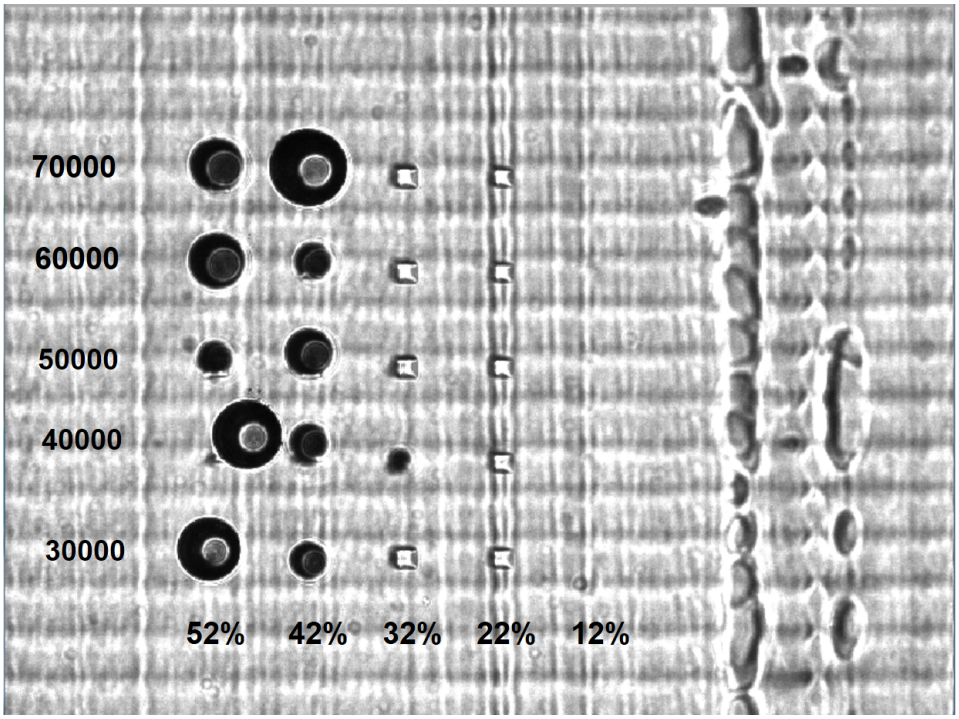


Figure A.19: Power evaluation for bubble formation. The laser power is increased from 12% to 52% from right to left, and the scan speed is increased from 30000 µm s^{-1} to 70000 µm s^{-1} from bottom to top.

The printing procedure is as follows:

1. Prepare the sample by cleaning the glass slide with acetone and isopropanol (IPA), clean the SL-substrate with (IPA), tape the substrate on the glass at a location 5+ millimeters from the center of the slide, and deposit a droplet of resin.

2. Initialize the machine, insert the holder with the sample, and approach the center of the slide.

3. Note down the microscope z-position and subtract the height of the SL-substrate and the ~150 µm tape height (A.18).

4. Lower the microscope z-position manually to this new height, then move the microscope to a suitable location on the substrate.

5. Print rectangular 10x10x40µm structures first with 20 µm height increments until the surface is reached, then finer (1 µm) increments, as shown in figure A.20) **A**. The correct height can be determined by how the rectangles look after printing, and a correct height will look like picture A.20) **B**.

6. Adjust the starting z-position in the printing code for the final structure to the correct height, then printing can commence.

Ablation will leave visible surface defects and can be used as a visual confirmation of correct printing height. Although bubbles larger than 10 µm could pose a problem, smaller ones can also be used as a visual confirmation. The surface of a stereolithographically printed substrate is shown in picture A.21 **A**, where it can be seen that the surface has a non-uniform roughness horizontally. This is a problem for example, if a structure is printed on a slanted substrate it might only be partly connected, with a partially connected rectangular structure seen in picture A.21 **B**. Sanding this surface can improve the surface, but only if the angle of sanding does not deviate significantly from the surface, otherwise it will only increase the slant.

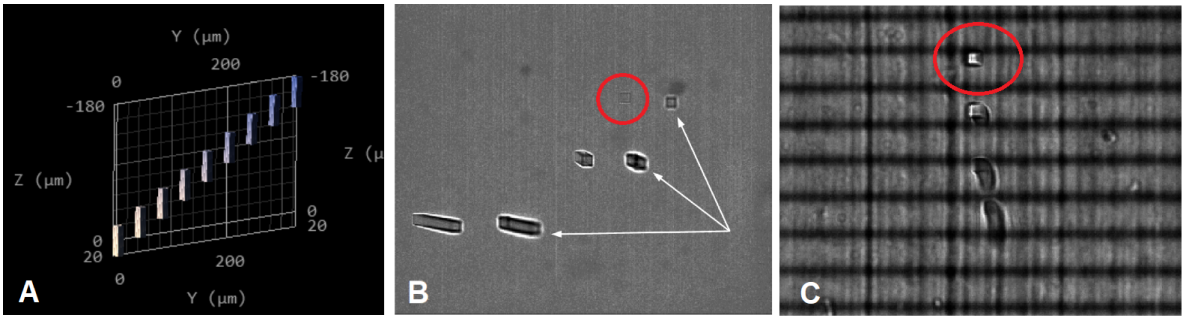


Figure A.20: **A)** Describe-software view of rectangles at incremental heights. **B)** picture of height determination on an ITO-glass substrate. White arrows indicate the shadows of the rectangles. **C)** picture of performing the height determination on an SL-substrate. The first three rectangles were not printed on the substrate and remain suspended in the resin, but the fourth was attached.

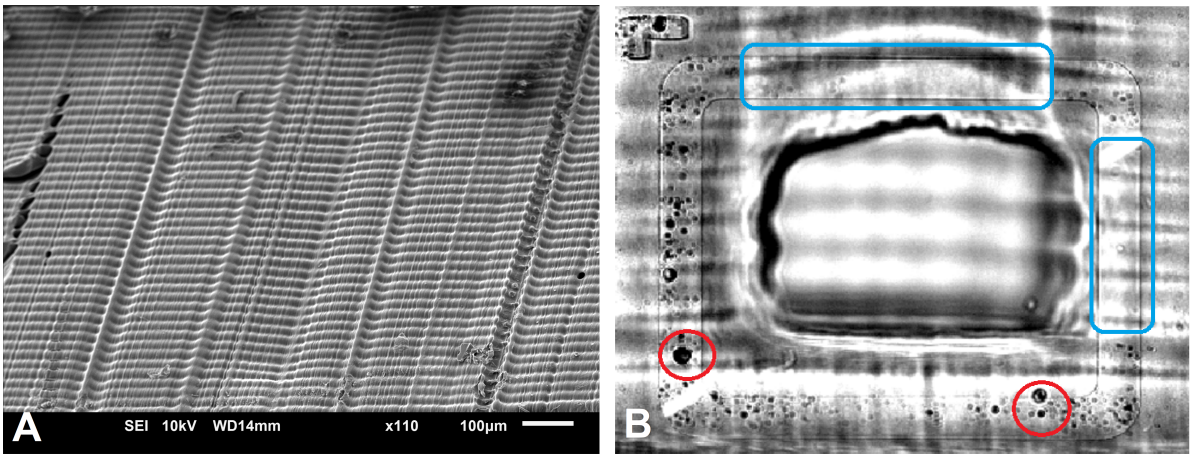


Figure A.21: **A)** SEM picture of the surface of a stereolithographically printed substrate. The horizontal lines are the ~25 µm printing lyaers and the vertical lines are due to possible contamination on the build plate or illumination window. **B** Microscope feed picture of the top view of a rectangular 2PP-structure printed around an SL-aperture. Through the transparent material the surface defects due to ablation are visible as small black spots, two of those are indicated with red circles. The blue rectangles indicate the locations where these spots were not visible, thus these parts were not connected to the substrate.

The next step would be to print closed structures, and cylinders with a sloping roof (yurts) have been attempted, as seen in picture A.22. It is clear that these are not closed, and the cause of that are the aforementioned bubbles. The bubbles had blocked polymerization at their positions and left bubble-shaped holes in the structure after development.

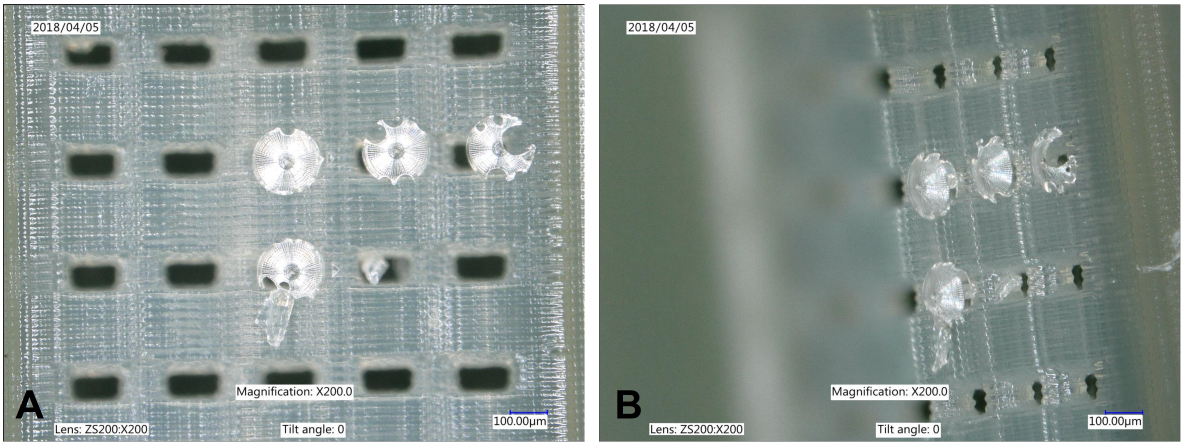


Figure A.22: Pictures of closed structures. **A)** Top view of four yurts. **B)** View under an angle of the same four structures.

To print watertight structures it is crucial that the printing depth must be deep enough so that every edge of the structure is connected to the substrate, but not so deep that excessive bubbles form. For a uniform polymer substrate a printing depth of 1 to 2 µm suffices for adequate bonding of the 2PP-structure. A maximization of the attached surface area maximizes the chance of watertight structures, because even if bubbles form, they will be encapsulated in the base of the yurt and leave no unwanted gaps in the walls. Picture A.23 shows such a base. Not only is it the same size as the writing field of the 25x objective, 400 µm in diameter, but it also contains rectangular hole structures which are able to trap bubbles when they form locally.

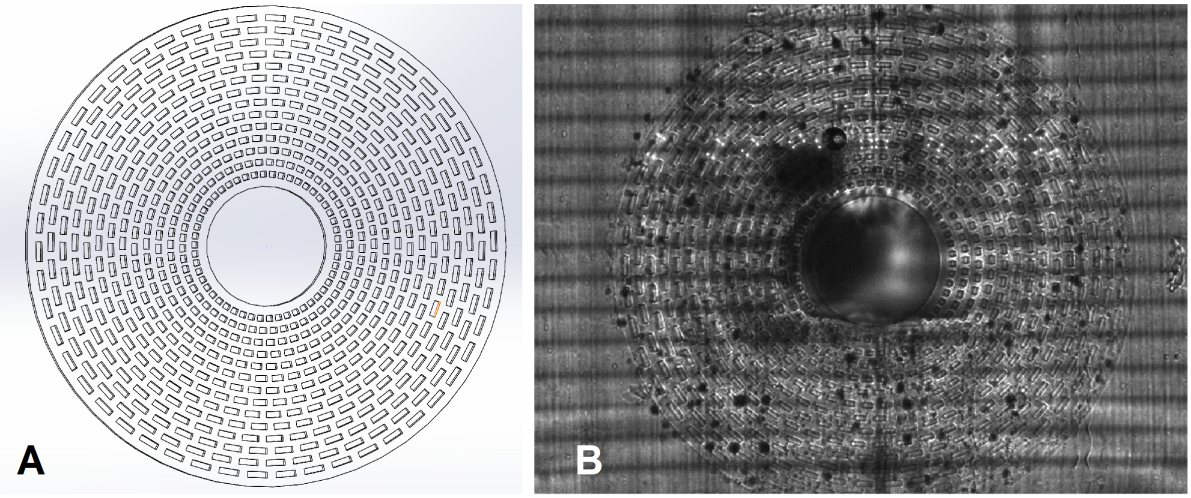


Figure A.23: Base for the yurt. **A)** shows the CAD-design and **B)** shows a printed base.

short summary

Structures were successfully 2PP-printed on an SL-substrate in both the conventional and DiLL-configuration. The choice of switching from the 63x objective to the 25x objective was motivated by the increase in writing field, enabling the printing of larger structures without time-costly stitching. The conventional configuration had a structure height limit of 190 µm, which limit out-of-plane cantilever designs. In DiLL-mode the maximum structure height is only limited by the approximately 2 mm sample holder slot. The DiLL-mode will leave a sufficient design space for out-of-plane cantilevers, considering that the yurt-structure can be as high as 150 µm. A safe substrate approaching strategy was developed, utilizing ablation defects and bubble formation as visual aids in determining correct printing heights. A 1 to 2 µm printing depth requirement was determined for adequate bonding to the SL-substrate and a base design for maximizing the attachment surface was printed.

A.4. Cantilevers

Several cantilevers were printed during the 2PP-on-SL attachment tests on separately designed fluidic interfaces on which multiple fluidically functional cantilevers could be printed A.24.

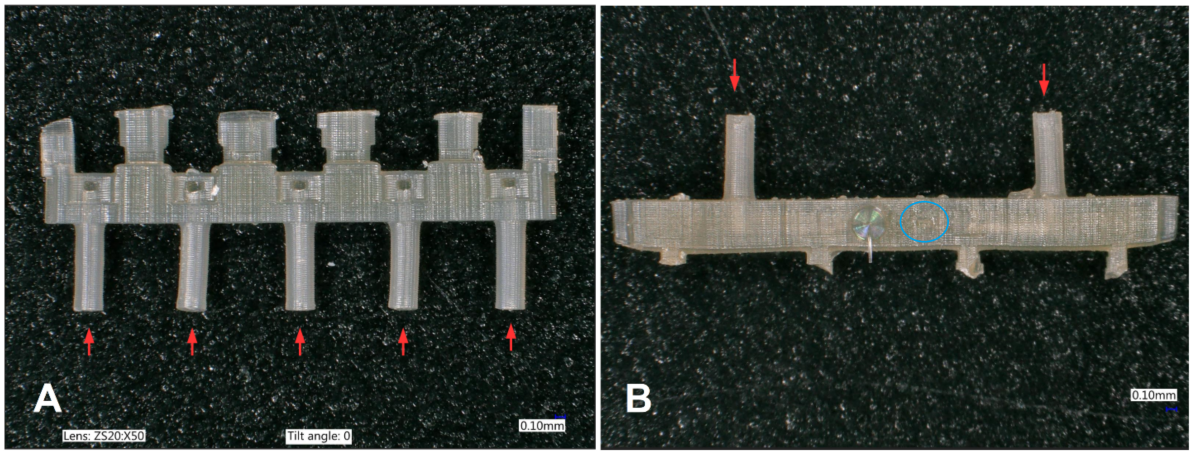


Figure A.24: **A)** Fluidic interface for printing and testing multiple cantilevers on one device. The same dimensions for the channels and aperture were taken from the single channelled fluidic interface. Red arrows indicate inlets for connection to external tubing. **B** Fluidic interface with two apertures, one of which is indicated with the blue circle, the other is covered by a printed cantilever.

The first hollow cantilever was a hollow cylinder with a 30 µm outer diameter and 10 µm inner diameter. It was printed in one session on a square yurt structure, as seen in picture A.25. The inner channel was clearly formed, but no fluids were pushed through because the base was not fully connected.

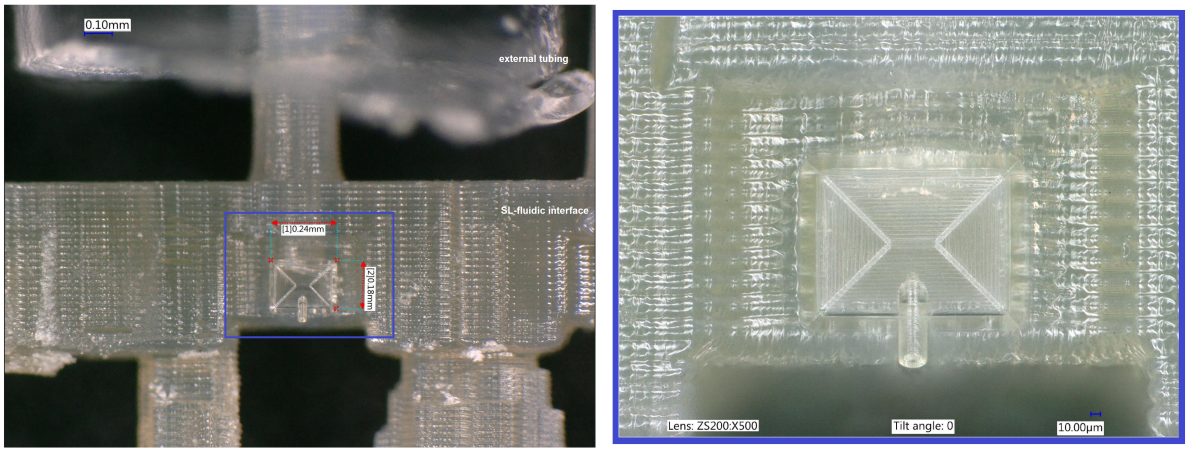


Figure A.25: Square yurt with a cylindrical diagonally upward printed hollow cantilever. At the top of the image the tubing for fluidic testing is seen to be attached to the fluidic interface.

In-plane cantilevers were printed as a monolithic structure, shown in picture A.26. The channels were not formed and the cause of this is that the first printing layer of the horizontal cantilever is a single voxel layer thick (~1 µm), but 20 µm wide and 120 µm long. These dimensions make it compliant and the layer will not stay in place, and subsequent layers will only partly be connected, leading to partially printed structures, as in picture A.26 **B**. A closer inspection of the aperture reveals that there is no channel inside the cantilever, as seen in picture A.27.

A printing strategy was developed to print horizontal structures. A code was written that writes single voxel vertical cantilever slices, the code for it can be found in the supplementary. Several cantilevers with different dimensions have been printed and are shown in figure A.28. Another printing strategy was to make CAD-designs of individual cantilever slices, and import those directly into the code. The slice is angled to counter

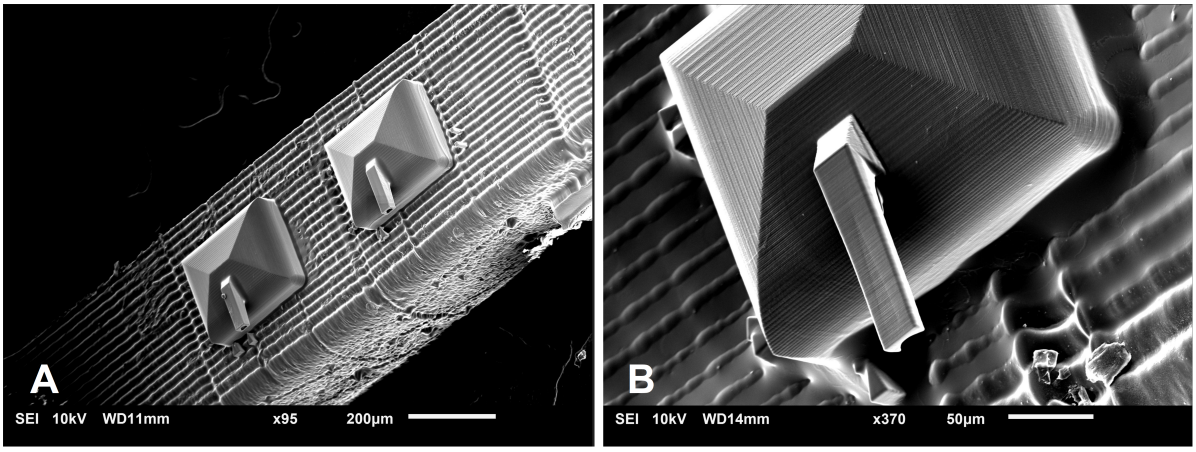


Figure A.26: SEM-images of monolithically printed horizontal cantilevers with **A)** unformed apertures, and **B)** only a partly formed cantilever.

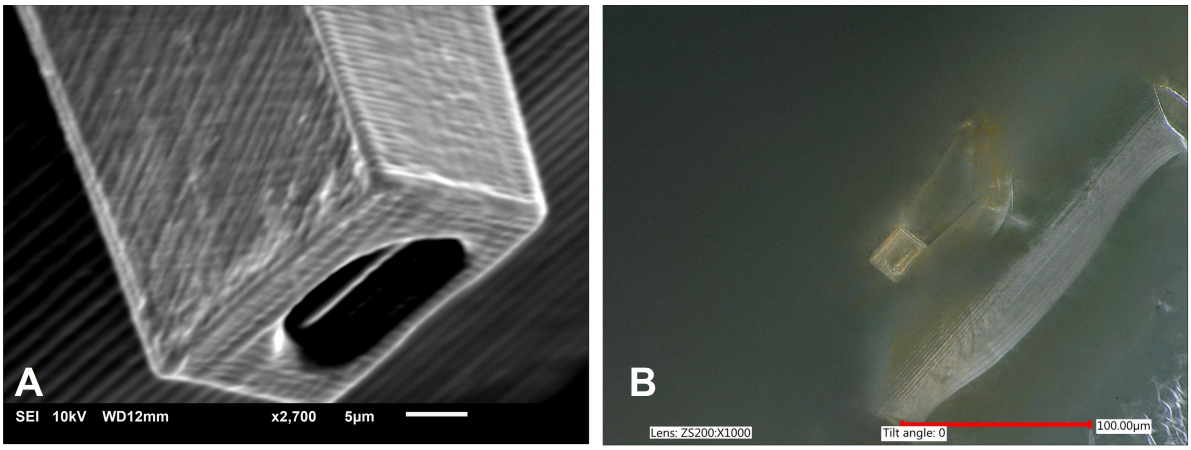


Figure A.27: **A)** SEM-image of the aperture of a cantilever. **B)** Optical image of the cantilevers front reveals that the internal channel is not formed.

the shadowing effect. The thickness of the individual slices and the amount of overlap per slice has an effect on the surface roughness, and scalloping occurs at every overlap. Figure A.29 shows a comparison between the surface roughnesses of several cantilevers with different slicing sizes and overlaps.

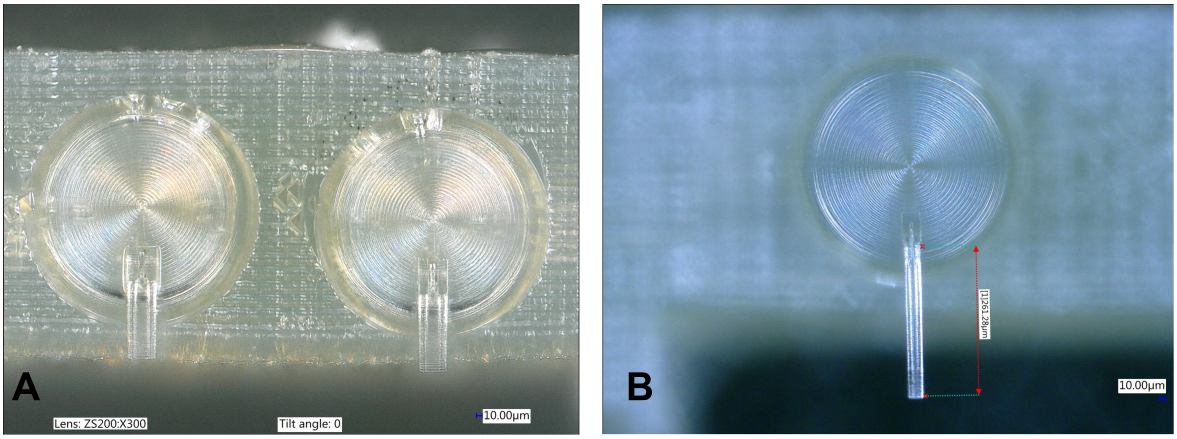


Figure A.28: Picture of self written cantilevers with dimensions for **A)**: cantilever width of 30 µm, channel diameter of 20 µm, and length of 130 µm. Dimensions for **B)**: cantilever width of 20 µm, channel width of 15 µm, and a length of 250 µm.

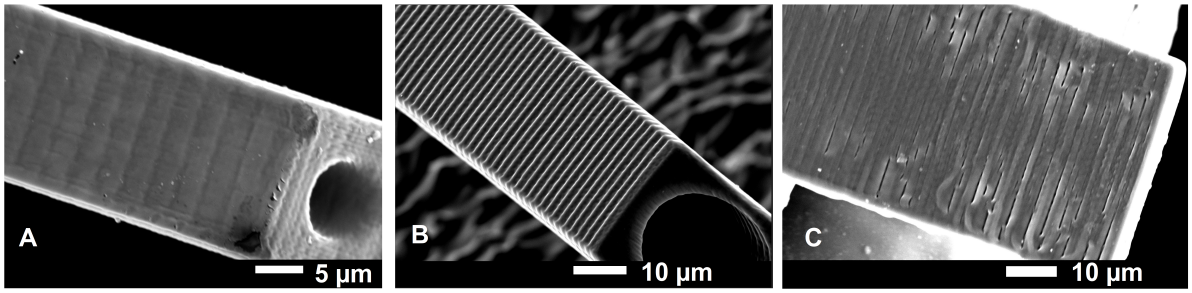


Figure A.29: **A)** SEM picture of a cantilever surface with 5 µm imported slices with a 2 µm overlap. **B)** A cantilever with 3 µm imported slices with a 1 µm overlap. **C)** SEM picture of a cantilever printed with a self written code, where the distance between the slices was 0.3 µm.

The difference between the cantilevers with self-written and imported slices is the uniformity of the scalloping. There are no irregular slots between slices for the imported slices, as is the case for the self-written ones in A.29 **C**. An overlap of 0.3 µm was not enough to keep the slices together, and the slots develop either during printing, where the voxel size is assumed to be spherical with a 1 µm diameter. In reality the voxel size depends on the laser intensity and is ellipsoidal in shape, and its width can be half as much as its height. The shrinking of the voxel lines just after the polymerization could also explain this de-bonding between layers. Smaller slicing distances could reduce this layer de-bonding. This de-bonding doesn't occur when the slices are imported as seen in figures A.29 **A** and **B**.

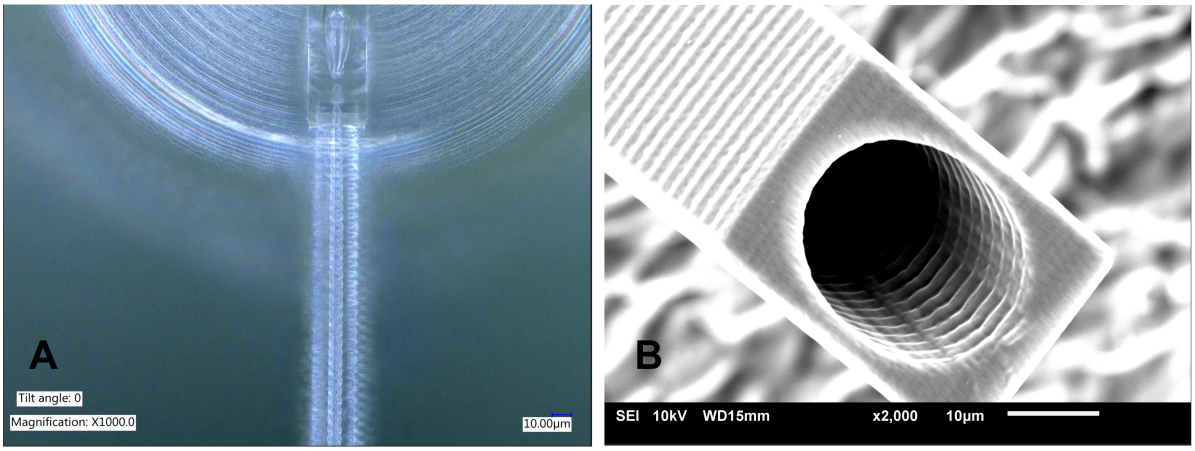


Figure A.30: **A)** Picture of a transparent cantilever with 5 µm slices where the internal scalloping of the channel surface is clearly visible. **B)** SEM picture of the internal channel near the tip of a cantilever with 1 µm slices.

Formation of a fully connected internal channel depends on the time the cantilever remains in the developing agent, Propylene glycol mono-methyl ether acetate (PGMEA). This agent removes left-over monomers, and it is critical that all the un-polymerized resin is removed from the entire channel. The channel dimensions influence the development time, and longer, narrower channels will need longer developing time than short, broad ones. A minimum developing time of 24 hours is recommended for a channel diameter of 25 µm and 300 µm length.

Although the glass slide is cleaned with both acetone and isopropanol, it is imperative that acetone is not used when cleaning the fluidic interfaces before 2PP-printing. Acetone is a known solvent for polymers and, since the fluidic interface is fabricated out of an acrylate-based photopolymer, it will dissolve given enough time. Several minutes is still detrimental, as the acetone can make the channel walls slightly porous, which can release polymer particles that can clog the cantilever channel.

A fully functional device is shown in figure A.31 **A**, together with the CAD-model in **B**, and SEM pictures of the 2PP-printed structure and cantilever in **C** & **D**. The cantilever is printed with slices of 3 µm, an overlap

of 1 µm, a width and height of 30 µm, internal channel diameter of 25 µm, and a length of 350 µm. A separate holder of multiple fluidic interfaces have been designed and 3D-printed on a fused deposition modelling (FDM) printer (Ultimaker®). A picture are found in the supplementary A.32.

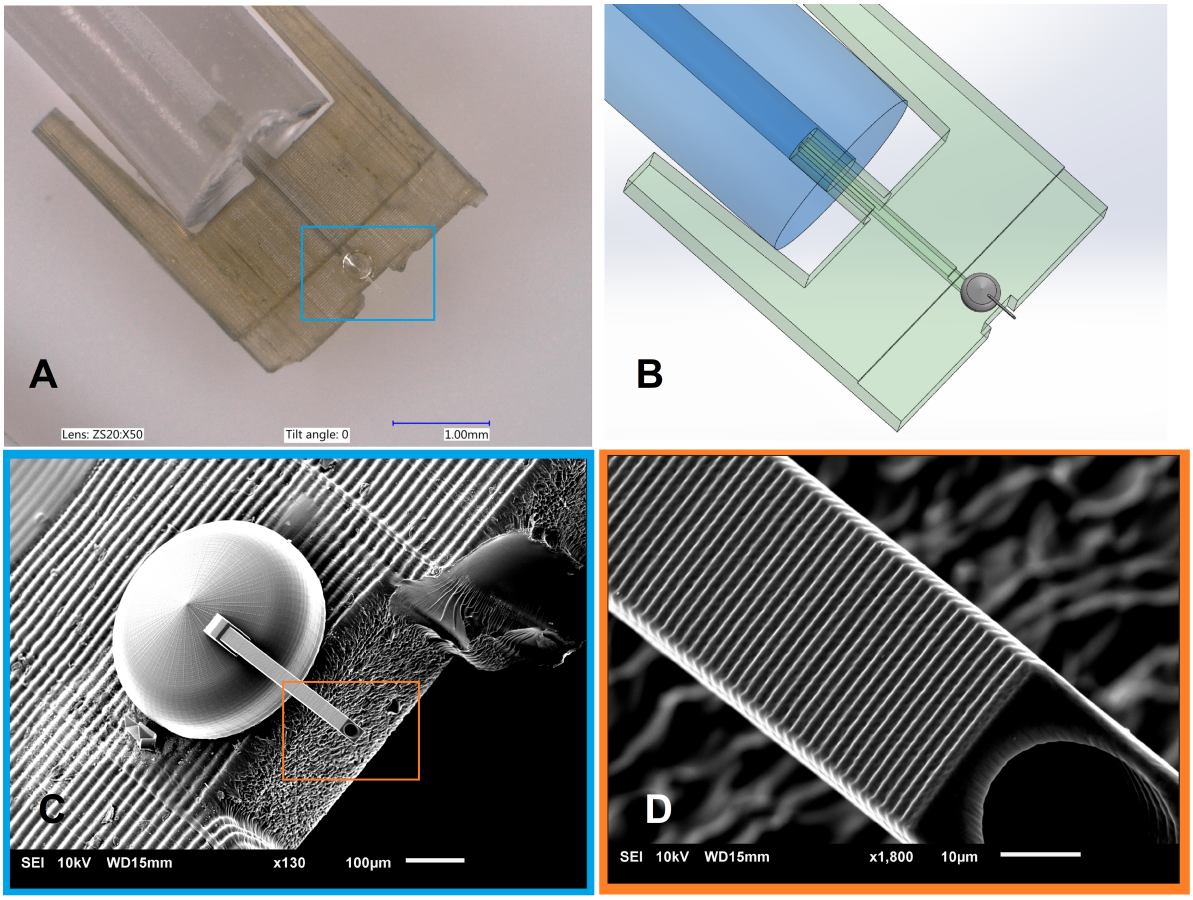


Figure A.31: A full device. **A)** Picture of a cantilever printed onto a fluidic interface that is connected to an external pressure source. **B)** CAD-design of the final device. **C)** SEM-image of the 2PP-printed microfluidic structure onto the SL-substrate. **D)** SEM-image near the tip of the cantilever.

A holder has also been designed and fabricated by fused deposition modelling 3D-printing to hold ten complete devices, shown in figure A.32. Between the two halves of the holder the cantilever is safe from physical disturbance that could damage and break it.

short summary
The first printed cantilevers were square based, non-horizontal 100 µm long, which were not functional. Horizontal cantilevers were printed by a self-written code that resulted in non-uniform, single-voxel thick cantilever slices. Uniform cantilevers were obtained by printing angled slices of 5 µm, and 3 µm thick. Minimum developing time is advised to be 24 hours, and the fluidic interface is advised not to be cleaned with acetone, as this will dissolve the polymer and can lead to clogging. A functional, 350 µm long cantilever has been printed, with a channel diameter of 25 µm.

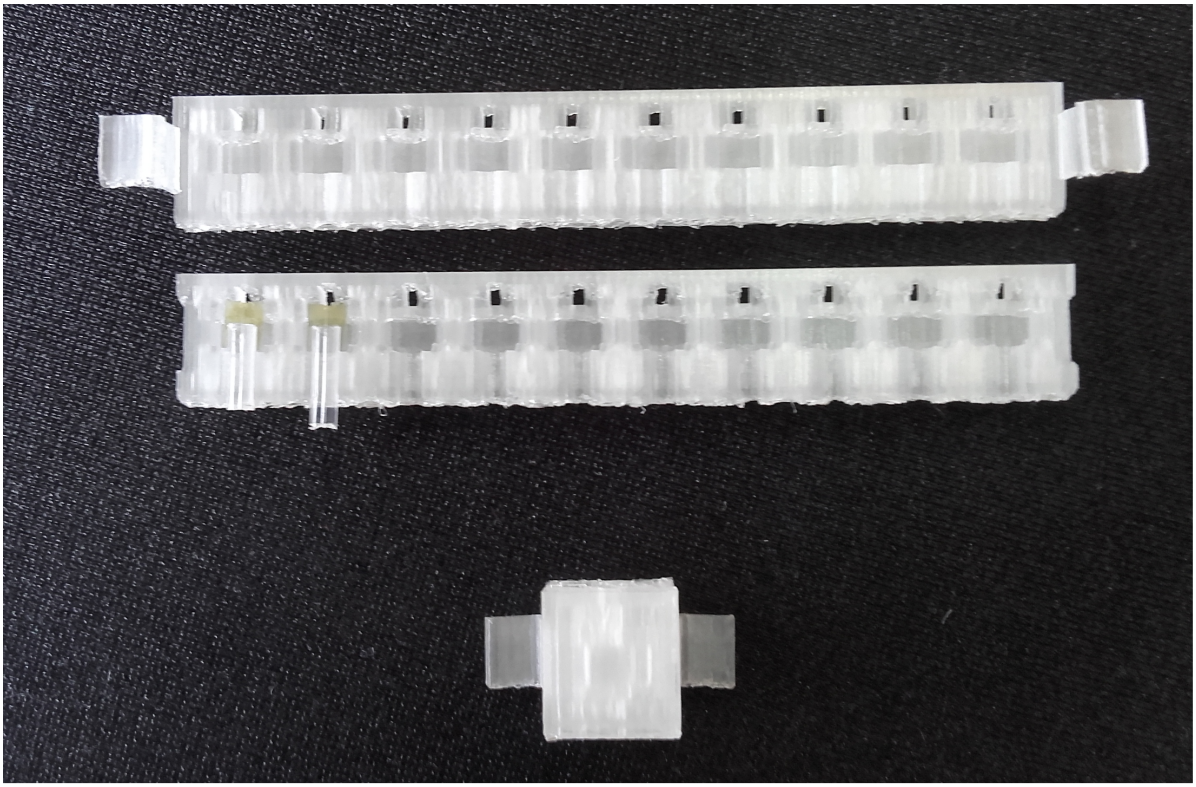


Figure A.32: Fused deposition modelling (FDM) 3D-printed device holder. The device consists of a top and a bottom. The fluidic interface connected to tubing can be inserted for secure handling. An open aperture enables a view of the cantilever. Ten devices can fit in the holder, but a single device holder has also been fabricated.

B

Characterization details

B.1. Mechanical characterization

The cantilever design of figure A.31 was mechanically characterised with a laser Doppler vibrometer (LDV) to obtain information about the amplitude-frequency relation. This is a non-contact vibration measurement device that uses the Doppler effect to detect minute velocities. A laser beam is shone onto a surface and reflected back with a slight frequency shift due to the Doppler effect caused by the vibrating structure. The interference pattern between this reflected beam and a reference beam provides the velocity information. The frequency response of one cantilever is shown in figure B.1 **A**, with a zoomed-in view around the peak in figure B.1 **B**. The data for two other cantilevers are plotted in figures B.2 and B.3.

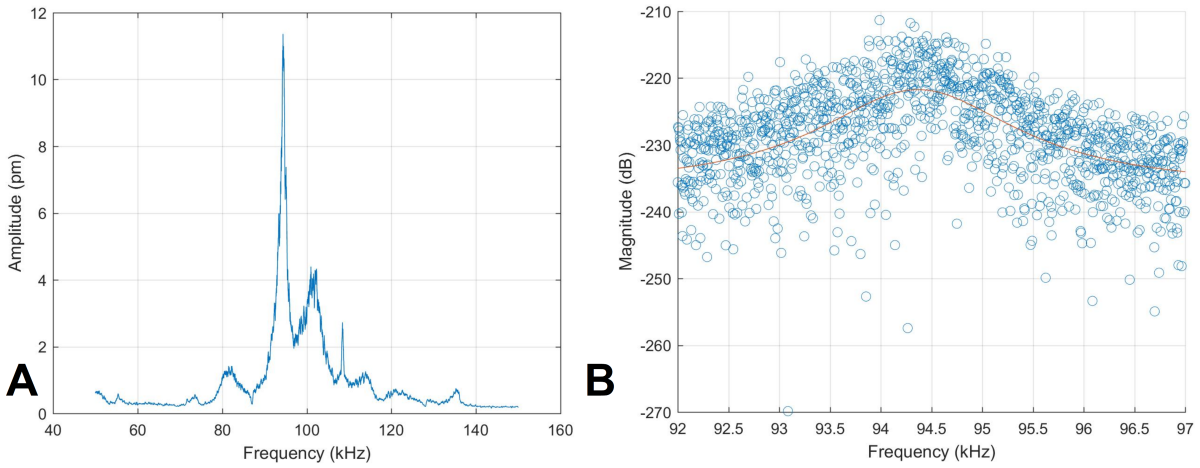


Figure B.1: **A)** Frequency sweep over the band 50 kHz to 150 kHz, with the resonance peak of the fundamental frequency at around 94 kHz. **B)** Scatter plot around the fundamental frequency, with the magnitude in decibels against the frequency; a lorentzian curve is fitted to the data points.

Table B.1 shows the comparison between an analytical and finite element model, and the experiment with the measurement errors. A possible explanation for these errors are that the Young's modulus of the photoresist depends on the laser power of the 2PP-device. The degree of crosslinking between monomers in acrylate-based photoresists depends on the writing speed and laser power [98]. The Young's modulus that was used for calculations was provided without knowledge of these dependencies, which means that the actual value for the measured device can deviate from this value. Even if the laser power and writing speed were known for this specific value, then still there would be deviations, as the laser power can fluctuate between printing sessions. Any of the other measurement devices and equipment contribute to this error.

Modes other than the fundamental mode are difficult to distinguish due to the amount of noise in the measurement signal. One possible cause is the cantilever surface, which is not flat and slightly curved. Ridges are

Table B.1: Comparison of the values of the eigenfrequency, stiffness, and the Young's modulus, obtained through an analytical and finite element model, and the experiment. *The Young's modulus of the analytical model is adopted from literature [87].

	Analytical model	**FEM**	**Experiment**
Eigenfrequency (kHz)	99	96	99.6 ± 6.2
Stiffness ($\mathrm{N\,m^{-1}}$)	15.55	14.76	15.8 ± 1.9
E-modulus (GPa)	4.6*	4.37	4.6 ± 0.5

formed between the printed cantilever slices and can deflect parts of the laser beam under different angles, losing signal in the process. Another cause could be the fact that the cantilever is not directly excited itself. The cantilever is connected to the 2PP-dome, which itself is connected to the SL-interface. This interface is in contact with the piezo-resistive element responsible for the oscillation. Energy is dissipated through these connections, and their resonance frequencies influence the measurement of the cantilever frequency response.

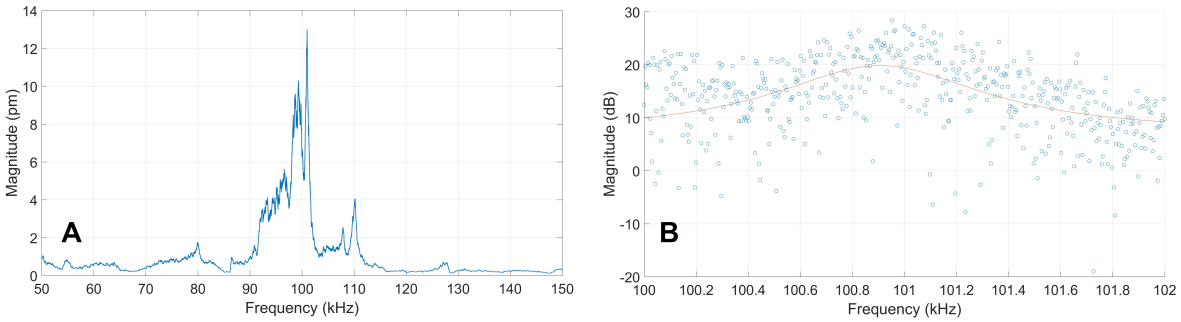


Figure B.2: **A)** Frequency sweep over the band 50 kHz to 150 kHz for a second cantilever, with the resonance peak of the fundamental frequency at around 100 kHz. **B)** Scatter plot around the fundamental frequency, with the magnitude in decibels against the frequency; a lorentzian curve is fitted to the data points.

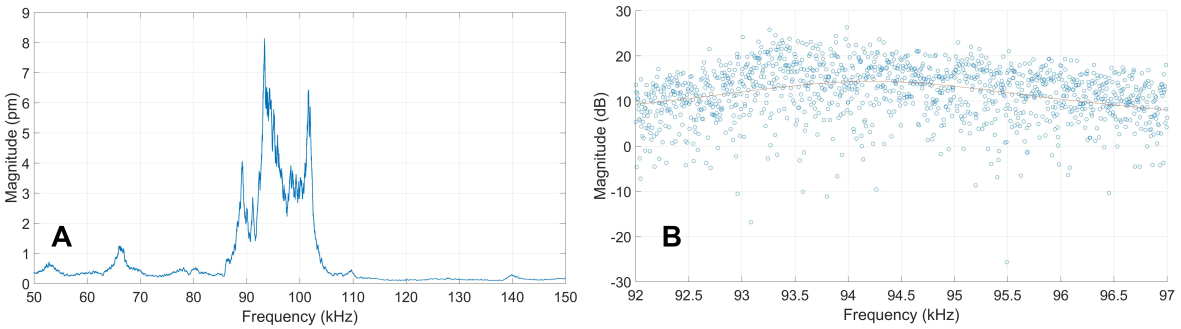


Figure B.3: **A)** Frequency sweep over the band 50 kHz to 150 kHz for a third cantilever, with the resonance peak of the fundamental frequency at around 94 kHz. **B)** Scatter plot around the fundamental frequency, with the magnitude in decibels against the frequency; a lorentzian curve is fitted to the data points.

Mode shapes for other eigenfrequencies were modelled and shown in figures B.4, B.5, and B.6.

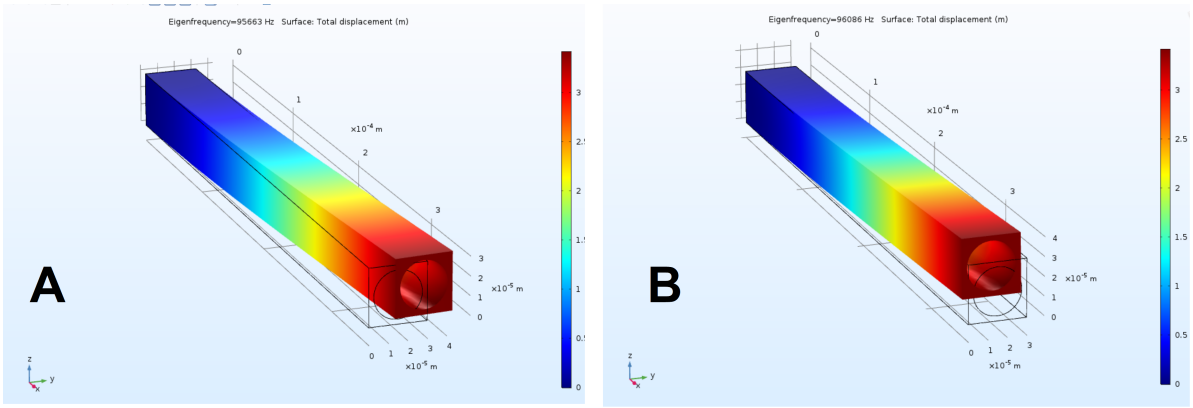


Figure B.4: Finite element model of the cantilever, **A)** first eigenfrequency, **B)** second eigenfrequency.

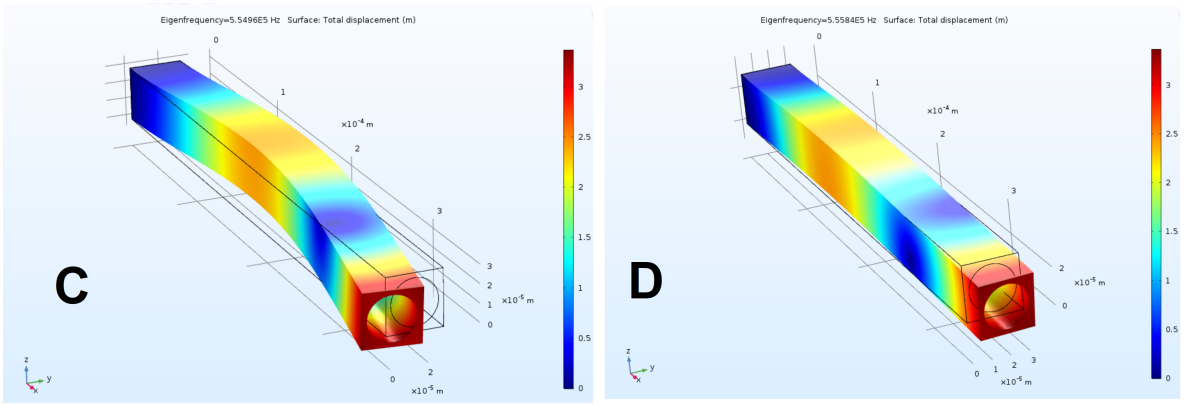


Figure B.5: Finite element model of the cantilever, **C)** third eigenfrequency, **D)** fourth eigenfrequency.

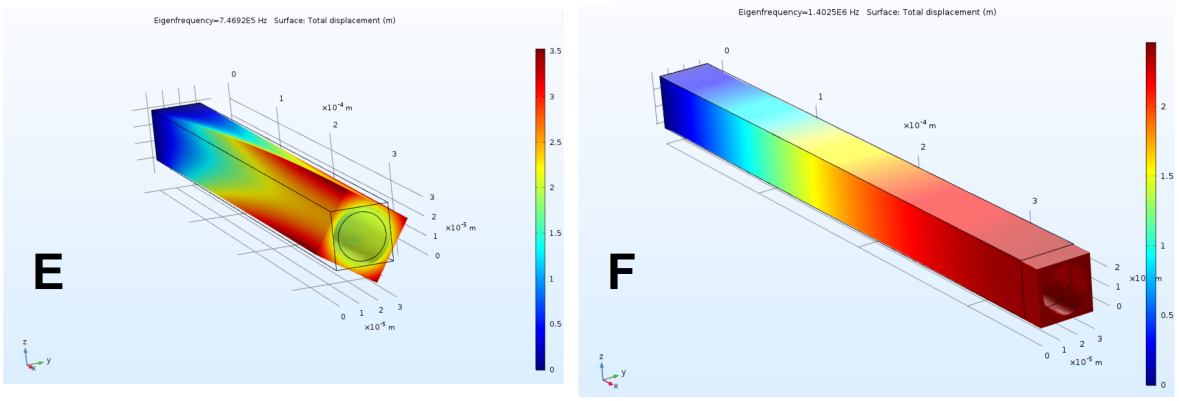


Figure B.6: Finite element model of the cantilever, **E)** fifth eigenfrequency, **F)** sixth eigenfrequency.

B.2. Attachment experiment

The attachment experiment was performed with blocks of 10 µm, 50 µm, 100 µm and 200 µm in the manner as shown in figure B.7 **A** and **B**. However, detachment was only observed for the blocks with the dimensions 100 µm^3 and 200 µm^3. In the paper only the data of the cubes that were detached was shown, therefore in this appendix the data of all blocks is plotted in figures B.8, B.9, B.10 and B.11 for the block dimensions of 200 µm^3, 100 µm^3, 50 µm^3 and 10 µm^3 respectively.

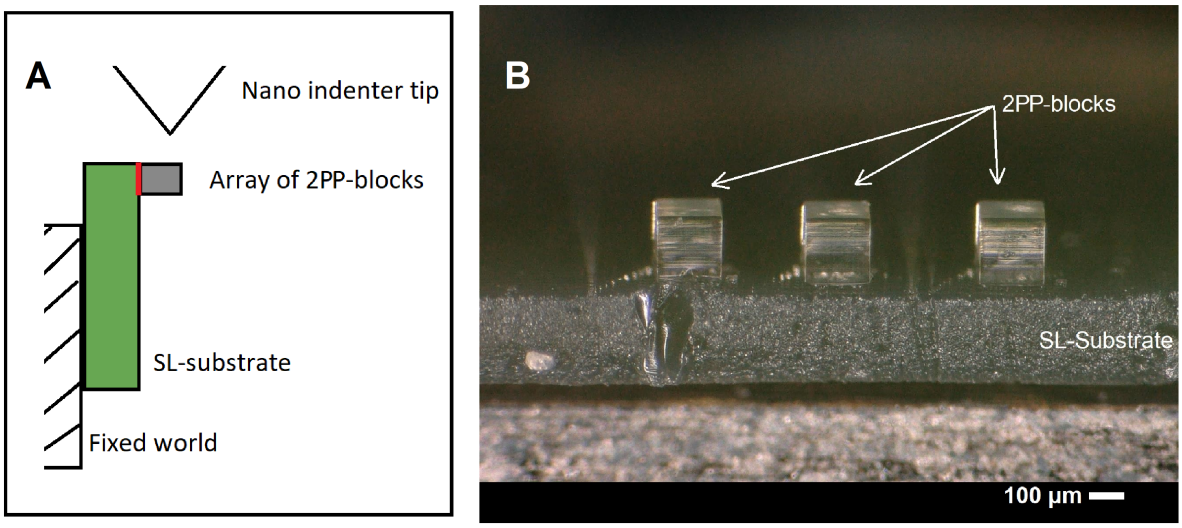


Figure B.7: **A)** Schematic sideview of the attachment experiment. The red strip indicates in the attachment area under test.
B) 200 µm^3 2PP-cubes that are printed on a SL-substrate. The cubes with other dimensions have been printed in a similar manner.

The force-distance curves obtained from the experiment reveal that the distance travelled by the nano indenter tip is not equal for some of the cubes, which is explained by the fact printing of these blocks was done by hand. In other words, the distance between the cube and the edge of the substrate has some variability in it. The full range of zero to 500 mN is plotted for every block, and some part of the unloading.

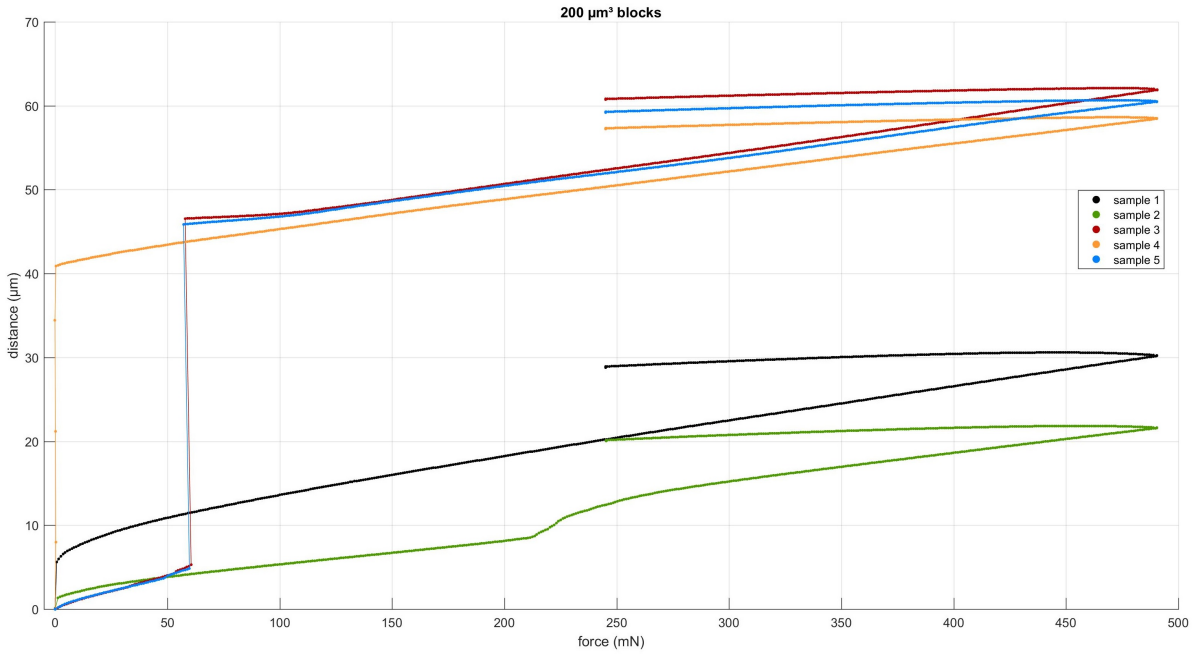


Figure B.8: Force - distance graphs of five samples of 200 µm^3 blocks, of which two samples were detached, namely samples 3 and 5. Detachment is visible as a sudden vertical jump, indicating a sudden detachment.

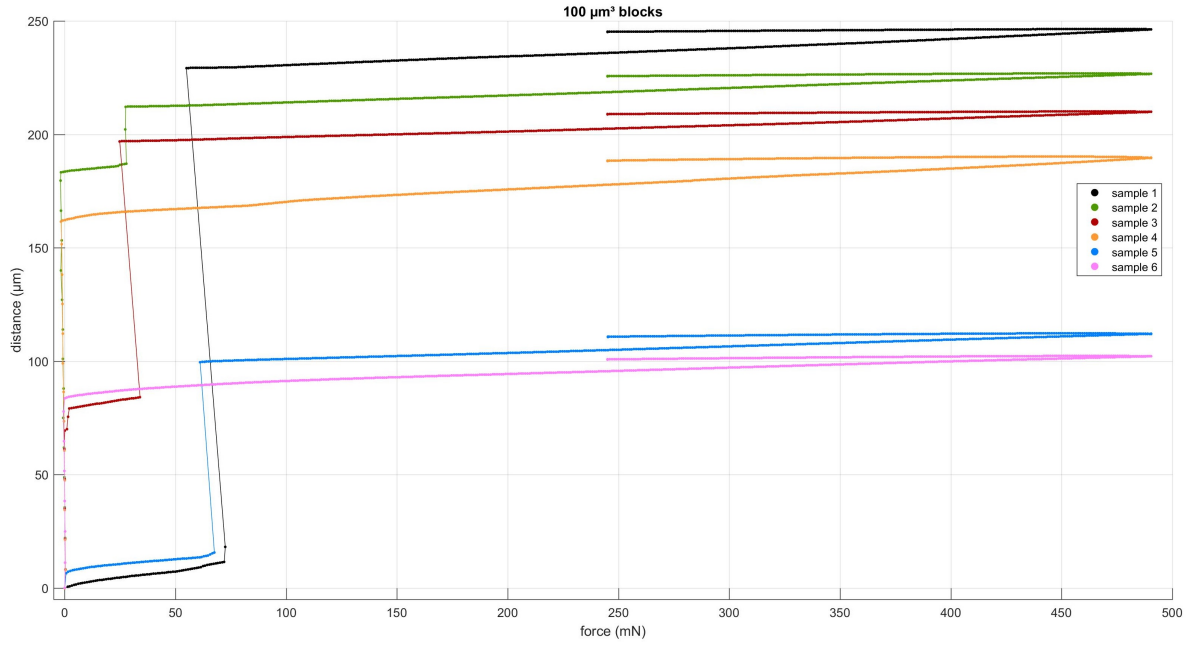


Figure B.9: Force - distance graphs of six samples of 100 µm^3 blocks, of which four samples were detached, namely samples 1, 2, 3, and 5. Detachment is visible as a sudden vertical jump, indicating a sudden detachment.

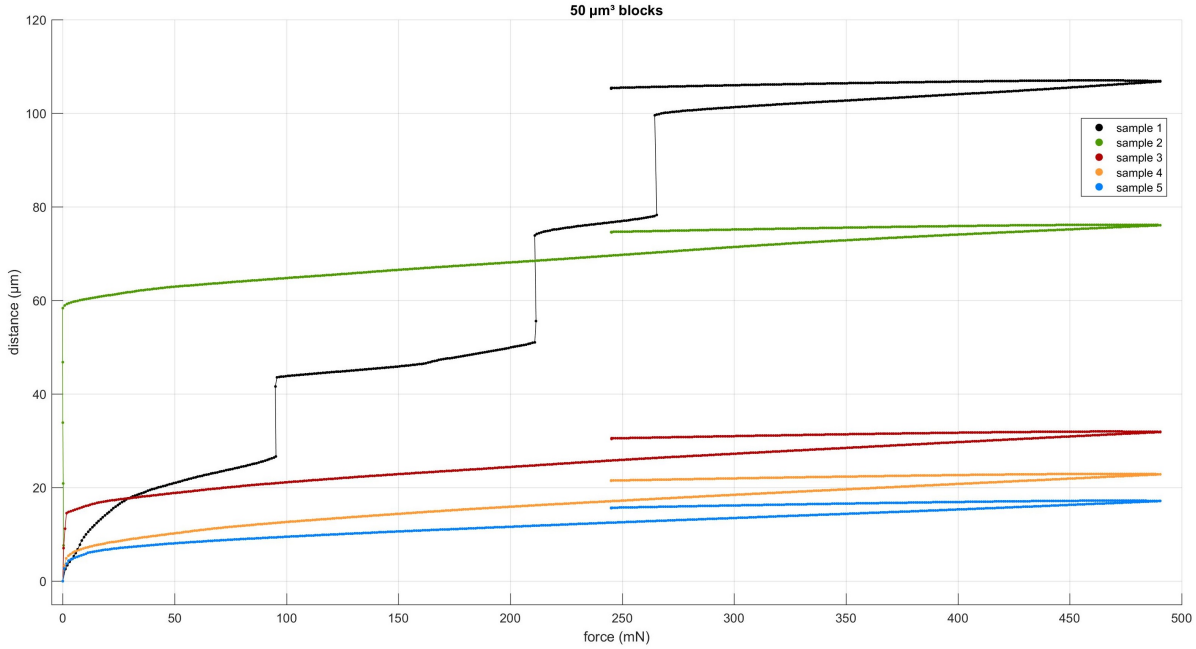


Figure B.10: Force - distance graphs of five samples of 50 µm^3 blocks, where none of the blocks were detached. The data from sample 1 shows regular jumps which can be explained by chipping of the SL-substrate material by the nano indenter tip.

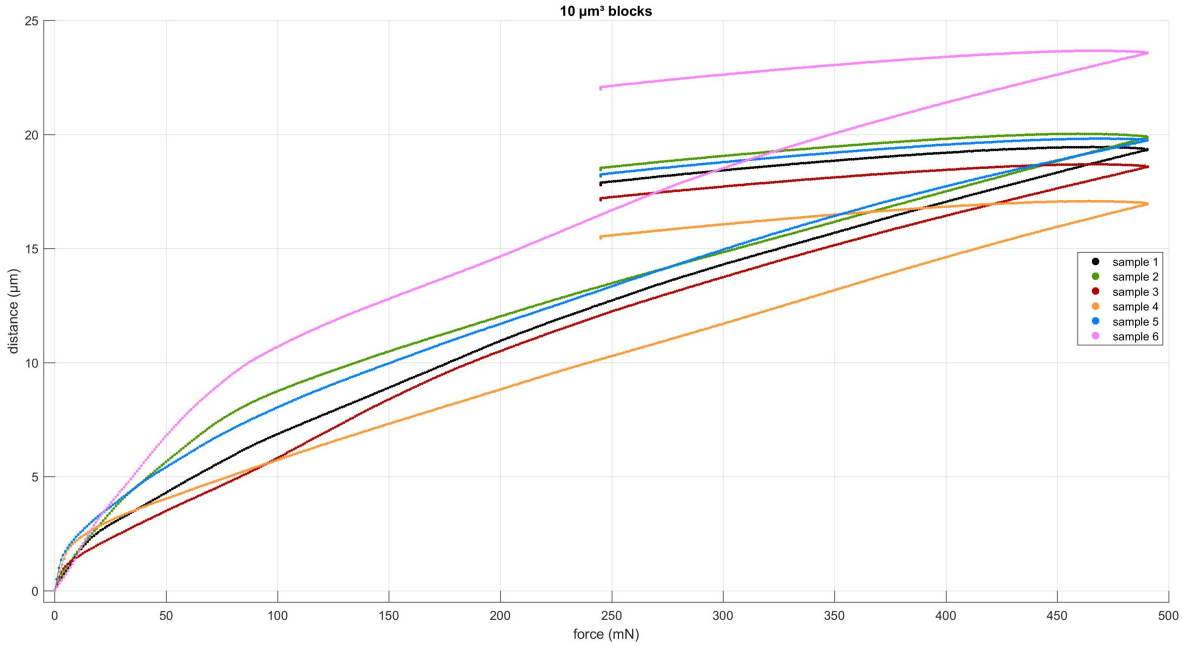


Figure B.11: Force - distance graphs of six samples of 10 μm^3 blocks, none of which were detached.

Figure B.12 shows a graph which can serve as a design guide for minimum cantilever aperture diameters and lengths for some values for the flow rate Q.

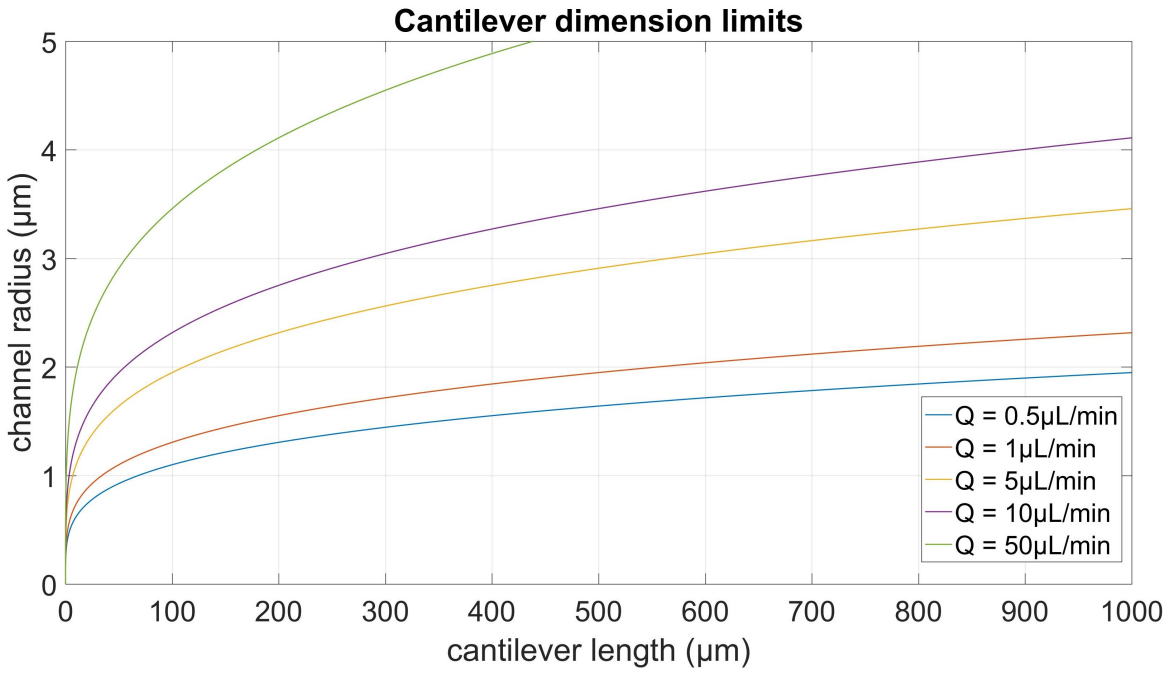


Figure B.12: Channel radius as a function of cantilever length, plotted for a selection of flow rates.

The figure shows that the minimum radius decreases with decreasing cantilever length. This is a result of the decrease in pressure drop when the length is shorter, and that directly decreases the channel resistance. A higher aperture resistance is then permissible for the same flow rate, resulting in a smaller radius.

These SL-substrates with blocks were glued on a fused deposition modelled 3D-printed pentagon to keep the

surface of the blocks perpendicular to the nano indenter tip. This pentagon is shown in figure B.13.

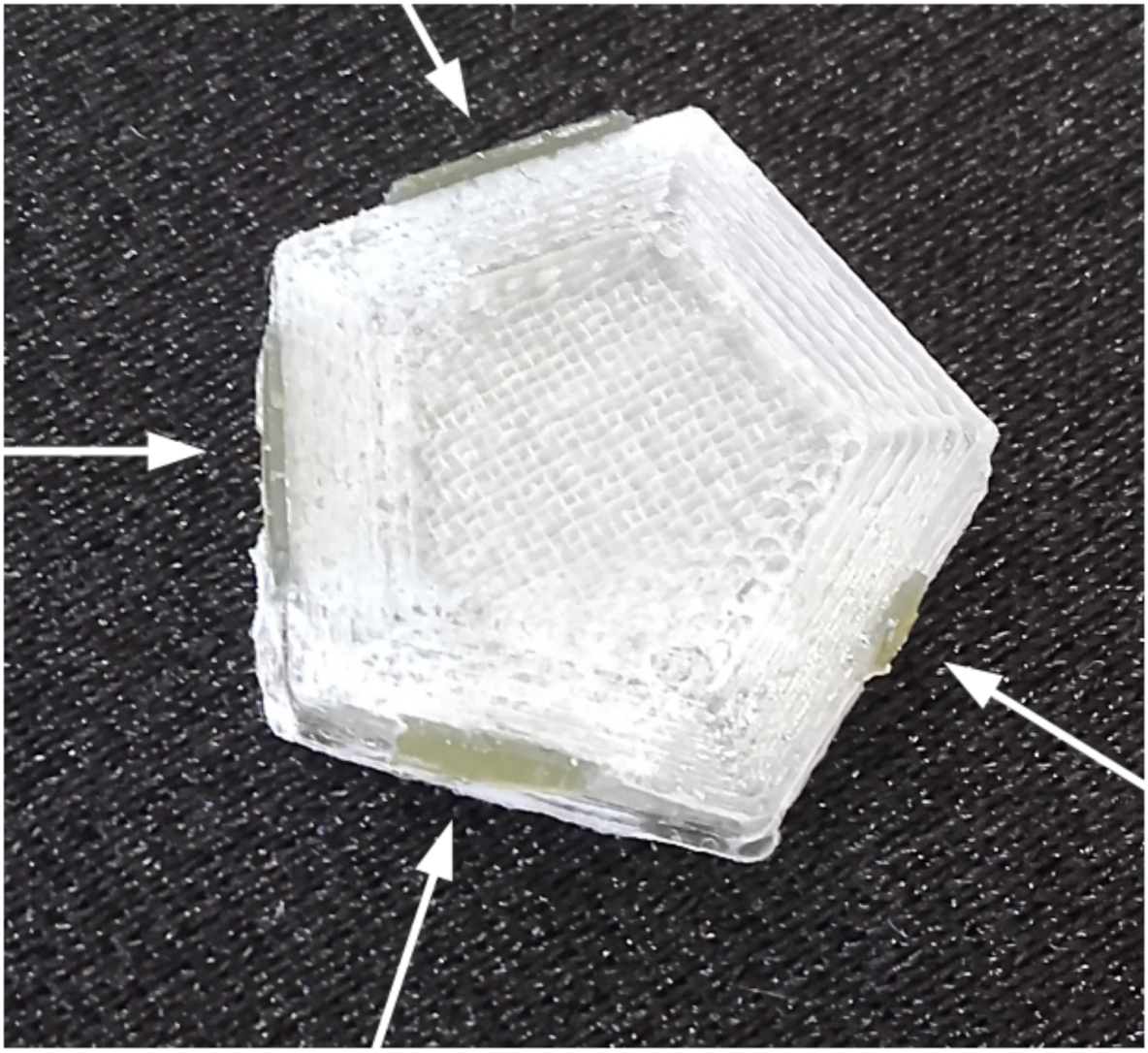


Figure B.13: FDM 3D-printed pentagon for the attachment test onto which the SL-plates with the 2PP-cubes is glued. The white arrows indicate the locations of the SL-plates.

B.3. Code

The code for a self written cantilever is supplemented here.

```
% File generated by DeScribe 2.5.1

% Strategy:
% 1. Find interface away from square
% 2. Lower microscope z-drive 530 µm (E-structure height is 400 µm)
% 3. Move to E-structure, distance between focus and structure = 130 µm
% 4. Raise microscope z-drive up 150 µm (new distance focus-structure =
40 µm, distance objective-tape = 230 µm)


% System initialization
InvertZAxis 1

% Writing configuration
GalvoScanMode
ContinuousMode
PiezoSettlingTime 10
GalvoSettlingTime 2
GalvoAcceleration 2
StageVelocity 200 % Enable for more accurate but slower stitching

% Scan field offsets
XOffset 0
YOffset 0
ZOffset 0

% after running the calibration file, insert a suitable value for 'cal'
here

var $cal = 0 % always <350 µm, otherwise the objective will hit the
structure

% Writing parameters
% laser power is <50 mW with powerscaling 1.0 and LP 100%

PowerScaling 1.0
var $LPstart                = 40

% Contour writing parameters
var $contourLaserPower      = 40
var $contourScanSpeed  = 60000
var $CSstart                = 60000

% Solid hatch lines writing parameters
var $solidLaserPower   = 40
var $solidScanSpeed    = 60000

% Base writing parameters
var $baseLaserPower    = $contourLaserPower
var $baseScanSpeed          = $contourScanSpeed

% Writing of structures
set $contourScanSpeed  = $CSstart
set $contourLaserPower      = $LPstart
```

```
set $solidLaserPower   = $contourLaserPower

MoveStageX 0
MovestageY 0

% Writing of reference moons
AddZDrivePosition $cal
Wait 5

% Enter desired cantilever dimensions here
var $cantilever_length = 250
var $channel_dim = 10
var $cantilever_dim = 20
var $hatching = 0.2

% loop variables
local $i = 0
local $j = 0
local $k = 0
local $l = 0
local $m = 0
var $znew =0
var $pi = 3.14159265359

var $cantilever_l_loop = $cantilever_length/(2*$hatching) % distance
between cantilever "slices" is 0.3 µm, so it's length is 0.3*$loopnumber

for $k = 0 to $cantilever_l_loop

      % horizontal +x top
      var $xplus_start = -0.5*$cantilever_dim
      var $xplus_stop = 0.5 * $cantilever_dim

      var $channel_xplus_stop=0
      var $channel_xplus_left_start = 0

      AddZOffset -0.5*$cantilever_dim

      for $l = 0 to $cantilever_dim - $channel_dim
            $xplus_start     0          0
            $xplus_stop      0          0
            Write
            AddZOffset 0.5
      end

      % channel
      for $i = 1 to 2 * $channel_dim-1

      set $znew = -0.5*$channel_dim + 0.5*$i
      set $channel_xplus_stop       = -(sqrt(pow(0.5*$channel_dim, 2) -
pow($znew, 2)))
      set $channel_xplus_left_start = (sqrt(pow(0.5*$channel_dim, 2) -
pow($znew, 2)))
```

```
            $xplus_start                0           0
            $channel_xplus_stop         0           0
            Write
            $channel_xplus_left_start   0           0
            $xplus_stop                         0           0
            Write

            AddZOffset 0.5
    end

% horizontal +x bottom
      for $l = 0 to $cantilever_dim - $channel_dim
            $xplus_start     0          0
            $xplus_stop      0          0
            Write
            AddZOffset 0.5
      end

      AddZOffset -0.5*$cantilever_dim-0.5
      AddYOffset -$hatching


      % horizontal -x top
      var $xplus_start = 0.5*$cantilever_dim
      var $xplus_stop = -0.5 * $cantilever_dim

      var $channel_xplus_stop=0
      var $channel_xplus_left_start = 0

      AddZOffset -0.5*$cantilever_dim

      for $l = 0 to $cantilever_dim - $channel_dim
            $xplus_start     0          0
            $xplus_stop      0          0
            Write
            AddZOffset 0.5
      end

      % channel
      for $i = 1 to 2 * $channel_dim-1

      set $znew = -0.5*$channel_dim + 0.5*$i
      set $channel_xplus_stop       = (sqrt(pow(0.5*$channel_dim, 2) -
pow($znew, 2)))
      set $channel_xplus_left_start = -(sqrt(pow(0.5*$channel_dim, 2) -
pow($znew, 2)))


            $xplus_start                0           0
            $channel_xplus_stop         0           0
            Write
            $channel_xplus_left_start   0           0
            $xplus_stop                         0           0
```

```
            Write

            AddZOffset 0.5
    end

% horizontal -x bottom
      for $l = 0 to $cantilever_dim - $channel_dim
            $xplus_start     0          0
            $xplus_stop      0          0
            Write
            AddZOffset 0.5
      end

      AddZOffset -0.5*$cantilever_dim-0.5
    AddYOffset -$hatching
end
```

Bibliography

[1] G. Binnig, H. Rohrer, C. Gerber, and E. Weibel. Surface studies by scanning tunneling microscopy. *Physical review letters*, 49(1):57–61, 1982.

[2] G. Binnig and C. F. Quate. Atomic Force Microscope. *Physical Review Letters*, 56(9):930–933, 1986.

[3] Hans Jürgen Butt, Brunero Cappella, and Michael Kappl. Force measurements with the atomic force microscope: Technique, interpretation and applications. *Surface Science Reports*, 59(1-6):1–152, 2005.

[4] AJC1. AFM principle. *Creative Commons License, downloaded on 22 Dec. 2017*, 2010. https://www.flickr.com/photos/ajc1/4808817852/in/photostream/.

[5] B Drake, C. Prater, A. Weisenhorn, S. Gould, T. Albrecht, C. Quate, D. Cannell, H. Hansma, and P. Hansma. Imaging crystals, polymers, and processes in water with the atomic force microscope. *Science*, 243(4898):1586–1589, 1989.

[6] Yves F. Dufrêne, Toshio Ando, Ricardo Garcia, David Alsteens, David Martinez-Martin, Andreas Engel, Christoph Gerber, and Daniel J. Müller. Imaging modes of atomic force microscopy for application in molecular and cell biology. *Nature Nanotechnology*, 12(4):295–307, 2017.

[7] Leo Gross, Z L Wang, D Ugarte, Fabian Mohn, Nikolaj Moll, W a Heer, P Vincent, Peter Liljeroth, C Journet, Gerhard Meyer, V T Binh, M Poot, H S J Van Der Zant, a Aguasca, a Bachtold, K Kim, a Zettl, P Hung, H W C Postma, M Bockrath, X Blase, and S Roche. only appears when looking at the I. *Science*, 325(August):1110–4, 2009.

[8] S. Herminghaus, A. Fery, and D. Reim. Imaging of droplets of aqueous solutions by tapping-mode scanning force microscopy. *Ultramicroscopy*, 69(3):211–217, 1997.

[9] D. K. Schweizer and E. K. Eigler. Positioning single atoms with a scanning tunneling microscop, 1990.

[10] Yoshiaki Sugimoto, Masayuki Abe, Shinji Hirayama, Noriaki Oyabu, Óscar Custance, and Seizo Morita. Atom inlays performed at room temperature using atomic force microscopy. *Nature Materials*, 4(2):156–159, 2005.

[11] Richard D Piner, Jin Zhu, Feng Xu, and Seunghun Hong. "Dip-Pen" Nanolithography. *Science*, 283(January):661–664, 1999.

[12] R. V. Martínez, N. S. Losilla, J. Martínez, Y. Huttel, and R. Garcia. Patterning polymeric structures with 2 nm resolution at 3 nm half pitch in ambient conditions. *Nano Letters*, 7(7):1846–1850, 2007.

[13] T K Chowdhury. Fabrication of extremely fine glass micropipette electrodes. *Journal of Scientific Instruments*, 2(2):1087–1090, 1969.

[14] Shmuel Shalom, Klony Lieberman, Aaron Lewis, and Sidney R. Cohen. A micropipette force probe suitable for near-field scanning optical microscopy. *Review of Scientific Instruments*, 63(9):4061–4065, 1992.

[15] Aaron Lewis, Yuri Kheifetz, Efim Shambrodt, Anna Radko, Edward Khatchatryan, and Chaim Sukenik. Fountain pen nanochemistry: Atomic force control of chrome etching. *Applied Physics Letters*, 75(17):2689–2691, 1999.

[16] A. Meister, S. Jeney, M. Liley, T. Akiyama, U. Staufer, N. F. De Rooij, and H. Heinzelmann. Nanoscale dispensing of liquids through cantilevered probes. *Microelectronic Engineering*, 67-68(2003):644–650, 2003.

[17] A. Meister, M. Liley, J. Brugger, R. Pugin, and H. Heinzelmann. Nanodispenser for attoliter volume deposition using atomic force microscopy probes modified by focused-ion-beam milling. *Applied Physics Letters*, 85(25):6260–6262, 2004.

[18] Keun Ho Kim, Nicolaie Moldovan, and Horacio D. Espinosa. A nanofountain probe with Sub-100 nm molecular writing resolution. *Small*, 1(6):632–635, 2005.

[19] Nicolaie Moldovan, Keun Ho Kim, and Horacio D. Espinosa. Design and fabrication of a novel microfluidic nanoprobe. *Journal of Microelectromechanical Systems*, 15(1):204–213, 2006.

[20] N Moldovan, K-H Kim, and H D Espinosa. A multi-ink linear array of nanofountain probes. *Journal of Micromechanics and Microengineering*, 16(10):1935–1942, 2006.

[21] Takayuki Shibata, Kenji Nakamura, Shuhei Horiike, Moeto Nagai, Takahiro Kawashima, Takashi Mineta, and Eiji Makino. Fabrication and characterization of bioprobe integrated with a hollow nanoneedle for novel AFM applications in cellular function analysis. *Microelectronic Engineering*, 111:325–331, 2013.

[22] André Meister, Michael Gabi, Pascal Behr, Philipp Studer, János Vörös, Philippe Niedermann, Joanna Bitterli, Jérôme Polesel-Maris, Martha Liley, Harry Heinzelmann, and Tomaso Zambelli. FluidFM: Combining Atomic Force Microscopy and Nano uidics in a Universal Liquid Delivery System for Single Cell Applications and Beyond. *Nano Letters*, 9(6):2501–7, 2009.

[23] Hector Hugo Perez Garza, Murali Krishna Ghatkesar, and Urs Staufer. Aspiration through hollow cantilever-based nanopipette by means of evaporation. *Micro & Nano Letters*, 8(11):758–761, 2013.

[24] Murali Krishna Ghatkesar, Hector Hugo Perez Garza, and Urs Staufer. Hollow AFM cantilever pipette. *Microelectronic Engineering*, 124:22–25, 2014.

[25] Ralph van Oorschot, Hector Perez Garza, Roy J S Derks, Urs Staufer, and Murali Ghatkesar. A microfluidic AFM cantilever based dispensing and aspiration platform. *EPJ Techniques and Instrumentation*, 2(1):1–11, 2015.

[26] Murali Krishna Ghatkesar, Hector Hugo Perez Garza, Friedjof Heuck, and Urs Staufer. Scanning probe microscope-based fluid dispensing. *Micromachines*, 5(4):954–1001, 2014.

[27] Angelo Gaitas and Robert W Hower. SU-8 microcantilever with an aperture, fluidic channel, and sensing mechanisms for biological and other applications. *J Micro Nanolithogr MEMS MOEMS*, 13(3):1–8, 2014.

[28] Vincent Martinez, Csaba Forró, Serge Weydert, Mathias J. Aebersold, Harald Dermutz, Orane Guillaume-Gentil, Tomaso Zambelli, Janos Voros, and László Demkó. Controlled single-cell deposition and patterning by highly flexible hollow cantilevers. *Lab Chip*, 2(2):303, 2016.

[29] Vincent Martinez, Pascal Behr, Ute Drechsler, Jérôme Polesel-Maris, Eva Potthoff, Janos Vörös, and Tomaso Zambelli. SU-8 hollow cantilevers for AFM cell adhesion studies. *Journal of Micromechanics and Microengineering*, 26(5):055006, 2016.

[30] F J Giessibl. Exploring the nanoworld with atomic force microscopy (vol 59, pg 9, 2006). *Physics Today*, 60(1):17, 2006.

[31] Franz J. Giessibl. Advances in atomic force microscopy. *Reviews of Modern Physics*, 75(3):949–983, 2003.

[32] T R Albrecht, P Grtitter, D Horne, and D Rugar. Frequency modulation detection using highdkantilevers microscope sensitivity for enhanced force. *Journal of Applied Physics*, 69(2):668–674, 1991.

[33] Stephanie Rinaldi, Sairam Prabhakar, Srikar Vengallatore, and Michael P. Païdoussis. Dynamics of microscale pipes containing internal fluid flow: Damping, frequency shift, and stability. *Journal of Sound and Vibration*, 329(8):1081–1088, 2010.

[34] K. Hu, Y. K. Wang, H. L. Dai, L. Wang, and Q. Qian. Nonlinear and chaotic vibrations of cantilevered micropipes conveying fluid based on modified couple stress theory. *International Journal of Engineering Science*, 105:93–107, 2016.

[35] P. Belardinelli, M. K. Ghatkesar, U. Staufer, and F. Alijani. Linear and non-linear vibrations of fluid-filled hollow microcantilevers interacting with small particles. *International Journal of Non-Linear Mechanics*, 93(November 2016):30–40, 2017.

[36] Kwang W Oh, Kangsun Lee, and Edward P Furlani. Lab on a Chip Design of pressure-driven microfluidic networks using electric circuit analogy. pages 515–545, 2012.

[37] Patrick Tabeling. *Introduction to microfluidics*. Oxford University Press, 2005.

[38] N. Mojarad, M. Hojeij, L. Wang, J. Gobrecht, and Y. Ekinci. Single-digit-resolution nanopatterning with extreme ultraviolet light for the 2.5 nm technology node and beyond. *Nanoscale*, 7(9):4031–4037, 2015.

[39] Marc J. Madou. *Fundamentals of Microfabrication and Nanotechnology: Manufacturing Techniques for Microfabrication and Nanotechnology, vol. 2*. Boca Raton, FL: CRC Press I Llc, 2011.

[40] Sidra Waheed, Joan M. Cabot, Niall P. Macdonald, Trevor Lewis, Rosanne M. Guijt, Brett Paull, and Michael C. Breadmore. 3D printed microfluidic devices: enablers and barriers. *Lab Chip*, 16(11):1993–2013, 2016.

[41] Ferry P.W. Melchels, Jan Feijen, and Dirk W. Grijpma. A review on stereolithography and its applications in biomedical engineering. *Biomaterials*, 31(24):6121–6130, 2010.

[42] Shoji Maruo and Koji Ikuta. Submicron stereolithography for the production of freely movable mechanisms by using single-photon polymerization. *Sensors and Actuators, A: Physical*, 100(1):70–76, 2002.

[43] John T Fourkas. *Chapter 1.3 - Fundamentals of Two-Photon Fabrication*. Elsevier Inc., 2016.

[44] Xiaoqin Zhou, Yihong Hou, and Jieqiong Lin. A review on the processing accuracy of two-photon polymerization. *AIP Advances*, 5(3), 2015.

[45] Andrea M. Kasko. Degradable Poly(ethylene glycol) Hydrogels for 2D and 3D Cell Culture. *downloaded on 05/01/2018*, 000. https://www.sigmaaldrich.com/technical-documents/articles/material-matters/degradable-polyethylene-glycol-hydrogels.html.

[46] Orane Guillaume-Gentil, Eva Potthoff, Dario Ossola, Clemens M. Franz, Tomaso Zambelli, and Julia A. Vorholt. Force-controlled manipulation of single cells: From AFM to FluidFM. *Trends in Biotechnology*, 32(7):381–388, 2014.

[47] Keun Ho Kim, Raymond G. Sanedrin, Andrea M. Ho, Seung W. Lee, Nicolaie Moldovan, Chad A. Mirkin, and Horacio D. Espinosa. Direct delivery and submicrometer patterning of DNA by a nanofountain probe. *Advanced Materials*, 20(2):330–334, 2008.

[48] Owen Loh, Robert Lam, Mark Chen, Nicolaie Moldovan, Houjin Huang, Dean Ho, and Horacio D. Espinosa. Nanofountain-probe-based high-resolution patterning and single-cell injection of functionalized nanodiamonds. *Small*, 5(14):1667–1674, 2009.

[49] Hector Hugo Perez Garza, Murali Krishna Ghatkesar, Per Lothman, Andreas Manz, and Urs Staufer. Enabling local deposition and controlled synthesis of Au-nanoparticles using a femtopipette. *9th IEEE International Conference on Nano/Micro Engineered and Molecular Systems, IEEE-NEMS 2014*, pages 323–328, 2014.

[50] Keir C Neuman and Attila Nagy. Single-molecule force spectroscopy: optical tweezers, magnetic tweezers and atomic force microscopy. *Nature Methods*, 5(6):491–505, 2008.

[51] P. L. T. M. Frederix, B. W. Hoogenboom, D Fotiadis, D. J. Müller, and A. Engel. Atomic Force. *Imaging*, pages 449–455, 2017.

[52] C Bustamante, S B Smith, J Liphardt, and D Smith. Single-molecule studies of DNA mechanics. *Current opinion in structural biology*, 10(3):279–285, 2000.

[53] Dimas G. de Oteyza, Patrick Gorman, Yen-Chia Chen, Sebastian Wickenburg, Alexander Riss, Duncan J. Mowbray, Grisha Etkin, Zahra Pedramrazi, Hsin-Zon Tsai, Angel Rubio, Michael F. Crommie, and Felix R. Fischer. Direct Imaging of Covalent Bond Structure in Signle-Molecule Chemical Reactions. *Science*, 340(6139):1434–1437, 2013.

[54] K Tomankova and P Kolar. Mechanical characterisation of HeLa cells using atomic force microscopy. *Current Microscopy . . .*, pages 549–554, 2012.

[55] Alper D. Ozkan, Ahmet E. Topal, Fatma B. Dikecoglu, Mustafa O. Guler, Aykutlu Dana, and Ayse B. Tekinay. Probe microscopy methods and applications in imaging of biological materials. *Seminars in Cell & Developmental Biology*, 2017.

[56] Gajendra S Shekhawat, Steven M Dudek, and Vinayak P Dravid. Development of ultrasound bioprobe for biological imaging. *Science Advances*, 3(October):1–6, 2017.

[57] R Pechmann, W Fritzsche, A Schaper, and Electronic Vi. The Novolever : microfabricated A new cantilever for scanning from polymeric materials force microscopy. *Review of Scientific instruments*, 65(12):0–4, 1994.

[58] Fangzhou Yu, Jiangbo Liu, Xiao Zhang, Ai-Lian Lin, Nabeela Khan, Yanbiao Pan, Nan Gao, Qingze Zou, and Jaeseok Jeon. Design, fabrication, and characterization of polymer-based cantilever probes for atomic force microscopes. *Journal of Vacuum Science & Technology B, Nanotechnology and Microelectronics: Materials, Processing, Measurement, and Phenomena*, 34(6):06KI01, 2016.

[59] Andreas Schneider, Robert H. Ibbotson, Richard J. Dunn, and Ejaz Huq. Arrays of SU-8 microcantilevers with integrated piezoresistive sensors for parallel AFM applications. *Microelectronic Engineering*, 88(8):2390–2393, 2011.

[60] Maria Nordström, Stephan Keller, Michael Lillemose, Alicia Johansson, Søren Dohn, Daniel Haefliger, Gabriela Blagoi, Mogens Havsteen-Jakobsen, and Anja Boisen. SU-8 Cantilevers for Bio/chemical Sensing; Fabrication, Characterisation and Development of Novel Read-out Methods. *Sensors*, 8(3):1595–1612, 2008.

[61] Gerald Göring, Philipp Immanuel Dietrich, Matthias Blaicher, Swati Sharma, Jan G. Korvink, Thomas Schimmel, Christian Koos, and Hendrik Hölscher. Tailored probes for atomic force microscopy fabricated by two-photon polymerization. *Applied Physics Letters*, 109(6), 2016.

[62] Norihisa Kato, Takahiro Kawashima, Takayuki Shibata, Takashi Mineta, and Eiji Makino. Micromachining of a newly designed AFM probe integrated with hollow microneedle for cellular function analysis. *Microelectronic Engineering*, 87(5-8):1185–1189, 2010.

[63] Kilho Eom, Harold S. Park, Dae Sung Yoon, and Taeyun Kwon. Nanomechanical resonators and their applications in biological/chemical detection: Nanomechanics principles. *Physics Reports*, 503(4-5):115–163, 2011.

[64] Thomas P. Burg, Michel Godin, Scott M. Knudsen, Wenjiang Shen, Greg Carlson, John S. Foster, Ken Babcock, and Scott R. Manalis. Weighing of biomolecules, single cells and single nanoparticles in fluid. *Nature*, 446(7139):1066–1069, 2007.

[65] Hashem Etayash, M. F. Khan, Kamaljit Kaur, and Thomas Thundat. Microfluidic cantilever detects bacteria and measures their susceptibility to antibiotics in small confined volumes. *Nature Communications*, 7:12947, 2016.

[66] Helen Bridle, Wenxing Wang, Despoina Gavriilidou, Farid Amalou, Duncan P. Hand, and Wenmiao Shu. Static mode microfluidic cantilevers for detection of waterborne pathogens. *Sensors and Actuators, A: Physical*, 247:144–149, 2016.

[67] Hamid SadAbadi and Muthukumaran Packirisamy. Nano-Integrated Suspended Polymeric Microfluidics (SPMF) Platform for Ultra-Sensitive Bio-Molecular Recognition of Bovine Growth Hormones. *Scientific Reports*, 7(1):1–10, 2017.

[68] S. Olcum, N. Cermak, S. C. Wasserman, K. S. Christine, H. Atsumi, K. R. Payer, W. Shen, J. Lee, A. M. Belcher, S. N. Bhatia, and S. R. Manalis. Weighing nanoparticles in solution at the attogram scale. *Proceedings of the National Academy of Sciences*, 111(4):1310–1315, 2014.

[69] Thomas Braun, Viola Barwich, Murali Krishna Ghatkesar, Adriaan H. Bredekamp, Christoph Gerber, Martin Hegner, and Hans Peter Lang. Micromechanical mass sensors for biomolecular detection in a physiological environment. *Physical Review E - Statistical, Nonlinear, and Soft Matter Physics*, 72(3):1–9, 2005.

[70] Thomas P. Burg, John E. Sader, and Scott R. Manalis. Nonmonotonic energy dissipation in microfluidic resonators. *Physical Review Letters*, 102(22):1–4, 2009.

[71] W. H. Grover, A. K. Bryan, M. Diez-Silva, S. Suresh, J. M. Higgins, and S. R. Manalis. Measuring single-cell density. *Proceedings of the National Academy of Sciences*, 108(27):10992–10996, 2011.

[72] Nathan Cermak, Selim Olcum, Francisco Feijó Delgado, Steven C. Wasserman, Kristofor R. Payer, Mark A. Murakami, Scott M. Knudsen, Robert J. Kimmerling, Mark M. Stevens, Yuki Kikuchi, Arzu Sandikci, Masaaki Ogawa, Vincent Agache, François Baléras, David M. Weinstock, and Scott R. Manalis. High-throughput measurement of single-cell growth rates using serial microfluidic mass sensor arrays. *Nature Biotechnology*, 34(10):1052–1059, 2016.

[73] Mark M. Stevens, Cecile L. Maire, Nigel Chou, Mark A. Murakami, David S. Knoff, Yuki Kikuchi, Robert J. Kimmerling, Huiyun Liu, Samer Haidar, Nicholas L. Calistri, Nathan Cermak, Selim Olcum, Nicolas A. Cordero, Ahmed Idbaih, Patrick Y. Wen, David M. Weinstock, Keith L. Ligon, and Scott R. Manalis. Drug sensitivity of single cancer cells is predicted by changes in mass accumulation rate. *Nature Biotechnology*, 34(11):1161–1167, 2016.

[74] Celso Accoto, Antonio Qualtieri, Ferruccio Pisanello, Carlo Ricciardi, Candido Fabrizio Pirri, Massimo De Vittorio, and Francesco Rizzi. Two-Photon Polymerization Lithography and Laser Doppler Vibrometry of a SU-8-Based Suspended Microchannel Resonator. *Journal of Microelectromechanical Systems*, 24(4):1038–1042, 2015.

[75] Wei Xiong, Yun Shen Zhou, Xiang Nan He, Yang Gao, Masoud Mahjouri-Samani, Lan Jiang, Tommaso Baldacchini, and Yong Feng Lu. Simultaneous additive and subtractive three-dimensional nanofabrication using integrated two-photon polymerization and multiphoton ablation. *Light: Science and Applications*, 1(APRIL):1–4, 2012.

[76] Aliaa I. Shallan, Petr Smejkal, Monika Corban, Rosanne M. Guijt, and Michael C. Breadmore. Cost-effective three-dimensional printing of visibly transparent microchips within minutes. *Analytical Chemistry*, 86(6):3124–3130, 2014.

[77] Alireza Ahmadian Yazdi, Adam Popma, William Wong, Tammy Nguyen, Yayue Pan, and Jie Xu. 3D printing: an emerging tool for novel microfluidics and lab-on-a-chip applications. *Microfluidics and Nanofluidics*, 20(3):1–18, 2016.

[78] Paulius Danilevicius. Micro-structured polymer scaffolds fabricated by direct laser writing for tissue engineering. *Journal of Biomedical Optics*, 17(8):081405, 2012.

[79] V Melissinaki, A A Gill, I Ortega, M Vamvakaki, A Ranella, J W Haycock, C Fotakis, M Farsari, and F Claeyssens. Direct laser writing of 3D scaffolds for neural tissue engineering applications. *Biofabrication*, 3(4):045005, 2011.

[80] Emmanuel Stratakis, Hojeong Jeon, and Sangmo Koo. Structures for biomimetic, fluidic, and biological applications. *MRS Bulletin*, 41(12):993–1001, 2016.

[81] Alexandros Selimis, Vladimir Mironov, and Maria Farsari. Direct laser writing: Principles and materials for scaffold 3D printing. *Microelectronic Engineering*, 132:83–89, 2014.

[82] Georg Von Freymann, Alexandra Ledermann, Michael Thiel, Isabelle Staude, Sabine Essig, Kurt Busch, and Martin Wegener. Three-dimensional nanostructures for photonics. *Advanced Functional Materials*, 20(7):1038–1052, 2010.

[83] Jesper Glückstad, Darwin Z. Palima, Mark Villangca, and Andrew Banas. 3D light robotics. *Proceedings of SPIE*, 9738:97380A, 2016.

[84] Tobias Frenzel, Claudio Findeisen, Muamer Kadic, Peter Gumbsch, and Martin Wegener. Tailored Buckling Microlattices as Reusable Light-Weight Shock Absorbers. *Advanced Materials*, pages 5865–5870, 2016.

[85] Hong Xia, Juan Wang, Ye Tian, Qi-Dai Chen, Xiao-Bo Du, Yong-Lai Zhang, Yan He, and Hong-Bo Sun. Ferrofluids for Fabrication of Remotely Controllable Micro-Nanomachines by Two-Photon Polymerization. *Advanced Materials*, 22(29):3204–3207, 2010.

[86] Laura Piedad Chia Gomez, Arnaud Spangenberg, Xuan Anh Ton, Yannick Fuchs, Frank Bokeloh, Jean Pierre Malval, Bernadette Tse Sum Bui, Damien Thuau, Cédric Ayela, Karsten Haupt, and Olivier Soppera. Rapid Prototyping of Chemical Microsensors Based on Molecularly Imprinted Polymers Synthesized by Two-Photon Stereolithography. *Advanced Materials*, pages 5931–5937, 2016.

[87] John H. Campbell, Nicole Nicole, Ori Stein, Ying Liu, Yongfeng Lu, and Lijia Jiang. Three-dimensional printing and deformation behavior of low-density target structures by two-photon polymerization. *Nanoengineering: Fabrication, Properties, Optics, and Devices XIV*, 10354(August):66, 2017.

[88] Klaus Cicha, Thomas Koch, Jan Torgersen, Zhiquan Li, Robert Liska, and Jürgen Stampfl. Young ' s modulus measurement of two-photon polymerized micro-cantilevers by using nanoindentation equipment Young ' s modulus measurement of two-photon polymerized micro-cantilevers by using nanoindentation equipment. *Journal of Applied Physics*, 094906(2012), 2012.

[89] Z. Bayindir, Y. Sun, M. J. Naughton, C. N. Lafratta, T. Baldacchini, J. T. Fourkas, J. Stewart, B. E A Saleh, and M. C. Teich. Polymer microcantilevers fabricated via multiphoton absorption polymerization. *Applied Physics Letters*, 86(6):1–3, 2005.

[90] Enrico Domenico Lemma, Francesco Rizzi, Tommaso Dattoma, Barbara Spagnolo, Leonardo Sileo, Antonio Qualtieri, Massimo De Vittorio, and Ferruccio Pisanello. Mechanical properties tunability of three-dimensional polymeric structures in two-photon lithography. *IEEE Transactions on Nanotechnology*, 16(1):1–1, 2016.

[91] Nadine Noeth, Stephan Sylvest Keller, and Anja Boisen. Fabrication of a cantilever-based microfluidic flow meter with nL per min resolution. *Journal of Micromechanics and Microengineering*, 21(1):015007, 2011.

[92] Mohammad Sadegh Cheri, Hamid Latifi, Jalal Sadeghi, Mohammadreza Salehi Moghaddam, Hamidreza Shahraki, and Hasan Hajghassem. Real-time measurement of flow rate in microfluidic devices using a cantilever-based optofluidic sensor. *The Analyst*, 139(2):431–438, 2014.

[93] Aiping Fang, Erik Dujardin, and Thierry Ondarçuhu. Control of droplet size in liquid nanodispensing. *Nano Letters*, 6(10):2368–2374, 2006.

[94] Rob Bob Theodorus de Gruiter. Dosing of femto liter volumes using hollow atomic force micro- scope cantilever. *TU Delft repository*, page 116, 2016.

[95] Emely Marie Harnisch, Niels König, and Robert Schmitt. Quantitative comparison of measurement methods for the evaluation of micro- and nanostructures written with 2PP. *Nanophotonics VI*, page 98842Z, 2016.

[96] Andrew C Lamont, Ethan C Reggia, and Ryan D Sochol. IN SITU NANO 3D PRINTING OF A MICROFLUIDIC DIODE. pages 1304–1307, 2017.

[97] Caizhi Liao, Will Anderson, Fiach Antaw, and Matt Trau. Maskless 3D Ablation of Precise Microhole Structures in Plastics Using Femtosecond Laser Pulses. 2018.

[98] Li Jia Jiang, Yun Shen Zhou, Wei Xiong, Yang Gao, Xi Huang, Lan Jiang, Tommaso Baldacchini, Jean-Francois Silvain, and Yong Feng Lu. Two-photon polymerization: investigation of chemical and mechanical properties of resins using Raman microspectroscopy. *Optics letters*, 39(10):3034–7, 2014.